University of Alberta

Optimisation of Lung Cancer Treatment

by

Parminder S. Basran   ©

A thesis submitted to the Faculty of Graduate Studies and Research in partial
fulfillment of the requirements for the degree of Master of Science

in

Medical Physics

Department of Physics

Edmonton, Alberta
Fall 1997

Canada

To

my Parents,

Gurbax Kaur and Parkash Singh Basran,

and

my Family.

Abstract

A general solution for the problem of dose homogeneity in an external photon multi-beam configuration is proposed, where internal and external inhomogeneities are accounted for each beam through strategically constructed compensators, and the effects of the multi-beam arrangement are considered through Sherouse's (1993) gradient vector approach. Through this approach, dose homogeneity within the planning target volumes have been found to be better than 5%, exhibiting sharp dose gradients at the point of beam intersection and conforming tightly to the beam intersection points. The simplicity of this technique renders itself for easy implementation in three dimensional conformal therapies and complicated beam arrangements.

The displacements of the lung for several lung cancer patients at the Cross Cancer Institute were taken to estimate the planning target margins specifically allotted for respiration, and also to approximate the clinical implications from irradiating normal lung tissues specifically allotted for this motion. The additional margins, which only include healthy tissue, may be large enough to have negative consequences to the normal lung tissue and thus limit the dose to the tumour. A feasible course of action is to reduce this additional margin through either treating the patient at breath hold, or electronically gating the linac to the tumour's temporal pattern.

Acknowledgements

During my program, there were, and still are, a great deal of people whose assistance, advice, and company that I have come to appreciate. Both kudos and apologies are due to those whom I have failed to include here.

Firstly, I must thank my supervisors and advisors Dr. Brendan McClean, Dr. Will Ansbacher, and Mr. Brad Murray. Were it not for Dr. McClean's encouragement, I would have not taken Physics 475 nor 477, do my honors research project in medical physics, nor enroll in graduate studies to perform the thesis work detailed here. Unfortunately, he eluded the fetters I anchored to his office door by migrating to greener pastures and, as a consequence, I found myself shackled to the doorstep of Dr. Ansbacher, who graciously accepted me as his graduate student. As such, I must thank Will for his advice, guidance, and patience during the latter portions of my program. Brad has been the liaison factor during the transition; for this I am very grateful and appreciative. The efforts of committee members Drs. Urtasun and Rodning are also gratefully acknowledged through their assistance and guidance in the development of the thesis manuscript.

The Faculty of Graduate Studies and Research along with the Department of Physics made my environment conducive towards research by providing both financial and personal assistance throughout my program. I must thank Associate Chairs Drs. Hube and Kernahan and Ms. Lynn Chandler for smoothing over difficulties encountered along with keeping a roof over my head for the last three years. I would like to thank the Alberta Cancer Board, most notibly, Dr Sloboda and Brad Murray, for allowing me the opportunity to work as a Research Scientist while finishing up the thesis.

I wish to thank my fellow graduate students Marc MacKenzie, Lara Dyke, John Kollar, HJ Kim, Isabelle Gagné, and Steve Steciw; all for their helpful (and sometimes inane) interactions and discussions. In addition, the physics staff, Len Johnson (from TMG), John Issit (from the Mold Room), Ernie and Claire, and the rest of the coffee club at the CCI deserve a note of thanks for their assistance, patience and company.

I cannot exclude my family who have unequivocally dispensed their love, support, shelter, and food throughout my thesis work. Lastly, I thank Kim Nayyer, for her support, love, patience, and, of course, meticulous proofing reading skills.

Table of Contents

List of Tables

List of Figures

List of Abbreviations

ATP	Alberta Treatment Planning
CCI	Cross Cancer Institute
CF	Correction Factor
CRT	Conformal Radiotherapy
CT	Computed Tomography
CTV	Clinical Treatment Volume
DPB	Differential Pencil Beam
dSAR	differential Scatter Air Ratio
DVH	Dose Volume Histogram
ETAR	Equivalent Tissue Air Ratio
GTV	Gross Tumor Volume
HVL	Half Value Layer
ICF	Inhomogeneity Correction Factor
ICRU	International Commission on Radiation Units
IV	Irradiated Volume
LRC	Inductance-Resistance-Capacitance
MRI	Magnetic Resonance Imaging
MTV	Mobile Target Volume
NSCLC	Non-Small Cell Lung Carcinoma
NTCP	Normal Tissue Complication Probability
PDD	Percent Depth Dose
PTV	Planning Target Volume
RTOG	Radiation Therapy Oncology Group
SAD	Source to Axis Distance
SAR	Scatter Air Ratio
SCLC	Small Cell Lung Carcinoma
SNR	Signal to Noise Ratio
SPECT	Single Photon Emission Tomography
TAR	Tissue Air Ratio
TMR	Tissue Maximum Ratio
TPR	Tissue Phantom Ratio
TRR	Thickness Reduction Ratio

1. Introduction

1.1 Overview of Lung Cancer

The National Cancer Institute of Canada report that about 28% of all Canadians will be diagnosed with some type of cancer during their lives [Statistics Canada 1996]. Of all cancer types, lung cancer is the leading cause of cancer deaths. Over the last 20 years, clinical studies indicate slight reductions in the incidence of male lung cancers. Despite the efforts to improve lung cancer treatment methods, the fate of diagnosed patients is quite disappointing. In 1993, the lifetime probability of developing lung cancer for males and females is 9.5% and 4.7%, respectively. The lifetime probability of dying from lung cancer for males and females is 8.5% and 4.2%, respectively.

About 90-95% of all lung cancer types may be divided into two cytological categories: Small Cell and Non-Small Cell carcinomas. Small Cell Lung Carcinomas (SCLC) make up approximately 25% of all lung cancers, whereas Non-Small Cell Lung Carcinomas (NSCLC) constitute the remaining portion of lung cancers. Carcinoma types are distinguishable by factors such as clinical representation, response to various forms of therapies, and other biological characteristics. Surgical resection of both NSCLC and SCLC is possible if the diagnosis is made during the early stages of growth. However, cases are most often diagnosed during the latter stages of growth when surgical resection is not feasible. In such cases, other methods of treatment may be used, such as radiotherapy, chemotherapy, photodynamic therapy, ultrasonic hyperthermia, and other novel techniques. The choice of therapy type is primarily a function of clinical benefit-risk factors for the patient.

1.2 Overview of Radiotherapy

Up to 55% of all patients diagnosed with cancer will be treated through radiotherapy. High energy X-rays, Gamma rays, and charged particles are often used to treat a wide variety of cancer types. There are several advantages to using external beam radiotherapy for cancer treatment. First, the characteristics of a high energy radiation are such that larger amounts of energy may be imparted to the underlying (cancerous) tissue than the energy imparted to the surface of the skin. This is of particular advantage when treating tumours situated well beneath the surface of the skin. Second, beam trajectories can be arranged such that the dose to healthy and critical structures is minimised. Surgical resection of deep seated tumours is often quite difficult because of the size and extent of the tumours. Large lung tumours can extend into peripheral structures, such as the heart, healthy lung tissue and other mediastinal structures. An advantage for using radiotherapy is that a high and uniform distribution can be delivered through the addition of beams at various incident angles, so that the resultant energy distribution not only conforms to the tumour geometry, but also avoids critical structures.

The International Commission on Radiation Units and Measurements recommend that when delivering radiation dose, the calculated dose should be within 5% of the actual dose delivered (ICRU 24, p45-50). The ICRU 50 also recommend that the dose to the target volume should be homogeneous within +7% to -5% of the prescribed dose (ICRU 50, p50). The existence of lung tissue provides an added complexity when calculating and delivering dose. One of the objectives of this thesis is to account for these complexities when trying to achieve a high and uniform dose to the target.
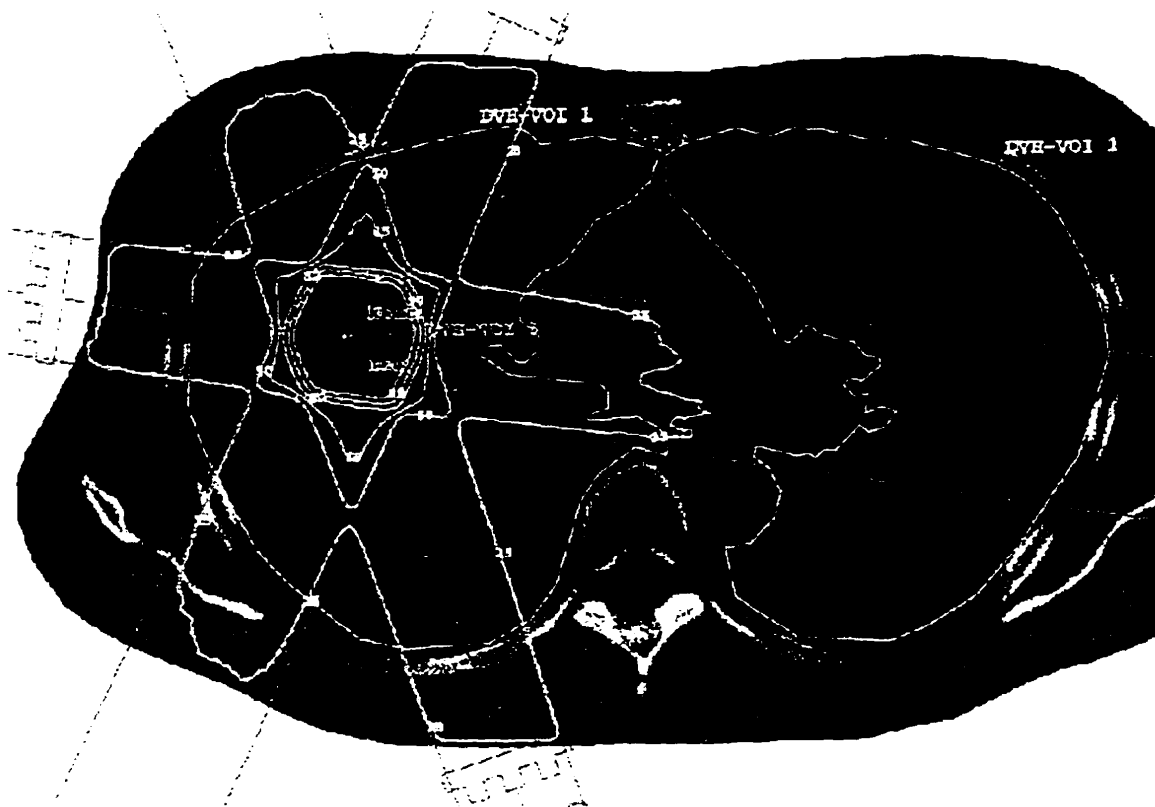
Figure 1.1: A typical CT radiotherapy plan. Shown above are the anatomy, tumour, and the resulting dose distribution from incident radiation beams.

From a quantitative point of view, optimised radiotherapy may be defined as the search for an appropriate objective function to optimise. In this sense, the objective function is to deliver a high and uniform target dose subject to the constraint that normal tissue tolerances are not exceeded [Langer et al. 1993, Niemerko et al. 1992, Mohan et al. 1987]. Another intent of this thesis is to examine and provide a simple solution to this optimization problem, while paying special attention to the clinical concerns of lung cancer.

1.3 Rationale for Optimising Lung Cancer Treatment

Traditionally, a lung cancer treatment plan was restricted to two dimensions, where dose computation and anatomical description lay in a coincident transverse plane. However, faster and less expensive computers have allowed for the possibility of three dimensional target definition and radiation dose calculation. Three dimensional radiotherapy simulation and dose computation of radiotherapy is commonly referred to as Three Dimensional Conformal Radiotherapy (3D-CRT). Computed Tomographic (CT) images, illustrated in Figure 1.1, are used to delineate pertinent three dimensional volumes during the planning process.

Quantitative CT images provide an approximate measure of the electron density distribution and may be used in modeling the energy deposited for arbitrarily positioned photon beams [Van Dyk et al. 1982]. Several studies suggest that the use of three dimensional imaging and dose computation will result in a significant increase in tumour control and a decrease in normal tissue morbidity [Armstrong et al. 1993, Emami et al. 1991].

In the early stages of disease, both NSCLC and SCLC have a high control rate via chemotherapy, radiotherapy, or combinations of both [Cox et al. 1986]. However, the control rate for those diagnosed with NSCLC or SCLC at the later stages of growth is quite low. Some of the reasons for treatment failure are the variations in radiosensitivity between different tumour sizes and types, inadequate delivery of dose, and the deleterious effects of excessive toxicity in normal tissues from radiotherapy. Congruently, increased radiosensitivity of tumour cells, delivery of higher and more uniform doses to volumes, and avoidance of critical structures when delivering tumourcidal dosages may result in higher tumour control. The technology of 3D-CRT allows for improvement of the latter two points. By conforming the radiation fields to the shape of the target volume, a lower amount of healthy tissue is irradiated. Also, beam modifying devices or computer controlled radiation output can shape radiation distributions such that high and uniform dose distributions are achieved at the target. Advances in photon delivery have allowed for the possibility of increasing the dose to levels that were once unattainable through conventional two dimensional treatment planning. Several studies suggest that increasing the dose to the target volume may result in increased tumour control. This suggests a biological rationale for employing 3D-CRT for lung cancer [Graham et al. 1994, Leibel et al. 1991].

The IRCU 24 report states that the highest source of error in treatment planning is beam localization. Localization errors may result in a 6% to 15% reduction in the prescribed dose to the target volume. One of the most frequent sites of beam localization error is the mediastinum. Some possible explanations for these errors are inaccurate inhomogeneity correction algorithms, systematic and random positioning errors, physiological motion, and misalignment of treatment fields. Improvements in beam localisation have been observed with the use of patient immobilization devices during treatment. Such devices can reduce both systematic and random positioning errors. The dosimetric consequences of physiological motion, such as respiratory, cardiac, and peristaltic motion, are still uncertain and they may be of clinical importance when assessing dose uncertainty to the target. Another intent of this thesis is to investigate the effects of respiratory motion in the context of 3D-CRT.

In summary, there are several questions that are the focus of this thesis:

- What are the various physical and physiological parameters involved in obtaining a high and uniform radiation dose distribution for a typical lung cancer patient?

- In light of these physical parameters, can a simple optimisation technique be devised?

- Employing the 3D-CRT approach to radiotherapy treatment planning, what are the treatment planning stages when devising a lung cancer plan? What implications do respiratory motions have to the treatment plan?

- If the effects of respiration are significant enough, how can they be accounted for within the treatment plan?

Firstly, to answer these questions, an understanding of photon transport phenomena in various types of tissue is needed. Therefore, a brief introduction to the physics of ionizing radiation is given in Chapter 2.

Secondly, the basic steps in delivering accurate radiotherapy are outlined in Chapter 3. From the initial diagnostic evaluation, to the treatment planning, and eventually to the treatment delivery, the steps involved in developing a plan is outlined.

Thirdly, in Chapter 4, a brief overview of the anatomy and physiology of the thorax is given. Also included is a review of the potential effects of respiratory motion in radiotherapy and methods to account for respiration from the literature.

In Chapter 5, the optimisation problem is investigated. A brief introduction to the optimisation problem is given and a simple technique for optimising the dose distribution for lung cancers is proposed. Case studies using this optimisation technique are shown along with a discussion of the results.

In Chapter 6, the effects of respiration during treatment planning is investigated. A study of videotaped images of typical lung cancer patients is discussed. Target motion is simulated along with the dosimetric consequences of a treatment plan that accounts for respiration. Techniques for optimising the treatment to account for respiratory motion are presented.

Lastly, conclusions derived from this thesis work along with a brief discussion of the sources of error are given in Chapter 7.

2. Physics of Ionising Radiation

Ionising radiation is ultimately responsible for the deleterious effects radiotherapy inflicts to tissue. Due to space considerations, a detailed explanation of the physics of ionising radiation is omitted here and may be found in elsewhere [Attix 1986, Khan 1984]. This thesis outlines only the basics of ionising radiation.

The ICRU classifies ionising radiation into two categories:

1. Directly Ionising Radiation: This radiation consists of charged, high velocity particles that dissipate energy directly to matter through coulombic interactions.

2. Indirectly Ionising Radiation: This radiation consists of uncharged particles, such as photons (both X-ray and Gamma ray) and neutrons. The transfer of energy is facilitated by an intermediate interaction of the neutral radiation with a charged particle, and the charged particle goes on to deliver the biological damage.

2.1 Charged Particle Interactions

Charged particles for radiation treatment may be delivered from either an external source, such as an electron beam from a linear accelerator, or an internal (contained) source, such as a beta particle radioactive implant. Electrons or beta particles represent virtually all charged particle therapy in most cancer clinics.

Charged particle interactions are facilitated by the particle's coulomb field. Such interactions between a charged particle and a target (which may be charged or neutral) may be classified as either soft collisions, hard (knock-on) collisions, or nuclear coulombic interactions. The types of interactions are categorised with two distances: the distance from the electron's path to the target particle, which is the impact parameter, b, and other distance being the atomic radius, a.

Soft collisions occur when b >> a, or the incident charged particle is far from the atom. Soft collisions are by far the most common type of charged particle interaction (See Figure 2.1). They also contribute about half of the total absorbed energy. In this interaction, the coulombic forces affect the whole atom by either distortion, excitation, or ionisation.

Knock-on, or hard collisions, occur when the impact parameter is on the order of the atomic radius. At these dimensions, the probability of interaction with a single atomic electron becomes significant and the interaction can be approximated as "billiard ball" like collisions. Incoming charged particles can knock loose atomic electrons, which are commonly referred to as delta rays. Like both soft and hard collisions, delta rays can release kinetic energy through coulombic interactions in the absorbing medium. Despite the fact that the probability of hard collisions is lower than that of a soft collision, the relative amounts of energy dissipated by the two processes are comparably the same. In the event of a hard collision electron ejection, characteristic X-rays and/or Auger electrons may be emitted, and these can travel some considerable distance from the interaction site.

Inelastic interactions may take place with the nucleus for charged particles with kinetic energy on the order of several MeV, and impact parameter less than the nuclear radius. For example, an intranuclear cascade can occur where one or more nucleons are struck by an

incident charged particle. Then the nucleus drops from its excited state by emitting evaporation particles and gamma rays. The discussion of pion interactions with the nucleus may be found in more comprehensive texts [Evans 1955].
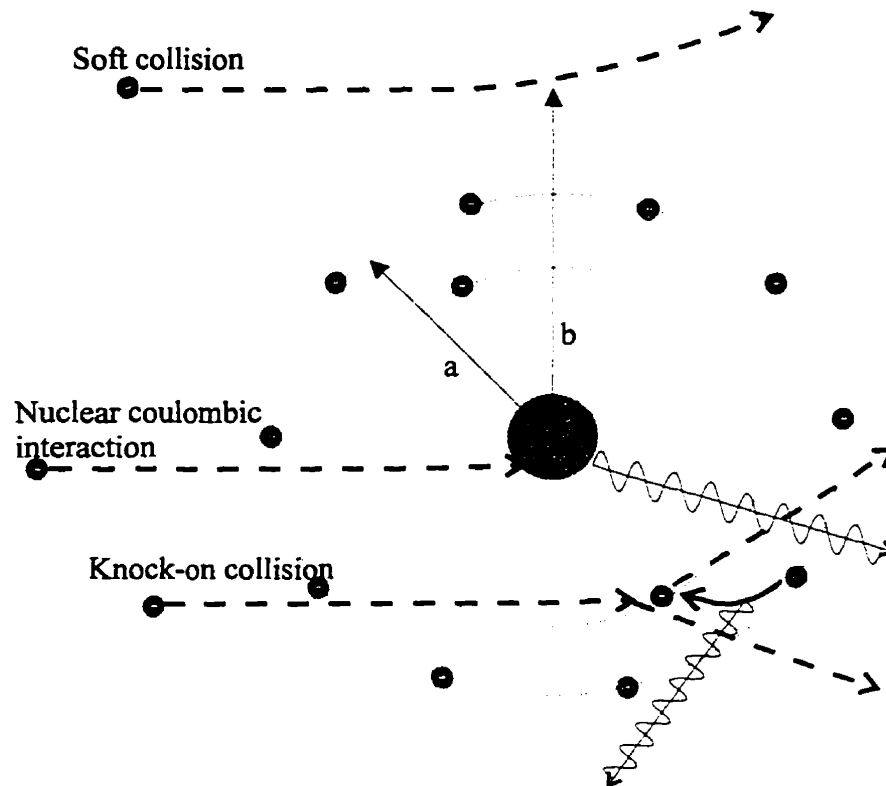
Figure 2.1: Soft, Knock-on and Nuclear coulombic interactions.

2.2 Gamma and X-ray interactions

Of the various types of radiation treatment methods, external high energy photon treatment is by far the most common. Approximately 85% of patients who receive radiotherapy do so via external beam photon radiotherapy.

There are three major types of photon interactions that are important for diagnostic and therapeutic X-rays: 1) Compton Scattering, 2) Photoelectric Absorption, and 3) Pair Production. Left out of this discussion are Photonuclear and Rayleigh interactions, which, because of their minute effects, can be ignored without a loss of accuracy when computing absorbed dose from external beam photons. The type of interaction encountered is often a function of the photon energy and the absorbing medium's atomic composition.

At this point, it may be instructive to make the distinction between the units MeV and MV. By definition, MeV is an energy unit that is equivalent to the energy an electron attains

by accelerating through a potential difference of 1 MV. A linear accelerator consists primarily of a linear array of cavities (or the waveguide) that have high energy electric fields oscillating at radio frequencies. The oscillating fields are used to accelerate electrons through the waveguide, which is then magnetically bent and directed towards the patient. If electron treatment is desired, the beam strikes a metal scattering foil to increase the lateral spread of electrons. The electron beam, in this case, may be characterised in units of MeV. If photon treatment is desired, a high Z target, such as Tungsten, is placed in front of the electron beam to produce brehmsstrahlung radiation. At these energies brehmmstrahlung radiation is forwardly peaked and thus is directed toward the patient. The resulting photons do not consist of a discrete energy but instead a spectrum of energies. The maximum photon energy for a wave guide with an accelerating potential of 6 MV would be 6 MeV. However, the flux of such photons is close to zero; the highest energy flux would be significantly less than 6 MeV, depending on the accelerating voltage and the target's composition. Therefore, it is more appropriate to classify the photon beam in terms of the effective accelerating voltage potential in the wave guide. The peak energy depends on the atomic number of the target material and the accelerating potential within the wave guide. This principle is analogous to a cathode-anode type system, such as those used in diagnostic imaging, where a potential applied to that anode and cathode provides the accelerating voltage for the electrons. The voltage specification indicates the cathode-anode potential, but not the energy of the electrons nor photons produced.

2.2.1 Compton Scattering

Compton scattering is by far the most important interaction therapeutic energy ranges (100 keV to 10 MeV). Compton scattering is also known as inelastic or nonclassical scattering.

In a Compton interaction, an incident photon collides with one of the atomic electrons in the absorbing medium. In the simplest model, the atomic electrons are considered free or weakly bound particles in the atom. After the collision, an electron is knocked loose and the photon loses energy. The free electron then may go on to ionise the surrounding material and deliver dose.

Applying a relativistic treatment of the electron-photon interaction, Klein and Nishina assumed that the electrons are stationary in the photon electron interaction [Evans 1955]. The effective cross section of the Compton interaction, $_e\sigma$, can be calculated theoretically. The resulting effective mass attenuation cross section is given as, .

$$\frac{\sigma}{\rho} = \frac{N_a}{A} Z \, _e\sigma \,,$$

where N_a is Avogrado's number, Z is the number of electrons per atom, A is the mass number, and $_e\sigma$ is the electron Klein-Nishina cross section. An important property of the Klein-Nishina cross section is that it is independent of the atomic number Z. The cross-section is independent of Z since the Klein-Nishina model assumes the electrons are free, and thus, binding energy is not considered. If the photon energy were lower (few keV), where the photoelectric interaction dominates, the binding energy of the electron would become more significant. Since the number of electrons in a medium is approximately proportional to the density of the material for low atomic number elements, the attenuation coefficient, μ, is approximately proportional to the density of the material. The attenuation coefficient is thus independent of the target's

atomic composition. This fact is exploited in dosimetry calculations based on CT image data. A CT image approximates the density distribution *in vivo* by amplifying the atomic Z composition of the patient. The amplification of atomic number in a CT image stems from the photoelectric interaction.

2.2.2 Photoelectric Absorption

This photon interaction dominates for low diagnostic energy ranges (below 100 keV). In this interaction, a photon imparts all of its energy to an inner K or L shell electron of the absorbing medium. Then, an electron becomes ionised while the atom recoils. The kinetic energy of the electron is equal to the difference of the photon energy and the bound potential energy of the atomic electron plus the atomic recoil. After the ejection of the electron, the atom responds by filling the vacancy with a higher orbiting electron, which results in one of two competing processes: 1) an emitted quantized photon, or 2) an emitted (Auger) electron. Afterward, another electron vacancy is created and the process is repeated. It is worth pointing out that the ejected photoelectron can have enough kinetic energy to ionise the proximal material and, therefore, induce biological damage.

The effective mass cross section for photoelectric absorption may be characterised by,

$$\frac{\tau}{\rho} \propto \left(\frac{Z}{h\nu}\right)^3,$$

where $h\nu$ is the incident photon energy. This cubic dependence is exploited in diagnostic radiology. Diagnostic X-rays interact with tissue mostly through photoelectric absorption. The degree of absorption is a function of atomic number cubed. Thus, materials with different atomic number are greatly contrasted by virtue of the cubic dependence in attenuation. For diagnostic CT images, the contrast variations approximate the density distribution.

Photoelectric electrons have the potential to ionise tissue after being ejected from the atom. Thus, the photoelectron may impart energy to tissue and contribute to the dose. The probability of ionisation decreases as incident photon energy decreases. The more likely effect is that the electron is absorbed by an electron deficient atom and a photon is emitted in another direction. This secondary photon contributes to the noise in a diagnostic X-ray image.

2.2.3 Pair Production

Pair production can only occur when the photon energy is equal to or greater than two electron rest masses (greater than 1.02 MeV). The photon essentially transforms into an electron-positron pair via Einstein's mass energy equation, $E = mc^2$, and obtains coequal kinetic energy equal to the difference of photon energy and two rest mass electrons. In this interaction a photon must be in the proximity of a nucleus in order to conserve angular momentum. The produced electron interacts through the usual charged particle interactions as described earlier, while the positron quickly annihilates with another electron to produce two 0.511 MeV photons directed in opposite directions.

The effective mass cross section is defined as,

$$\frac{\kappa}{\rho} = \frac{N_a}{A} \, _a\kappa,$$

where, $_a\kappa$ is the total nuclear pair production cross section per atom. The total nuclear pair production attenuation is proportional to Z^2. Photons emitted from pair production have the potential to ionise surrounding material and thus deposit dose. This interaction is not of particular importance in therapeutic physics unless linear accelerators with energies above 18 MV are used.

2.3 Descriptors for Ionising Fields

2.3.1 Energy Fluence and Kerma

The number of photons passing through a cross-sectional area, N_e, is called fluence. Multiplying this quantity by energy, E, of the photons produces energy fluence, Ψ;

$$\Psi = E\frac{dN_e}{da}$$

Kerma, K, is defined as the kinetic energy transferred to a unit mass and includes all radiative losses. Kerma is related to energy fluence by the mass-energy transfer coefficient, (μ_{tr}/ρ), which is a function of energy and absorbing material. Excluding energy carried away by photons, collisional kerma is defined as,

$$K_c = \frac{dE_{tr}}{dm} = \Psi \cdot \left(\frac{\mu_{tr}}{\rho}\right)$$

Kinetic energy passed from one charged particle to another is not accounted for in μ_{tr}.

2.3.2 Absorbed Dose

An important assumption often made in radiation dose calculation is the connection between dose and kerma. Dose, D, is defined as the amount of energy absorbed per unit mass:

$$D = \frac{dE_{ab}}{dm} = \Psi \cdot \left(\frac{\mu_{ab}}{\rho}\right)$$

and has units of J/kg. The SI unit for dose is defined as a Gray, or Gy, which is equal to 1 J/kg. The mass-energy absorption coefficient, (μ_{ab}/ρ), is equal to (μ_{tr}/ρ) as in the collision kerma, except that (μ_{ab}/ρ) excludes brehmmstrahlung or radiative losses.

A connection can be drawn between kerma and dose where both are equal provided that charged particle equilibrium and radiation equilibrium exists. In the non-stochastic limit, radiation equilibrium exists when a photon, with a given energy, entering a volume replaces a photon, with same energy, leaving that same volume. The concept of charged particle equilibrium is equivalent to the mass continuity equation where charge, as opposed to mass, is conserved and no sources nor sinks exist within the volume of interest. For a specified amount of charge entering a volume, there exists an equal amount of charge exiting the volume.

If the volume is small enough, we can allow radiative-loss photons (or those photons generated from brehmmstrahlung) to escape the volume. This being true, we can approximate the total amount of energy absorbed within the material to the total energy absorbed minus the

radiative loss photons, $D = K_c$, where K_c is the collisional kerma. The collisional kerma excludes radiative-loss photons.

More often than not, charged particle equilibrium does not exist, and to accurately describe photon dose distributions, one assumes a state of transient charged particle equilibrium. Transient charged particle equilibrium exists when the dose is proportional to collisional kerma. For typical external radiotherapy beams, dose becomes approximately proportional to kerma at a significant distance below the surface of the absorbing material. This is primarily due to two factors: The photon beam is not "pure" since it often contains (contaminant) electrons generated from ionisation of the preceding material (normally air). Also, the photons that interact with the interfacing material produce ionising electrons that are primarily forwardly peaked. These electrons may travel several centimetres, depending on the photon energy and the absorber's composition, "down" stream in the direction of the incident photons. At the surface, the electron flux is not nearly as large as those generated within the absorber. Thus, the dose "builds up" to a maximum distance, called the "equivalent thickness", as opposed to the kerma that is maximum at the surface. In such regions, the kerma is significantly greater than the dose and charged particle equilibrium does not exist..

Even past the equivalent thickness, dose and kerma cannot be equal because dose neglects all brehmsstrahlung losses. After the equivalent thickness, the kerma becomes roughly proportional to dose, but not in charged particle equilibrium due to the radiative losses; thus, such regions are said to be in transient charged particle equilibrium.

2.4 Basic Dosimetry Fundamentals

It is generally not possible to measure the amount of radiation a patient receives during the treatment plan. Even if it were possible, it still would be necessary to simulate optimal beam configurations. Thus, it becomes necessary to develop computer algorithms that accurately predict radiation distributions for various patient and beam configurations. As is shown in Chapter 3, many dose calculation algorithms involve both analytical and empirical techniques. Some basic empirical quantities commonly used in many of these algorithms are now described.

2.4.1 Tissue Air Ratio, Tissue Phantom Ratio, and Scatter Air Ratio

The tissue-air ratio, or TAR, is defined as the dose at some reference depth, X, in tissue divided by the dose at a point, X', in air (see Figure 2.2). Tissue in this context is implied to be water, or water equivalent material. The TAR is primarily a function of the beam's depth, width, and energy. The distance, f, is common for both measurements of dose in the determination of TAR:

$$TAR_x(d, W_d, h\nu) = \frac{D_x(d, W_d, h\nu)}{D_{x'}(d, W_d, h\nu)}.$$

The original intention of the TAR was to aid in calculating dose to tumours in rotation therapy for low energy photon beams (less than 0.6 MeV). In rotation therapy, the head of the treatment machine rotates about a central point, X, and delivers continuous photon treatment. As the distance from the center of the target to the external patient contour changes, different values of TAR are used in predicting the total dose to the target. It has been shown

experimentally that TAR does not change significantly for f > 50 cm; therefore, only a single TAR table is necessary to predict the dose at the point of rotation [Johns et al. 1958].
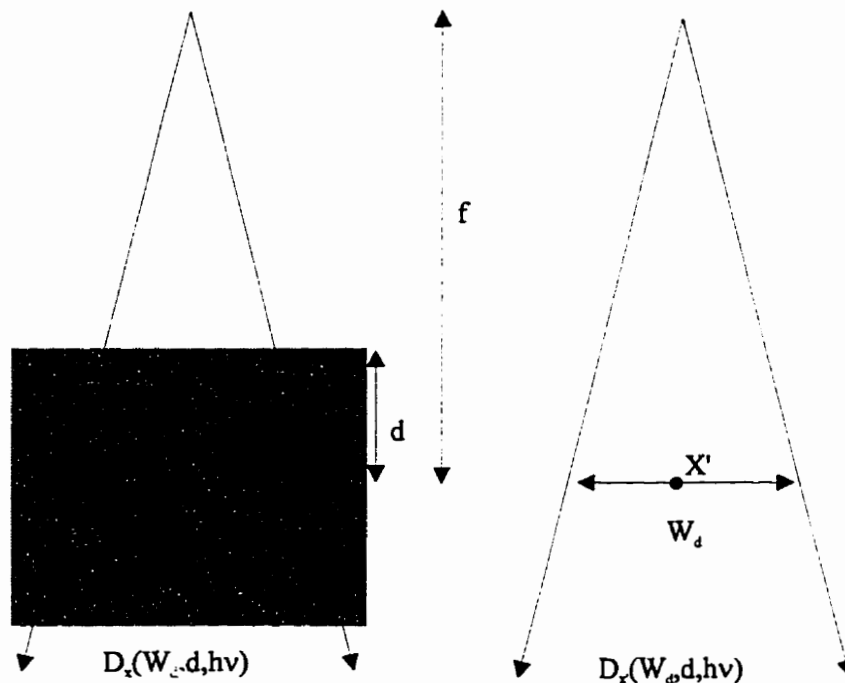
Figure 2.2: Description of TAR.

If the photon energy increases beyond 0.6 MeV, electrons that scatter from Compton interactions can have ranges that are on the order of centimetres. To ensure that charged particle equilibrium exists within the ionisation chamber, a buildup cap should be used to encapsulate the chamber. The thickness of the cap must be equal to or greater than the equivalent depth to ensure equilibrium. TAR values are not used in high energy photon treatment calculations because of the large amount of build up material required to ensure charged particle equilibrium. Subsequently, the measurement of dose in air becomes harder to interpret for high energy photons than for low energy photons. For high energy photon the tissue phantom ratio, or TPR, is often used for empirical dose calculation. The TPR is defined as,

$$TPR_x(d, d', W_d, hv) = \frac{D_x(d, W_d, f, hv)}{D_{x'}(d', W_d, f, hv)}.$$

The distance from the measuring point to the source, f, remains constant where the depth of the phantom tissue material, d and d', is modulated. The TPR can be interpreted as being somewhat similar to TAR where the reference point in air is replaced by a reference depth in tissue.
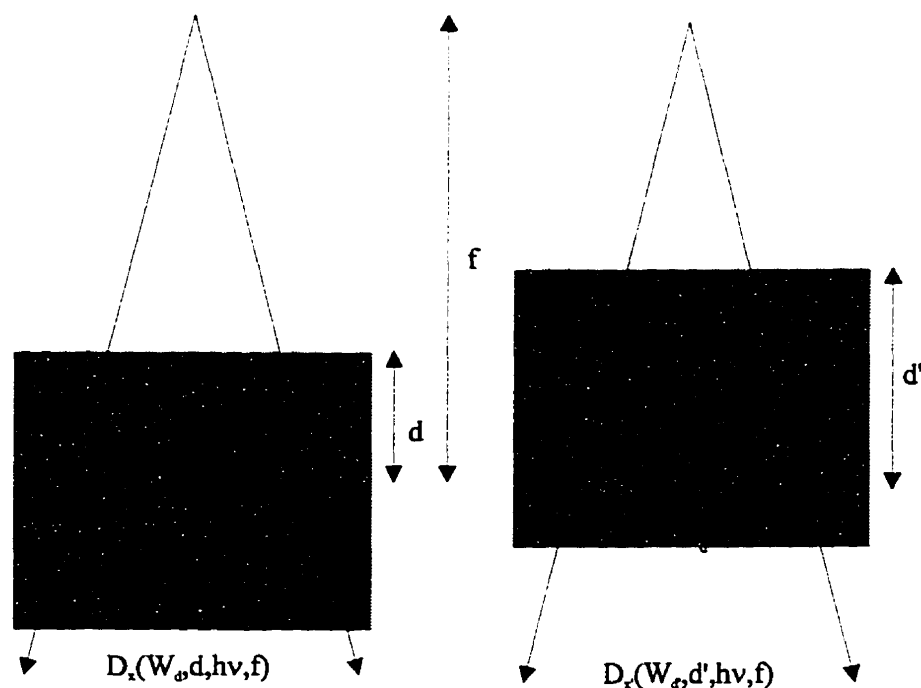
Figure 2.3: Description of TPR.

The scatter air ratio, or SAR, is a numerically calculated quantity that represents the amount of scatter dose to a referenced point. If the beam size, W_d, approaches zero, we begin to approximate a narrow beam geometry. Ideal narrow beam geometry excludes any photon scattering into the detector and will essentially be a measure of the narrow beam attenuation of the material. Thus, the amount of scatter of a beam of width, W_d, at depth, d, will be,

$$SAR(W_d, d, hv, f) = TAR(W_d, d, hv, f) - TAR(0, d, hv, f).$$

Values of SAR represent the amount of scattered dose from a given beam size, energy, depth and source to surface distance (SSD). SAR tables can prove useful in empirically based dose calculation algorithms.

2.4.2 Percentage Depth Dose

The percentage depth dose is a spatial descriptor of the relative amount of dose delivered as a function of depth. The shape of the depth dose curve is a function of beam size, energy, depth, and SSD.

Figure 2.4 shows a typical depth dose curve for a 30 x 30 cm field incident on a homogeneous phantom. Upon inspection, it is evident that the dose deposited does not display simple exponential attenuation. At the surface, there is a considerable lack of backscatter as charged particle equilibrium is violated. At further depths, transient charged particle equilibrium exists and the dose deposited begins to depict a more exponential behavior. However, the beam becomes "harder", meaning that the probability of interaction decreases at further depths. This is because the photon beam, which consists of a spectrum of energies,

slowly becomes filtered by the medium as the lower photon energies interact and deposit dose within the medium.

The scatter contribution to dose increases as depth increases. The hardened beam interacts via Compton interactions more energetically and the ejected electrons have more kinetic energy. These ejected electrons can produce more ionisation than can weaker photons. This contributes to the "tail" like appearance of the percentage depth dose curve.
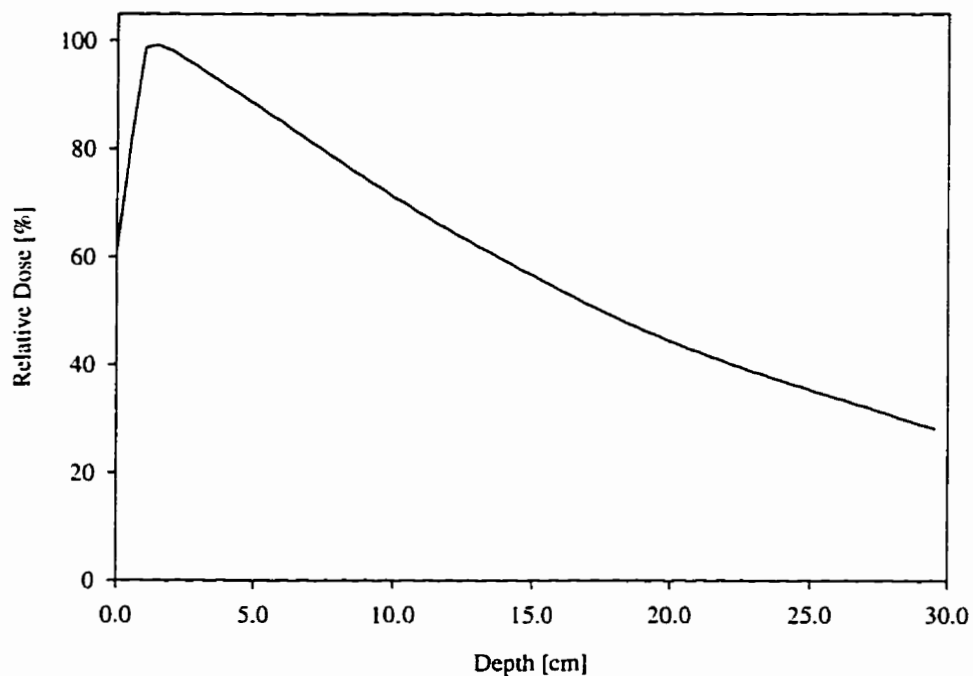
Figure 2.4: Percentage Depth Dose curve for a 30 x 30 cm photon beam at 6 MV. The phantom is a homogeneous water box and the source is 100 cm from the surface of the phantom. The dose is normalised at 1.5 cm below the surface.

3. Steps Involved for Accurate Radiotherapy Delivery

The purpose of this chapter is twofold; to provide the background information for the optimisation routine developed in Chapter 5, and to give context to the problems that respiration may impose throughout the treatment planning procedure. The following procedures may differ significantly from procedures used in other treatment facilities. Also possibly true is that all of the following procedures may not be all performed at the Cross Cancer Institute and may be in different chronological order. Despite these variations in treatment planning methodology, assessing the possible sources of error when defining margins around a tumour requires a systematic approach. Therefore, for the lack of a better method, I will outline the various stages in a typical lung cancer treatment plan at the Cross Cancer Institute and discuss some potential problems that are relevant in this thesis work.

3.1 Diagnostic Procedure

3.1.1 Diagnostic Evaluation

Assessing the type and extent of cancerous growth is primarily the responsibility of the clinician. Although this is a formidable task, the ability to diagnose a lesion has improved greatly over the last 20 years. Evaluating the physical extent of disease is aided with various imaging modalities, of which the most common is X-ray transmission radiography. The radiograph consists of low energy photons (approximately 10-100 keV) directed toward and through the patient. In such energy ranges, photoelectric absorption is the primary method of interaction. The image, in video or film format, represents a two dimensional density mapping of the subject. Although radiographs are a cost effective method for diagnosing disease, the amount of information they provide is limited to a low contrast, divergent two dimensional geometry. Three dimensional imaging devices, such as MRI, SPECT, and CT often provide more useful contrast information when delineating target volumes.

3.1.2 Use of Computed Tomographic Images

Computed Tomographic images provide a density map of patient anatomy. Two dimensional transverse images are taken in intervals in the transverse plane. Stacking these planar images comprise a three dimensional density matrix of the patient's anatomy. The stacking intervals can vary from several centimetres to 0.1 centimetre. A particular advantage of Computed Tomography is that contrast is approximately proportional to density, which means that the images can be used in dose calculating algorithms [Battista et al. 1980, Van Dyk et al. 1982]. This density information may be used to model Compton interactions at therapeutic X-ray energy ranges. An example of a CT image with a superimposed dose plan is shown in Figure 1.1.

The conventional approach to treatment planning utilises a CT data set for the photon dose calculation. The intent of using the CT data set in the treatment plan is to predict the dose received for a given beam configuration. Therefore, it is necessary that the conditions during the image acquisition be as close as possible to the treatment delivery conditions. Such conditions include, but are not restricted to, patient orientation and positional accuracy. Errors

in positioning and density from the CT data set will translate to inaccurate dose calculation. Factors such as pixel and voxel size can contribute error in predicted dose through partial volume effects. Also, the densitometric accuracy of the CT image also becomes important if inhomogeneity correction algorithms are used in the computation of dose (as we shall see in Section 3.2.2.1).

3.2 Treatment Planning

After a diagnosis is made and the clinician decides radiotherapy is the best method of treatment, a radiotherapy treatment plan is sought. The treatment plan is often devised by a treatment planning specialist in conjunction with a clinician and/or physicist. The treatment planner's objective is to ensure a high and uniform dose to the target volume without damaging normal tissue.

3.2.1 Simulation

Before the radiotherapy treatment can begin, the patient may undergo a simulation of the plan. Inside the simulator room is an X-ray machine that has a similar design to a linear accelerator: a rotating gantry, collimator and table, a table of variable height settings, and light fields that mimic the treatment fields. Also included are a fluoroscopy unit and an X-ray film tray where images may be obtained either dynamically or statically.
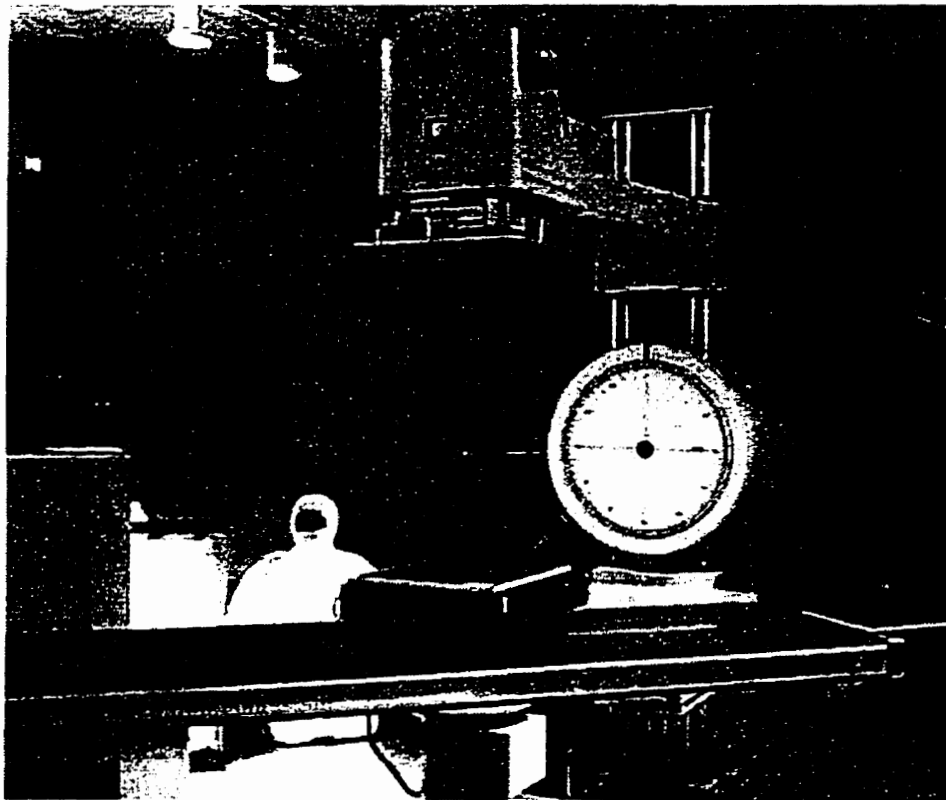
Figure 3.1: A radiotherapy simulator room.

There are several purposes for the simulation, one of which is to (re)assess the extent of the target volume as seen from the beam's eye view. Fluoroscopic images display the anatomy in "real time" and can therefore provide valuable information regarding the likely position of the target. The size of the treatment field is determined by various factors, that may be broken down into various sub-fields. These sub-fields are defined in the next section. After the total treatment field is defined, visible reference markings can be placed on the patient to ensure proper field alignment during the routine treatment.

3.2.1.1 Clinical Target Volume Descriptors

The degree of tumorous microextensions, random patient motion, and other factors need to be assessed when defining the treated volume. When the total planning target volume is delineated, margins around the tumor site need to be accounted for systematically. The IRCU 50 recommend defining three primary volumes of interest when delineating the total planning target volume.

The visible lesion is defined as the Gross Tumor Volume (GTV). This is normally defined on either radiographs or CT images. The GTV represents a volume where marked contrast variations are observed between the tumour and the surrounding normal tissue. Volumes delineated on radiographs or CT images include only the radio-opaque portions of the tumour. The GTV itself may be different from the radio-opaque tumour when other imaging modalities, such as magnetic resonance imaging, are used to define the gross tumour volume. A more precise definition of the GTV can be made with the use of three dimensional images.
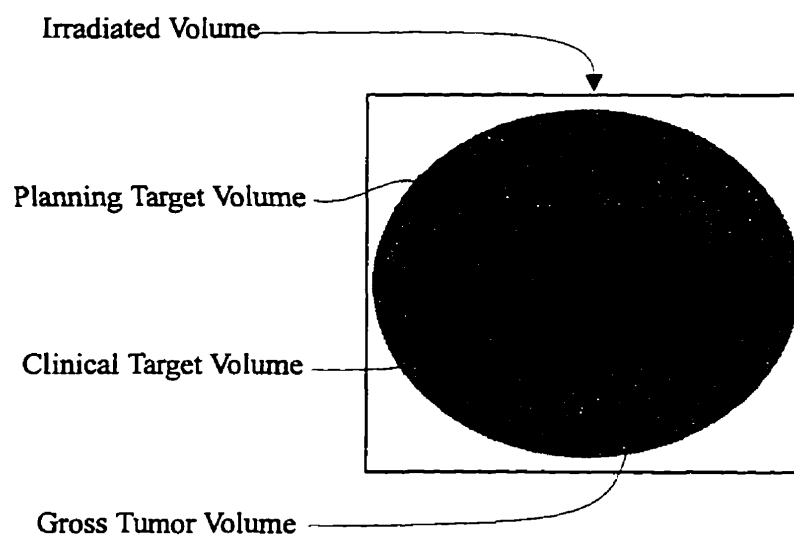
Figure 3.2: IRCU definitions of clinical target volume descriptors.

Since the GTV often will not contain all the tumour cells, it is necessary to allot a margin around the visible GTV so as to include non-visible cancerous microextensions. The margin of cancerous microextensions plus the GTV is called the Clinical Target Volume

(CTV). The CTV encompasses the biological extent of the disease, distinguishing the disease from normal tissue. Defining this margin may not be as simple as allotting a uniform margin around the perimeter of the GTV. The margin is approximated by the clinician based on experience and other clinical factors, such as adjacent structures and tumour cell kinetics. Austin-Seymour et al. (1995) have reported that defining this margin is very subjective and can vary significantly between clinicians and clinics.

A margin surrounding the CTV, the planning target volume (PTV) is defined to allow for random and systematic motion during the treatment. The extent of this margin is based entirely on geometric factors, such as ranges of motion due to respiration, margins for daily patient set-up errors, and accuracy of the light and beam fields on the treatment machines. Other definitions within the PTV have been proposed [Urie et al. 1991], such as the Mobile Target Volume (MTV) that outlines the most probable location of the CTV. The MTV would allow for both random displacements and physiological motion. Much like the CTV, the PTV may have non-uniform margins depending the surrounding anatomy and systematic displacements. Obviously, it would be advantageous to keep this margin to a minimum so that healthy peripheral structures are not needlessly irradiated. Examining the extent of this margin due to respiratory motion will be the focus of Chapter 6.

The planning target volume is the idealised volume of treatment. Due to the limitations imposed by the linac port, the PTV may not coincide to what is feasible. The additional tissue irradiated as a result of using feasible beams geometries is called the Irradiated Volume.

In addition to the Compton and photoelectric effects that deposit dose to the planning target volume, there are scattered electrons and photons that may extend beyond the margins defined by the port. It is probable that these interactions may deliver a small but significant dose far from the planning target volume. Also, dose may be delivered from scattered photons emanating from within the head of the linac and also inside the patient.

3.2.2 Calculation of Photon Dose

There are a wide variety of dose calculation algorithms that are used to predict radiation dose distributions. Such algorithms may be empirically based look-up tables, such as the dSAR method, or the algorithm may rely on computer simulation of photon interactions, such as the Monte Carlo simulation. Advances in physics and technology have allowed for the possibility of achieving 2% accuracy for homogeneous dose calculations [Van Dyk et al. 1993]. In most practical circumstances, this 2% benchmark is a reasonable lower limit of dosimetry error for external photon beams incident on homogeneous phantoms.

Since tissue densities different from water equivalent density will have different radiation transport characteristics, calculational techniques that account for such inhomogeneities are required. Such density variations are most evident in organs such as the lung, esophagus, and bone. There are many algorithms that are used to correct for such inhomogeneities. In general, these inhomogeneity correction algorithms do not meet the 2% benchmark established in homogeneous phantoms. In fact, errors found in computing dose to inhomogeneous tissue are significantly higher. Wong et al. (1991) have reported that errors in inhomogeneity correction algorithms range from 2 to 10 %. Most inhomogeneity correction algorithms over-estimate dose [Kappas et al. 1995, Wong et al. 1991, Orton et al. 1984] to the inhomogeneous tissue.

An implicit assumption in many inhomogeneity algorithms is the existence of lateral equilibrium. Mackie et al. (1984) have found that lateral equilibrium is violated for photon energies of 6 and 15 MV. In the condition of disequilibrium, the proportionality between kerma and dose ceases. Larger field sizes would improve lateral disequilibrium, but for higher energy photons (> 6 MV), lateral electron ranges become greater than 5 cm. Therefore, field sizes greater than 10 cm would be necessary to establish the proper equilibrium. One of the major obstacles in devising inhomogeneity correction algorithms is the ability to model lateral scatter accurately.

Briefly outlined below are several calculation algorithms used to predict photon dose to inhomogeneous tissue. A more detailed overview of calculation algorithms may be found in other texts and papers [Wong et. al 1990, Mackie et. al 1996].

3.2.2.1 Inhomogeneity Correction Dose Calculation Algorithms

The ratio between dose to the inhomogeneous media and the dose in water is defined as the Inhomogeneity Correction Factor;

$$ICF(r, z) = \frac{D_{inhomogeneous}}{D_{water}} .$$

The variable r corresponds to the field size and z corresponds to the distance from the surface to the calculation point. The ICF can be calculated for every point in the calculation window, or for one point only. Inhomogeneity Correction Algorithms may be divided into 2 categories: scatter and non-scatter correction algorithms.

3.2.2.2 Nonscatter Correction Algorithms

A common and simple method used to calculate dose to inhomogeneous media is through use of the ratio of TAR, or RTAR, method:

$$ICF(z) = \frac{TAR(z')}{TAR(z)} .$$

The crux of this method stems from the argument that the effective dose received to an inhomogeneous material is the same as it would be at some equivalent reference depth in a homogeneous, or water equivalent material. The reference distance depends on the electron density relative to water and is calculated by finding the effective pathlength of tissue traversed. The effective pathlength of the tissue is computed from the following integration:

$$z' = \int_0^z \rho(t)dt ,$$

where z is the depth of the calculation point and density may vary with respect to depth. TAR values are looked up and the ratio is calculated. The TAR values correspond to the same field size at differing depths.
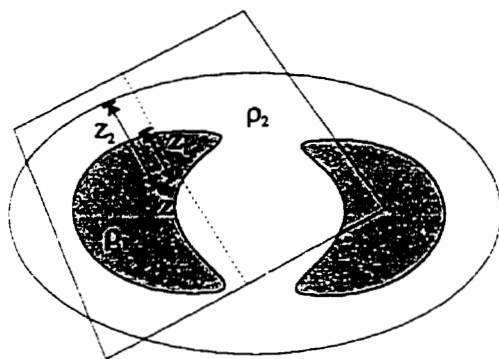
Figure 3.3 Point dose computation within the lung.

Another common correction technique is the Batho correction law [Batho 1964, Cassell et al. 1981] where,

$$ICF(z) = \frac{TAR(z_1)^{\rho_1 - \rho_2}}{TAR(z_2)^{1-\rho_2}} \cdot$$

This method attempts to model the exponential behaviour of the photon dose for multiple materials of varying density, where ρ_1 and ρ_2 are the electron densities of the first and second layer of material relative to water under or above the calculation point z, and z_1 and z_2 are the distances to each layer (See Figure 3.3). Since the model does not account for electronic build up regions at interfaces nor backscatter, Wong and Henkleman (1991) found that the Batho method produces a result smaller than when measured. The correction factor error at interfaces may be circumvented through a kerma correction of the TAR values, however, there still exists the problem of under correction for radiological distances greater than 1.5 cm. Another major disadvantage of this model is that it is one dimensional in nature; it does not explicitly account for the shape of the overlying points in the calculation plane. Using the Batho correction algorithm for Cobalt 60 photons, errors in dose have been found up to 15% but are commonly on the order of 5% [Kappas et al. 1995, Wong et al. 1991]. The Alberta Treatment Planning (ATP) dose calculator at the Cross Cancer Institute has the ability to compute doses to inhomogeneous tissue through several inhomogeneity correction algorithms (Batho, ETAR, and RTAR). As we shall see in Section 5.1.1, the Batho algorithm on ATP may have errors less than or equal to 5%.

A commonly found non-scatter method formulated in 3 dimensions is the Equivalent Tissue Air Ratio, that was developed by Sontag and Cunningham (1978). In this method,

$$ICF(z) = \frac{TAR_{medium}(z)}{TAR_{water}(z)},$$

and

$$TAR_{medium}(r, z) = TAR_{water}(0, z') + SAR_{water}(r'', z').$$

The ETAR method employs O'Connors theorem, which states that the dose to a point in a homogeneous media of an electron density not equal to water can be considered equivalent to that in a homogeneous water medium, provided that all the linear dimensions of the non water

medium are scaled by some constant factor. The first contribution to the TAR_{medium} consists of the TAR for a thin pencil beam at a depth equal to the equivalent pathlength. The second contribution consists of the scaled scatter contribution from an equivalent field size, r", at an equivalent depth, z". For every inhomogeneous voxel in the dose matrix, an equivalent homogeneous medium of effective density, ρ", is found:

$$r" = r\rho" = r\sum_{i,j,k} W_{ijk}\,\rho_{ijk}\,\Delta V_{ijk}\ ,\ \text{where}$$

$$\sum_{i,j,k} W_{ijk} = 1\ .$$

The constrained weighting factors W, are empirically chosen. ΔV_{ijk} and ρ_{ijk} are the corresponding volume and density of pixel element (i,j,k). The weighting factors may be approximated through the addition of dSAR components of primary and multiple scatter dose contributions, which may be separately modeled. The three dimensional nature of the ETAR method makes the algorithm computationally extensive and time consuming. For this reason, simpler two dimensional approximations are often used. Differences of up to 5% have been reported when comparing measured and simulated data using this algorithm [Yu et al. 1990]. Errors in the ETAR algorithm in ATP have been shown to be less than or equal to 5%. The errors stem from the problems that Batho model similarly faces, such as the inability to model lateral scatter and dose close to interfaces, with the addition of potentially ambiguous weighting factor determination. In some instances, more accurate doses can be computed if radiological depths are used instead of analytically derived weighting factors [Yakiwczuk 1987].

A sophisticated three-dimensional non-scatter correction algorithm is the convolution method as suggested by Boyer et al. (1986). This approach is much more mathematical than previous models. Dose to voxels are computed through convoluting the three dimensional dose kernels over the fluence distribution. The dose to a point, $D(\bar{r})$, is defined as:

$$D(\bar{r}) = \int \Psi o(\bar{r}\,') \times k(\bar{r} - \bar{r}\,') \cdot d\bar{r}\ ,$$

where Ψ_o is the vector field energy fluence, and $k(\bar{r} - \bar{r}\,')$ is the kernel dose distribution, integrated over the volume of the field. Integration may be performed over a spectrum of energies to allow for non-monoenergetic beams. The kernels can be spatially invariant or variant, depending on the calculation algorithm used. This method has an advantage over others since it can be implemented with a Fast Fourier Transform that can speed up calculation times considerably. The convolution computation is relatively straight forward to implement, however, accounting for tip angles, or beam divergence, and inhomogeneities requires a great deal more effort. Normally, invariant kernels and scaling methods are used to describe the kernel for different depths and tissue types. However, to account for beam divergence, rectangular kernels must be rotated according to beam width. Alternatively, one can rotate the kernels for the dose computations, or allow for kernel variance in the convolution. A major advantage of convolution techniques is its ability to model lateral scatter with a point spread function.

For inhomogeneous phantoms, dose is calculated with primary, first scatter, and multiple scattering kernels,

$$D(\bar{r}) = \iint \Psi_o(\bar{r}\,') \times [k_p(\bar{r} - \bar{r}\,') + k_s(\bar{r} - \bar{r}\,') + k_m(\bar{r} - \bar{r}\,')] \cdot d\bar{r} \cdot dE\ .\ \text{(Equation 3.1)}$$

The primary dose kernel may be derived directly by using a delta function to describe its position, multiplied by the relative stopping powers, interaction cross section and relative electron density. Analytically, the scattering kernel would consist of an integration over all angles from the scattering point while sampling the various densities along each ray. This would be in fact a scatter ray-trace method if the computation was carried out as such; however, in Boyer's model, a linear approximation is made where the first scatter kernel is scaled with the density at the site of computation. Boyer et al. (1986) suggest a technique where the exponential attenuation from the scattering sites is approximated with a Taylor expansion. The multiple scattering kernel is approximated by a spatially invariant kernel based on classical diffusion theory. Through this approach, ray tracing is completely avoided, and thus allows for easy FFT implementation. Errors of up to 4% have been reported with this calculation technique. This algorithm is increasing in popularity because a FFT implementation decreases computational time significantly.

The convolution/superposition method has been suggested by a number of authors [Mackie 1984, Ahnesjö 1984, Boyer et al. 1986, Mohan et al. 1986]. Variations of the convolution/superposition method will be described in the next section.

3.2.2.3 Scatter Correction Algorithms

With the advent of three dimensional CT and faster computing times, three dimensional scatter correction algorithms are becoming more common. The dSAR method, developed by Cunningham (1972), is a three dimensional extension of the RTAR method. The dSAR is a semi-empirical dose calculation algorithm that employs scatter integration of voxels based on measured data. In this method, we define ICF where

$$TAR_{medium}(r, z) = primary + scatter .$$

The primary component consists of a narrow beam photon beam at depth z, and the scatter contribution is equal to the integration of all scattered voxels surrounding the calculation point:

$$primary = TAR_{medium}(0, z) , \text{ and}$$

$$scatter = \sum_r \sum_\theta dSAR_{medium}(r, \theta) .$$

The algorithm is executed through a three dimensional integration from measured data. The inhomogeneity corrections impose an added degree of complexity, since the medium will not be the referenced homogeneous phantom. The inhomogeneity is accounted for in the calculation of TAR_{medium}, which is coupled with an exponential term:

$$TAR_{medium} = TAR_{water}(0, z) \times \exp\left[\mu_o \Delta z \sum (1 - \rho_{primary})\right],$$

where μ_o is the attenuation coefficient of the material through which the primary ray passes through, $\rho_{primary}$ is the density voxel of which the primary ray traverses, and Δz is the voxel length of the traversed primary ray. The dSAR is calculated in a similar manner:

$$dSAR_{medium} = dSAR_{water}(i, j, k) \times \rho_{ijk}$$

$$\times \exp\left[\mu_o \Delta z \sum (1 - \rho_{primary})\right],$$

$$\times \exp\left[\mu_1 \Delta r \sum (1 - \rho_{secondary})\right]$$

where $\rho_{secondary}$ is the density of the voxel element along the scattered ray, μ_t is the linear attenuation of the scattered ray, dSAR(i,j,k) is the subtraction of SAR values of the calculation point from the scattering point in question, and ρ_{ijk} is the density at the scattering point.

Multiple scatter is not needed in the calculation since the TAR values include all the extra scattering effects. It has been found that this computational technique works well for homogeneous phantoms, but breaks down for inhomogeneous phantoms. Some of the reasons the algorithm fails are that the model dose not account for backscatter at interfaces and it does not account for multiple scattering effects at higher energies. Errors in computed dose have been reported from 2% to 6% [Kollar 1996, Wong et al. 1990, Kappas et al. 1995].

As stated earlier in Section 3.2.2.2, there have been several convolution type dose computation algorithms proposed. The basic technique is the same as that described in Equation 3.1 with variations in the type of data used, implementation, scatter correction, and inhomogeneity correction.

The differential pencil beam (DPB), introduced Mohan et al. (1986), suggest the use of a dose kernel at the point of first collision within the phantom. Traditionally, the energy of the photon beam is characterised discretely by a nominal energy value: 1/3 of the maximum photon energy. However, adequately describing the depth dose curve requires a more accurate assessment of the beam's energy spectrum in the dose computation. Direct measurement of a clinical treatment unit's spectrum is virtually impossible due to the high photon intensity, thus Mohan et al. (1985) derive the photon energy spectrum by performing Monte Carlo simulations of the treatment head where millions of histories are generated and recorded as the accelerated electrons impinge on the various components within the port of the machine (flattening filter, collimators, monitor chambers, etc.,). The energy spectrum is determined discretely for a particular treatment machine through Monte Carlo simulations of the photon production. Afterwards, a DPB is derived, through Monte Carlo simulation, for each photon energy in a uniform phantom and the resulting dose is the superposition of monoenergetic DPMs with their appropriate weightings.

The dose at a point q is evaluated by performing an integration of the DPB in spherical coordinates (see Figure 3.3). The dose from the individual spherical sectors is computed by multiplying the value of the DPB(r,θ), from the Monte Carlo data, with the number of collisions in that element. The latter is computed through the following expression:

$$\Phi_p(E_i) \cdot \exp\left(-\langle\mu(E_i)\rangle \cdot t_p\right) \cdot \left(\frac{\mu(E_i)}{\langle\rho_q\rangle}\right),$$

where the photon fluence is approximated as fluence in air at the point p, exponentially attenuated through the distance t, multiplied by the mass energy transfer coefficient. ρ_q is the density at point q. The inhomogeneities are incorporated by dividing the attenuation by the "effective" density. The effective density is computed from a spatial averaging of the densities between the calculation and scattering points. Once this is computed, O'Connors scaling method is employed to find the water equivalent thickness. The equivalent thickness is used when the algorithm retrieves the DPM values from the Monte Carlo table data. In cases where the calculation point exists inside an inhomogeneity, the photon fluence is attenuated using the average total linear attenuation coefficient to the point t. By virtue of O'Connors scaling method, an assumption is made that the secondary electrons travel in a straight line from the scattering to the calculation point. This is not entirely the case and this assumption will

produce errors at lateral interfaces [Knöös et al. 1995]. Also, it is assumed that each sampled pixel along the raylength contributes equally to the scattered photon fluence. It may also be true that one voxel within the sampled raylength effects the scatter fluence more than other voxels along the raylength. This oversight is accounted for in the collapsed cone algorithm (see further).

The DPB method is very accurate for homogeneous phantoms at distances greater than the equivalent thickness (2 - 4%). However, the method does not consider contaminant electrons from interactions upstream; thus, the model underestimates dose considerably at interfaces. Since each DPB is spatially variant, the computation requires a full volume integration for each computation point. This increases the computation times significantly.
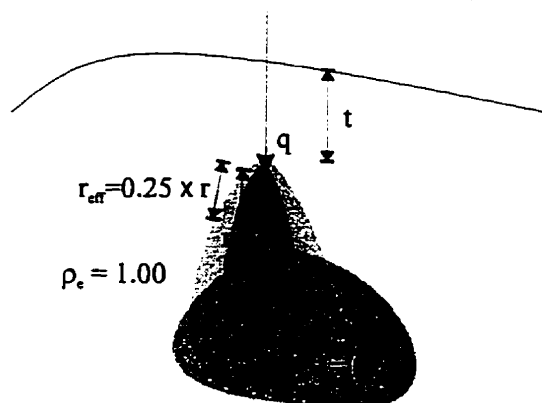
Figure 3.4: The convolution approach.

Computation time can be decreased significantly if the kernels are spatially invariant. Mackie (1984) computed similar differential pencil beams, but instead calling them dose spread arrays (The terms dose spread array, differential pencil beams, and dose kernel are equivalent descriptions of a three dimensional kernel of dose in a homogeneous phantom). The computation of dose is performed by convoluting the fluence spectrum with the DPM to yield a full three dimensional dose distribution. Primary, first scatter, and multiple scatter kernels are individually convoluted and summed, similar to Boyer's model. The contaminant electron doses are accounted for by adding the dose due to stray electrons to the computed distribution. Mackie found that this contaminant dose distribution may be easily approximated through a gaussian like distribution, which is a function of field sizes in both x and y directions, radiological depth, and 2 dimensional position within the phantom. The FFT implementation is not possible when accounting for inhomogeneities. The inhomogeneity correction is performed by employing O'Connors scaling method to the unit electron density DPB. The primary kernels for various electron densities are generated by scaling the geometry by the average electron density in the medium. Similar scaling is performed for secondary and multiple scatter kernels in the heterogeneous medium without density sampling. Each kernel becomes spatially variant and the convolution is performed for each pixel separately, thereby being a superposition. The assumptions made in the inhomogeneity correction are identical to those in Mohan's DPB model. Despite these assumptions, the resulting dose distributions prove to be depth dose consistent for unit density phantoms, particularly close to interfaces.

At the Cross Cancer Institute, the Helax[1] three dimensional dose calculator employs a technique similar to that proposed by Mohan and Mackie. The pencil beam model, suggested by Ahnesjö et al. (1992), involves an integration of analytic pencil beam kernels. The kernels may be described through the sum of two kernels: one representing primary and the other secondary polyenergetic doses:

$$\frac{k_{p+s}}{\rho}(r,z) = \frac{A_z e^{-a_z r}}{r} + \frac{B_z e^{-b_z r}}{r} .$$

The parameters A_z, Bz a_z, and b_z are in fact generated for specific beams through a characterisation of the beam's energy spectra [Ahnesjö et al. 1989]. These values are stored and, therefore, allows for faster computation times through the use of look up tables. The field and penumbra are determined by convoluting the primary portion of the above kernel with a gaussian source distribution. In practice, some approximations are made such that a perturbation term is added to the total primary plus scatter kernel. The above equation produces DPB distributions equivalent to those generated from Monte Carlo simulation. Similar to the contamination distribution in Mackie's model, a charged particle contamination kernel is approximated through a radial gaussian function coupled with an exponential drop off with depth. Nillson et al. (1981) found that photon contamination, or photons different from the geometric beam, stem primarily from the flattening filter and primary collimator. The dose distribution from contaminants is approximated through a gaussian like function, which can then be added to the computed distribution separately.

The kernels are integrated separately for each voxel and multiplied by the fluence to yield dose. As opposed to an actual convolution, the kernel distribution is integrated through the Sievert integrals of the first and second kind in order to account for irregular field shapes. The general shape of the Sievert integrals are given as,

$$\int_0^{\theta} e^{-(x/\cos(t))^n} dt ,$$

where n=1 and 2 for first and second order Seivert integrals, respectively. The Sievert integral implementation readily handles contour variations and irregular field sizes. The use of the Sievert integrals allows for faster computation times through using precomputed look-up tables.

Inhomogeneities in the Helax algorithm are modeled through corrections of both the primary and scatter dose. Primaries are corrected in the same manner as that described in Mohan's model where the radiological pathlength is evaluated from the scattering site and the mean attenuation along the pathlength. Scatter dose is computed by multiplying the scatter from a homogeneous phantom with a correction factor. The scatter dose contribution increases with depth. Thus, a correction factor is applied to the homogeneous dose that consists of the ratio of radiological (z_r) and geometric (z) depths multiplied by a transmission factor:

$$CF = \frac{z_r}{z} \exp\left[-\langle\mu\rangle(z_r - z)\right] .$$

The value of $\langle\mu\rangle$ is empirically chosen as 0.8μ, where μ is the narrow beam attenuation coefficient in the medium.

1 HELAX TMS: Raddix, Uppsala, Sweden

The model performs very well for homogeneous phantoms and is well suited to patient geometries and typical clinical beams. For non-homogeneous phantoms, however, the model fails to include lateral scatter efficiently. Knöös et al. found deviations of up to 5% and 14% for 4 and 18 MV photons respectively. Similar errors have been reported at the Cross Cancer Institute. The error is most likely greater than 5 % for the 6 MV photons used at the Cross Cancer Institute since the laterally scattered electrons increase in range as energy increases. Thus, Ahnesjö's pencil beam algorithm does not perform well when lateral charged particle equilibrium is violated.

Primary and
Secondary Isodoses

Multiple Scatter Isodoses
(normalised to it's maximum)

Coaxial Cone
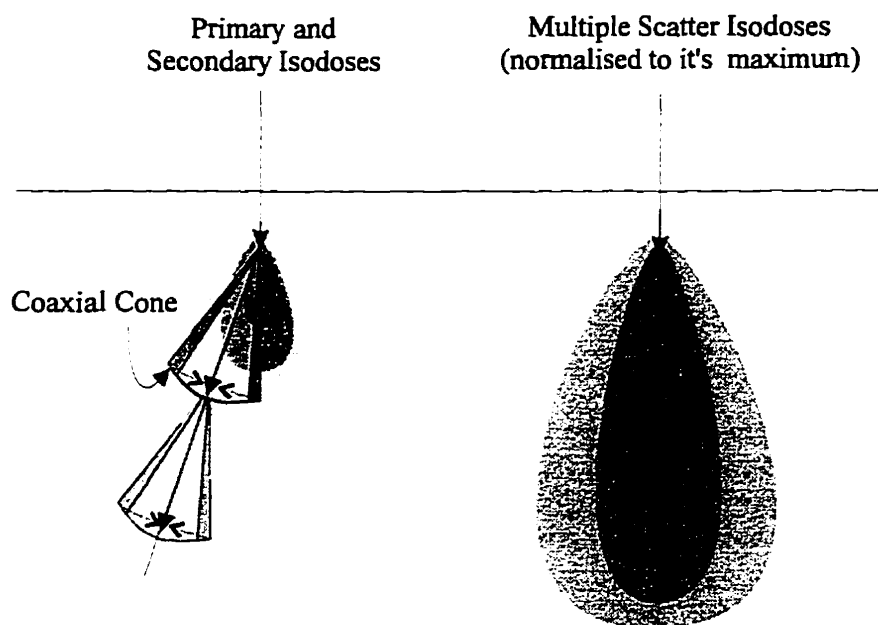
Figure 3.5: Relative distributions of primary, secondary and multiply scattered photons, normalised to their respective maximums.

The algorithm can be improved by employing a collapsed cone approximation [Ahnesjö 1989]. In this approximation, the computation of dose is carried out identical to the pencil beam algorithm mentioned earlier with the exception to the method inhomogeneity corrections are performed. The scaling of radiological pathlengths from sampling the density between the calculation site and scatter site assumes that each voxel along the ray contributes an equal amount of dose. Generally, this is untrue; multiply scattered particles contribute more dose further from the calculation point [Mackie et al. 1984]. As a consequence, the relative amount of dose due to multiple scattering using this scaling method is underestimated.

In the collapsed cone approximation, the energy released into coaxial cones along a given raylength is transported and attenuated to a point along the raylength (see Figure 3.5). The energy deposited within these coaxial cones can be computed through a convolution of the primary and scatter pencil beam with the fluence profile multiplied by the density. The primary and scatter contributions of the inhomogeneity are modeled separately; therefore, the

algorithm can predict dose in regions of disequilibrium. The scatter dose along the raylengths is then summed to provide the total scatter contribution. In order to avoid oversampling along each ray, a voxel's contribution to dose along the axis is counted only once. The correct dose can be computed directly as opposed to performing a correction factor to the homogeneous distribution, such as the Batho and ETAR algorithms. Compared to Monte Carlo simulations, the collapsed cone algorithm proves much better at predicting dose at lateral interfaces and in heterogeneous media than scaling radiological pathlengths.

The most computationally extensive of all dose calculation algorithms is the Monte Carlo simulation [Ford et al. 1978, Rogers 1982, Rogers et al. 1995]. In this method, the interactions of the photon are based on the Klein & Nishina and other cross sections. The trajectory of the ionised electron is followed and the number of ionisations are counted in each voxel. The direction of the scattered photon is selected from predefined "scattering rules", which are determined by the interaction cross sections. Doses to voxels are scored depending on the number of ionisations within each voxel. Range straggling effects of the electrons can be modeled by performing similar calculations for the ionised electrons. The accuracy of Monte Carlo simulations is equal to or less than 2% depending on the level of physical interactions modeled. Obviously, the degree of accuracy is at the expense of time; computation times may take on the order of days to complete. The same type of problems encountered for other calculation techniques are overlooked in this method since the limitations of accuracy depend entirely on the sophistication and detail of physical modeling.

3.2.3 Treatment Planning

As mentioned earlier, the optimisation of a treatment plan may be defined as an optimisation problem where an objective function is either maximised or minimised subject to various constraints. These constraints may include, but are not limited to, functions, such as average dose to the target, dose volume histograms, and normal tissue complication probability (Described in Section 3.3). There exists a wide variety of optimisation routines found in the literature [Graffman et al. 1975, Brahme 1988, Bortfeld et al. 1990, Holmes et al. 1994]. The most effective routines employ both biological and physical constraints [Niemerko et al. 1992]. A desirable characteristic is that the routine be efficient for three dimensional planning: The routine should be robust (reproducible), and it should seek solutions rapidly.

There are two approaches that one may take when optimising a dose distribution. One approach, coined as inverse planning, is to define the desired distributions and compute the number of beams, along with their dimensions, gantry angles, modulation, etc., required to create the distribution [Brahme 1988, Morrill et al. 1990, Desobry et al. 1991, Holmes et al. 1994]. Inverse planning algorithms generally employ minimisation algroithms such as Simplex , Least Squares, or Simulated Annealing [Press et al. 1988]. The commercially available Nomos[2] Peacock system creates a uniform distribution by modulating thin pencil beam of radiation that rotate 180° around the patient. These types of systems are generally unavailable to most clinics because of their expense and its efficacy is still yet to be fully evaluated.

The other approach for optimisation is to "forward" plan; that is, a general knowledge of a satisfactory treatment plan is known apriori through experience or educated guesses. The planner then iterates through combinations of the various planning parameters to create the

2 Nomos Corporation, Sewickley, PA

desired distribution. This approach is used the most in clinical settings because it is easy to implement in routine treatment planning; all that is required is a reliable dose calculation engine and an experienced treatment planner. When deciding on potential gantry angles, the planner will know that it would not be appropriate to have beam entry points that traverse directly through radio-sensitive organs; in the inverse planning approach, the algorithm may produce acceptable a PTV distribution but an unacceptable normal tissue dose, gantry angle, or produce solutions that are not clinically feasible to implement (such as a high number of beams with small weightings). The forward approach allows the planner the freedom to impose both objective and subjective constraints as desired in the plan. This freedom comes at the expense of time and, therefore, potentially less than optimal distributions.

A reasonable compromise can be achieved between these two approaches by specifying certain parameters by the treatment planner while allowing computer algorithms to minimise a less complex objective function. The time required to produce the desired distribution becomes greatly minimised by providing a "good guess". This also avoids creating an optimisation algorithm that encompasses all the potential degrees of freedom for 3D-CRT.

3.2.4 Optimisation Through the Gradient Vector Approach.

A simple mathematical method that ensures a uniform dose distribution at depth has been proposed by Sonntag (1975) and again by Sherouse (1993). To describe this method, we define the patient and beam coordinate systems as in Figure 3.5. Within this coordinate system, we represent each incident beam with a vector. Each beam has a gantry (φ), table (θ), wedge (ϕ), and collimator (ω) angle, and beam weighting. The beam's vector may be found by computing the gradient of the scalar dose field. A vector is used to represent the beam's dose distribution within the patient, where each vector has its origin aligned at isocentre. The magnitude of the vector will depend on several factors: beam size, percentage depth dose, density of target material, and amount of lung tissue traversed. The angle of the vector will depend on the angles θ, φ, ϕ, and ω.

Using the patient coordinate system, each "gradient" vector can be decomposed into two components: an axial component, which points toward the source, and a transaxial (or longitudinal) component that points perpendicular to the axial vector. We assume that a wedge only affects the transaxial component of the gradient vector. For instance, let us consider a treatment plan consisting of a single beam, θ, φ, ω all equal to zero, and ϕ equal to 30 degrees. First, we normalise the magnitudes of the beams according to the beam weightings and compute the magnitudes of the axial and transaxial components. In this case, the normalisation is trivial since there is only one beam to consider. Next, we compute the axial and transaxial components after finding the magnitude of the vector. For this example, we have the following axial and transaxial vectors:

$$|\vec{v}| = \sqrt{\vec{v}_{transaxial}^2 + \vec{v}_{axial}^2} = 1 \text{ , and}$$

$$|\vec{v}_{axial}| = \cos(\phi) = \cos(30) = \frac{\sqrt{3}}{2}, \text{and } |\vec{v}_{transaxial}| = \sin(\phi) = \sin(30) = \frac{1}{2}.$$

$$\text{Thus, } \vec{v}_{axial} = (\sqrt{3} / 2)\hat{i}, \text{ and } \vec{v}_{transaxial} = (1 / 2)\hat{j}.$$

Each beam in the treatment plan is decomposed into its axial and transaxial components. We assume that the sum of each beam's axial and transaxial components gives the net dose gradient of the combined fields.
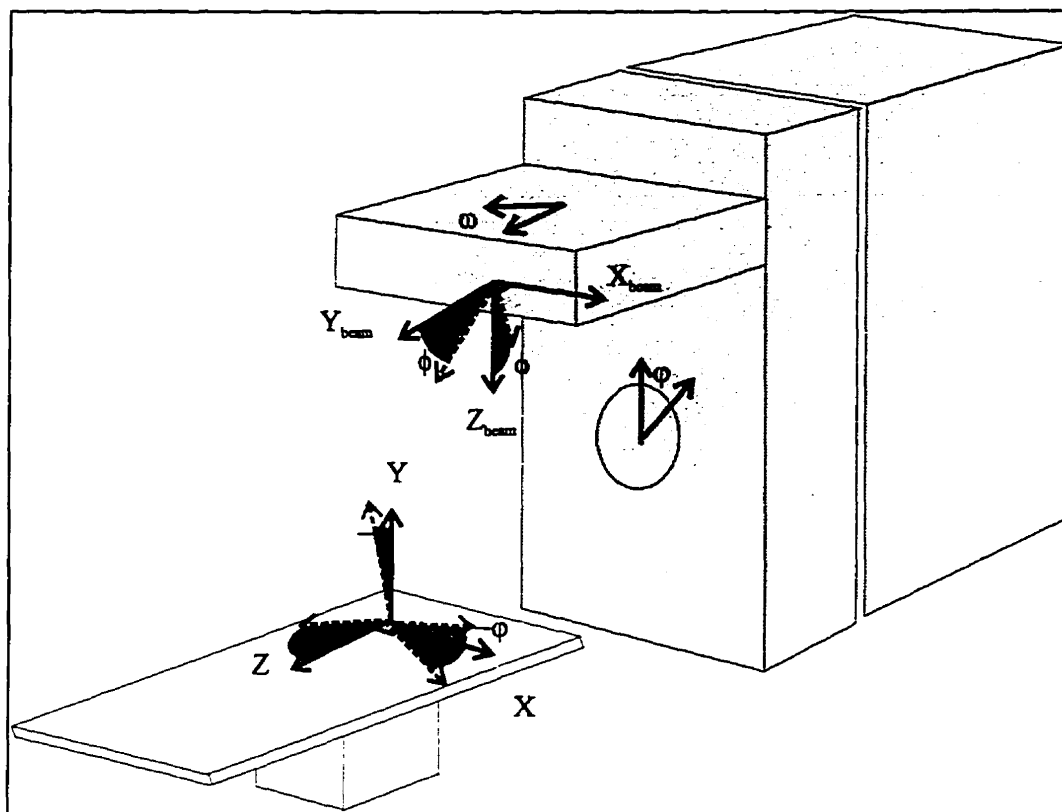
Figure 3.6: Definition of patient and beam coordinate systems.

It has been demonstrated that for water phantoms, the gradient vector approach can generate high dose gradients at beam intersection points and handle three dimensional beam configurations efficiently. The efficiency of this method in clinical practice remains to be investigated.

3.3 Treatment Planning Evaluation

After the treatment plan is devised and dose calculations are performed, the treatment plan is evaluated. The plan is scored, or judged, based on the merits and demerits of the treatment plan. Up until the last several years, treatment plans were scored by either the clinician, dosimetrist, and/or physicist without much quantitative analysis. This was acceptable since the conventional approach was restricted to a two dimensional analysis and visually inspecting the merits and demerits of a treatment plan is much easier than for a three dimensional plan. However, three dimensional dose computations generate an overwhelming

amount of dose information. Therefore, more quantitative tools are necessary to collate the three dimensional dose information.

Some of the criteria used in assessing dose plans are dose to the target, homogeneity of dose to the target, relative dose to peripheral structures, distance between high dose regions and critical structures, and dose to critical organs. In some instances, a single factor may be the constraint in assessing the treatment plan. For instance, a beam arrangement may produce high coverage of the target but may involve irradiating an organ higher than its irradiation tolerance.

In three dimensions, qualitatively assessing the merits and demerits of a treatment plan becomes difficult due to the multi-dimensional information. One can, in principle, assess individual slices of the treatment plan in a systematic fashion, however, this would be extremely time consuming. Therefore, quantitative tools need to be developed to accurately assess the merits and demerits of a three dimensional treatment plan. These tools may be as simple, like the average or range of doses to the PTV, or more complicated, like the dose volume histogram. Some of these quantitative tools are now discussed.

3.3.1 Normal Tissue Complication Probability and Tumor Control Probability

There is a vast amount of data suggesting that the degree of damage done to the genetic material of cells determines its probability of survival [Steel et al. 1989]. The length of the "tracks" of excited and ionised atoms and molecules is primarily determined by the energy of the incident charged particle. In general, the greater the charge of the incident particle, the more dense the degree of ionisation per unit length, or linear energy transfer. A typical value for linear energy transfer would be 0.25 keV/μm for an electron set in motion from a Co-60 source.

Approximately 70-85% of the mass in humans consists as water. Because of its abundance, water absorbs the majority of energy imparted from radiation treatment. Upon irradiation, a water molecule may transform into an ion pair in one of two ways. The first way is through ionisation of one of the water molecule's electrons, resulting in a positively charged molecule. The second method through which the molecule may attain charge is through electron capture. For the second method, the resulting ions are highly unstable and dissociate quickly to form a free radical and another ion. Both ions have an extremely short lifetime and do not contribute any significant biological damage. The free radicals, however, can act as strong reducing or oxidising agents. These free radicals can combine directly with macromolecules, such as DNA, to change their molecular composition. The structural changes may range from a hydrogen bond breakage, molecular degradation or breakage, to inter- or intra-molecular cross linking. As a result of such molecular deformations, a cell's ability to proliferate becomes compromised and the cell ceases to function properly or disintegrates.

Macroscopically, the cell's ability to retain its proliferating capacity can be illustrated on what is commonly referred to as a cell survival curve. On such a curve, surviving fraction is plotted on the vertical axis and the dose delivered to a specific cell population is plotted on the horizontal axis. Figure 3.6 illustrates the typical shape of a cell survival curve.

There are a number of models that mathematically describe cell survival curves. Since effectiveness of radiation to cancer cells is stochastic in nature, these models revolve around the random nature of radiation energy deposition [Zagars et al. 1986]. A common model used

to describe cell survival is the linear-quadratic model [Chadwick et al. 1973]. In this model, the number of cells surviving radiation, N, is given by the following equation:

$$N = N_o \exp\left[-\left(\alpha D + \beta D^2\right)\right],$$

where N_o is the original number of cells, D is the dose delivered, and α and β are empirically found parameters for different cell types.
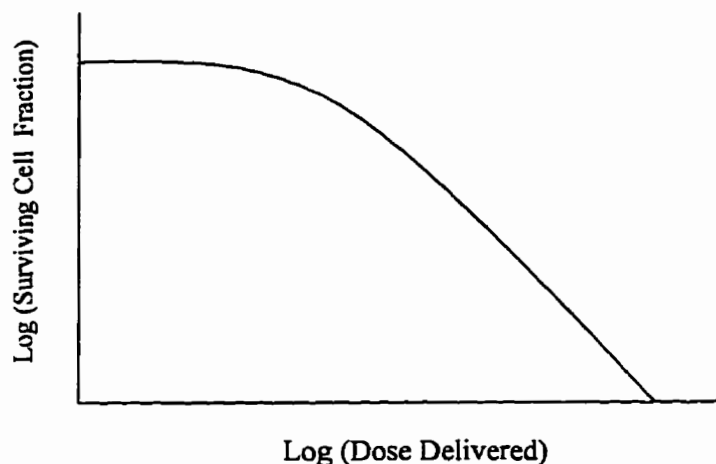
Figure 3.7: **Shape of a typical cell survival curve. Both the horizontal and vertical axes are plotted on a logarithmic scale.**

It must be stressed that although cell type survival curves may be mathematically fit, it is not possible to model the behaviour of all cell types. This is due to the fact that survival curves alone are not a precise measure that can distinguish between the various mathematical models; that is, similar equations can be empirically derived with completely different biological assumptions built into the model. Several unique equations may be used to describe the behaviour of a particular cell's radiation response and each equation may contain uncommon radiobiological parameters.

Much like the survival curve, we can display a cell's response to radiation through a dose response curve. A dose response curve has probability of cellular complication or death on the vertical axis and dose delivered on the horizontal axis. Measures of response may range from cellular death within a petri dish to the fraction of patients with complications after irradiation. As the response becomes larger, or more macroscopic, more factors are required to adequately model the dose response behaviour. The shape of the dose response curve will look much like that of Figure 3.8.

One of the many biological endpoints that may be used in assessing tumour control is the tumour control probability. The tumour control probability is a stochastic measure of the probability of complication a volume of interest receives under certain treatment parameters and dose levels. This measure of response is much more macroscopic than those found for cell specific dose response curves, and thus involves more parameters when it is modeled.

Modeling the tumour control probability would require accounting for a host of biological factors that describe the response of cancer cells to radiation. There are many sophisticated models that predict the dose response characteristics under various planning parameters [Brock et al. 1989]. Some factors involved in computing the tumour control probability include physiological parameters, such as size and extent of the tumour, cell kinetics of cancer type, spatial distribution of the cancer cell, cellular growth rate, while others include treatment planning parameters, such as fractionation schemes, and dose homogeneity to the target.

Similar to the tumour control probability, the normal tissue complication probability provides a stochastic measure of the probability of clinical complications to the volume of interest. The normal tissue complication probability is a function of various factors, such as the beam parameters (energy, direction, and beam characteristics), dose delivered, volume of target, radiosensitivity of the volume of interest, disease type and other clinical factors. One model of calculating the normal tissue complication probability is the Lyman four parameter model [Lyman et al. 1987] where,

$$NTCP = \frac{1}{\sqrt{2\pi}} \int_{-\infty}^{t} \exp\left(\frac{-t'^2}{2}\right) dt' \quad \text{(Equation 3.2a),}$$

$$t = \frac{(D - TD_{50}(v))}{m \cdot TD_{50}(v)} \quad \text{(Equation 3.2b),}$$

$$TD_{50}(1) = TD_{50}(v) \cdot v^n \quad \text{(Equation 3.2c), and}$$

$$v = V / V_{ref} \quad \text{(Equation 3.2d).}$$

The normal tissue complication probability for a volume, V, receiving a dose, D is defined through an error function with several empirically fit parameters that vary with the volume of interest under risk assessment. $TD_{50}(1)$ is the dose to the volume of interest when 100% of the organ produces a 50% complication probability, $TD_{50}(v)$ is the dose to partial volume, v, producing a similar complication probability, and m and n are parameters that are empirically fit from normal tissue tolerance data. The Lyman model assumes a logarithmic dose-response relationship with the amount of volume irradiated. The parameter m is a measure of the dose sensitivity of the organ, whereas n is a measure of the volume sensitivity. The dimensionless parameters m and n have been calculated by curve-fitting the complication rates for most vital organs subject to irradiation [Burman et al. 1991]. With respect to lung treatment, the relevant organs are the skin, lung tissue, heart, spinal cord, esophagus, and possibly the thyroid, liver, and kidneys. A table of the parameters for various organs, taken from Burman et al., is provided below. To understand the table let us take an example. If two thirds of a patient's lungs were irradiated with a dose of 30 Gy, there would be approximately a 5% chance of complications within 5 years. If the dose were increased to 40 Gy, there would be a 50% chance of complications within 5 years.

	Fitted Parameters		TD5/5 (Gy)			TD50/5 (Gy)		
Organ	n	m	1/3	2/3	1	1/3	2/3	1
Skin (100 cm²)	0.1	0.12	70	60	55	-	-	70
Lung (both)	0.87	0.18	45	30	17.5	65	40	24.5
Heart	0.35	0.1	60	45	40	70	55	48
Spinal cord (20 cm)	0.05	0.175	50	50	47	70	70	66.5
Esophagus	0.06	0.11	60	58	55	72	70	68
Thyroid	0.22	0.26	-	-	45	-	-	80
Kidney (both)	0.7	0.1	50	30	23	-	40	28
Liver	0.32	0.15	50	35	30	55	45	40

Table 3.1: List of n and m parameters along with tolerance data. This data is reproduced from Emami et al. and Burman et al. (1991).

In Figure 3.8 are replicated normal tissue complication probabilities from the data generated by Burman et al. For Figure 3.8, values of n=0.87, m=0.18 are used to describe the sigmoidal curve.

Measuring normal tissue complication probability may be done retroactively by examining delivered treatment plans along with associated complication rates of lung cancer patients. This was in fact done for the data generated by Burman et al. Since the calculation of tumour control probability is significantly more involved than a normal tissue complication probability calculation, a precautionary evaluating technique would be to impose a minimising constraint on the normal tissue complication probability and allow the dose to the target to increase to a level where normal tissue complication probabilities remain acceptable.

There exist other methods to calculate normal tissue complication probability. One method is the critical volume model [Niemierko et al. 1993], which is considerably more complicated and involves examining the volume of interest in terms of its functionality and structure. The Lyman model was used in this thesis work because of its wide usage and simplicity. Also, data is readily available for describing dose-response relationships with respect to specific organs.

It should be noted that, in general, generating a dose response curve, such as the NTCP curve, implies a precision that is impossible to attain through clinical testing. There are several reasons why this is true. First, the dose response curve for a particular cancer type is has unique parameters, such as tumour cell density, size, distribution, position, and cellular kinetics. Extrapolating results of one patient response to another's clinical outcome is only valid if the two plans are identical. Two patients having the same cancer type, shape, cellular distribution, and similar physiology, anatomy, and functionality is extremely unlikely. Second, the relationships between dose and a tumour's type, shape and position within the lung are unclear. This has yet to be fully investigated. Third, the solution from mathematically modeling the behaviour of the dose response is not unique; each model may have specific and uncommon radiobiolgical parameters.
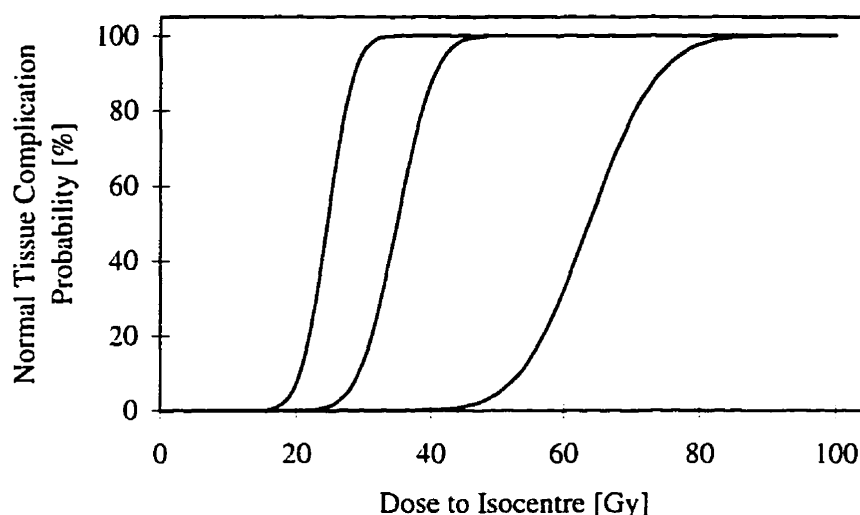
Figure 3.8: Normal tissue complication probabilities of lung as generated from the Kutcher-Burman-Lyman model. Shown are normal tissue complications of lung where effective volumes are 1, 2/3 and 1/3 from left to right.

3.3.2 Dose Volume Histogram

The dose volume histogram (DVH) is a two dimensional descriptor of the amount of dose given to a volume of interest [Dryzmala et al. 1991] . The two dimensional histogram amalgamates the three dimensional dose distribution information of treatment plan by plotting partial irradiated volume versus dose. The DVHs used in treatment plans are actually cumulative DVHs, however, over time the term cumulative has been dropped and the true histogram is called a differential DVH. To illustrate how the dose volume histogram is produced, Figure 1.1 shows a slice of a 3D treatment plan. The dose has been computed for this plan and a volume of interest, such as the lung is defined. The volume of the lungs can be computed as the number of voxels within the lung multiplied by the volume per voxel. The volume of the lungs are 3263 cm^3 in this case. The DVH may be computed through a loop like;

```
for every value of dose(i) encountered,
     DVH(i) = the total number of voxels within the VOI
                            receiving a dose i
end
```

The result of this computation produces the differential dose volume histogram, which is displayed in Figure 3.9. The cumulative distribution may be computed through a logic loop such as;

```
for every value of dose bin (i) in the differential DVH,
     Cumulative DVH (i) = DVH(i)
                              - cumulative sum of DVH(First value to i)
end
```

After the cumulative DVH is computed, it may be normalised such that it is a function of relative dose. Shown in Figures 3.9 and 3.10 are unnormalised examples of a DVH and differential DVH.

Scoring criteria based on the evaluation of the DVH is simple if the DVH curves do not intersect. However, this is not always the case; two similar treatment plans may produce DVH lines that indeed intersect, such as that observed for the lower curves in Figure 5.24. A simple method of distinguishing plan merits and/or demerits is to compute an equivalent volume that receives a uniform dose, such as the dose to the target volume. If a volume of interest receives a uniform dose equal to the prescribed dose, effective volume becomes unity. Similarly, an effective volume of 0.5 is equivalent to the total volume of interest receiving exactly half of the prescribed dose, or equivalently, exactly half of the volume of interest receiving the prescribed dose. Currently, there are two methods to calculate an effective volume: the interpolation technique [Lyman et al. 1987], and the histogram reduction method [Burman et al. 1991].
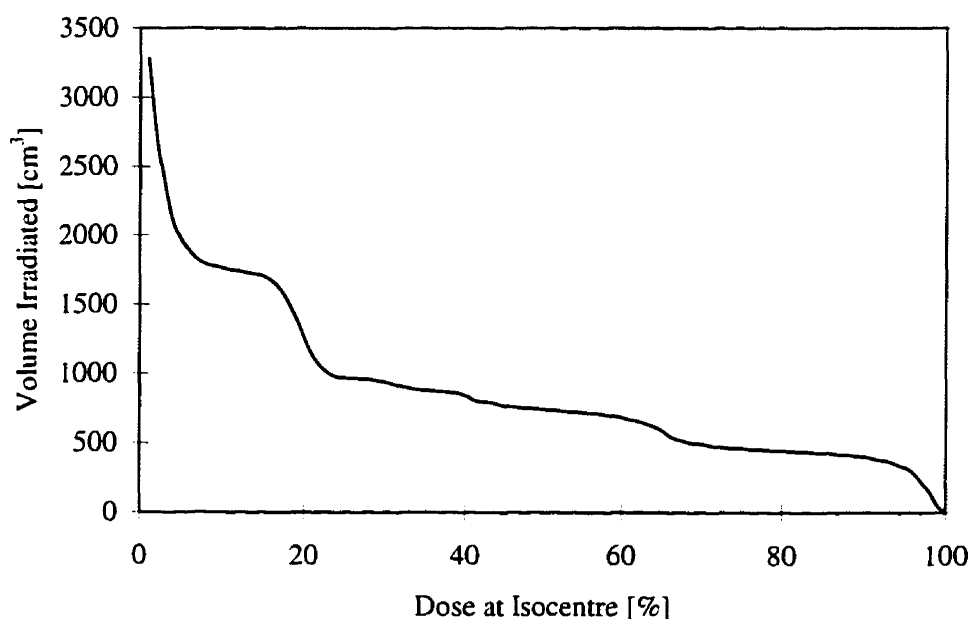
Figure 3.9: Cumulative dose volume histogram.
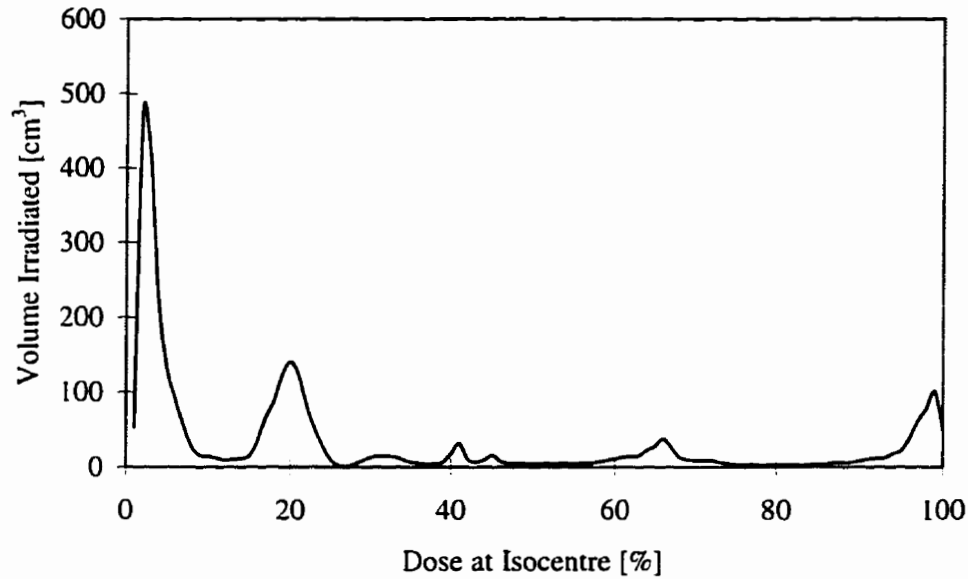
Figure 3.10: Differential dose volume histogram.

The interpolation transforms the non-uniform dose volume histogram to an equivalent uniform dose volume histogram having a dose equal to or less than the maximum dose to the volume of interest. In this model, a complication response function, $P(D,V)$, needs to be specified apriori. A cumulative DVH is generated for the treatment plan and $P(D_m,V_m)$ and $P(D_{m-1},V_{m-1})$ is computed with the model (see Figure 3.11). If V_m is small, we assume that $P(D_m,V_m) \cong P(D_{m-1},V_{m-1})$. In addition, if $V_{m-1} \cong V_m$, then a complication for a dose D', that lies between D_m and D_{m-1}, is approximated through a weighted average of $P(D_m,V_m)$ and $P(D_{m-1},V_{m-1})$, depending on the relative amounts of volume irradiated:

$$P(D', V_i) = \frac{(V_i - V_m)}{V_i} \cdot P(D_i, V_i) + \frac{V_m}{V_i} \cdot P(D_m, V_i).$$

The calculation of $P(D',V_i)$ is stored and an identical probability calculation is performed for a dose less than the maximum (as determined by the dose bin size). The process is repeated until a single dose value is obtained for the uniform histogram. The result is a probability of complication for the volume of interest with a uniformly delivered dose D'.
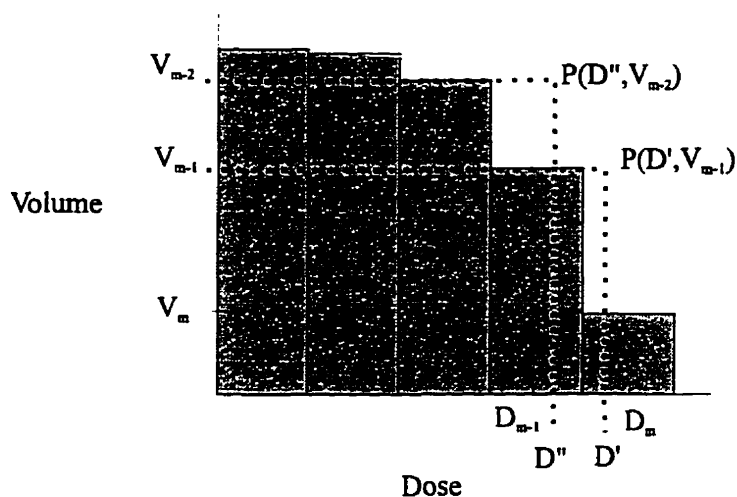
Figure 3.11: Determination of effective dose through Lyman's interpolation method.

The second method utilises the "true" dose volume histogram, or the differential dose volume histogram, such as that displayed in Figure 3.9, and is referred to as the effective volume method [Kutcher et al. 1991]. In this method, we assume that each volume element in the differential dose volume histogram has the same dose response characteristics as the entire organ. The normal tissue complication probability is computed using Lyman's suggested four parameter model (See Equations 3.2a-d). For each volume there is an associated dose received, and to model the dose response, we calculate an effective volume irradiated for a dose bin:

$$\left(\Delta V_{eff}\right)_i = \Delta V_i \left(\frac{D_i}{D_m}\right)^{1/n} ,$$

where D_m is the maximum dose received, D_i is the dose received to the volume element V_i, and n is the parameter that describes the dose-volume sensitivity for the volume of interest. The calculation is repeated for all dose bins and the effective volumes are computed. Summing the total effective volumes produces the total effective dose receiving dose D_m:

$$V_{eff} = \sum_i \Delta V_i \left(\frac{D_i}{D_m}\right)^{1/n} \quad \text{(Equation 3.3)}.$$

Note that D_m could correspond to any specified dose; however, if D_m is chosen to be the maximum dose, V_{eff} is be ensured to be less than or equal to 1.

Kutcher's histogram reduction method incorporates various considerations for treatment planning optimisation: effects of both hot and cold spots in the volume of interest, dose-volume sensitivity of volume of interest, quantitatively evaluating dose volume histograms that intersect, and ensuring that the normal tissue complication probability is less for smaller irradiated volumes. For these reasons, Kutcher's histogram reduction method was employed when computing the effective volume in this thesis.

3.3.3 Scoring of Treatment Plans

Quantitatively measuring the advantages and disadvantages of treatment plans is greatly facilitated through the use of functions such as the dose volume histogram, normal tissue complication probability and tumour control probability. These functions may be used independently or dependently in optimisation routines for evaluating treatment plans.

The objective function may be either maximised or minimised, depending on the scoring criteria used. If the biological endpoint used to evaluate the treatment plan is the tumour control probability, a maximum solution would be required, whereas if the normal tissue complication probabilities were used, a minimisation of the normal tissue complication probability would be sought provided the constraints are satisfied. Some potential constraint functions are dose homogeneity to the target, critical tissue dose limits, and optimal beam entry points and configurations. It is important to recognise that in radiotherapy, structural and functional tumour response is stochastic by nature and, therefore, difficult to incorporate into linearly programmed optimisation routines.

It must be stressed that these tools (normal tissue and tumor control probabilities, and dose volume histogram) used in comparing treatment plans are not quantitative descriptors of probable treatment outcomes. The data used in generating normal tissue complication probabilities are subject to error and so should only be used to compare plans; they can not be used to predict probable outcomes given a specific treatment planning configuration.

3.4 Treatment Delivery

After treatment plan is optimised and simulated, the patient is now ready to undergo treatment. Many lung cancer treatments are isocentric: a fixed point is normally defined within the tumour volume and the gantry rotates at a fixed radius from that point. All treatment plans generated in this thesis assume an isocentric configuration.

After calculating the dose (in Gray) to the isocentre, the total dose is fractionated according to the durations of daily treatment times and the total number of sessions. As an example, a dose of 60 Gray delivered over 6 weeks is not uncommon for a lung cancer treatment plan. If there are three beams in the treatment plan with equal weighting, each beam delivers 20 Gray. If the treatment is to be given over the course of six weeks (or 30 days), this would amount to 0.67 Gray per beam per day. In our treatment facilities, delivering 2.0 Gray would require approximately 25 seconds. As discussed later in this thesis, the period of the respiratory cycle for lung cancer patients is approximately 3.2 s. Some patients may have shorter or faster respiratory periods. In cases of the latter, it would not be unreasonable to question whether respiration may alter deposited dose.

3.4.1 Relevant Factors Regarding Linear Accelerators

A thorough discussion regarding the design and advances of linear accelerators may be found elsewhere [Karzmark 1984]. Since the focus of this thesis work is the relevance of respiratory motion in the treatment of lung cancer, there are a few factors regarding linear accelerators that are worth noting.

Photon fields are normally designed to be as uniform as possible. The overall effect of respiratory motion to a uniform radiation field is essentially a blurring, or convolution, of the

delivered dose within the patient. The kernel spread function depends primarily on the period of motion and treatment, size of the field and target, and density distribution of the planning target volume. Penumbral widenings have been reported due to the effects of respiratory motion [Jacobs et al. 1996, Ohara et al. 1989].

Accounting for respiratory motion at the treatment delivery stage is more plausible by recreating a static treatment scenario. This can be accomplished by simply gating the portal machine to the respiratory cycle. Several investigators have reported some success in accomplishing gated radiotherapy [Huang et al. 1996, Kubo et al. 1996, Ohara et al. 1989]. More will follow regarding this in Chapter 6.

3.4.2 Beam Modifying Devices

Two beam modifying devices that are relevant in this thesis work are wedges and compensators. Compensators are normally made from wax, cerrobend or lead whereas wedges may be constructed from steel and/or lead. These devices may be manually inserted in designated slots by the portal head. These beam modifying devices are strategically designed to create an isodose effect below the surface of the patient.

3.4.2.1 Wedges

A wedge is a beam attenuating device that tilts isodose lines to a specific angle some distance below the surface. Shown in Figure 3.12 is the effect of a 45 degree wedge on a homogeneous water like phantom. The wedge may be calibrated to create the appropriate isodose angle effect at 10 cm below the surface for a homogeneous phantom. Due to beam hardening, and additional scatter contributions at depth, the effective wedge angle is slightly greater above the reference depth and decreases as the depth increases. A 45L wedge tilts the isodoses counterclockwise with respect to the beam's central axis, where a 45R rotates the isodoses clockwise.

Tilted isodose lines may also be created by dynamically moving the jaws of the collimator while the beam is on. This technique is commonly referred to as dynamic wedge [Kijewski et al. 1978]. A dynamic wedge is produced when one of the jaws in the collimator moves across the field, at a variable speed, until the jaws are fully closed.

3.4.2.2 Compensators

To account for irregular surfaces, a bolus may be placed on the surface of the patient as shown in Figure 3.13a. Since the bolus has the same attenuation characteristics as that of normal tissue, the photon interactions within the patient and phantom be closely matched. Thus, using a bolus will create a more uniform distribution at depth given the existence of surface irregularities. With the bolus in place, there will be a buildup of dose at the surface, just as one would normally expect. However, the skin, which lays a significant distance below the bolus surface, will receive a higher dose than if the bolus was not there. In order to spare the skin this additional dose, the bolus may be placed above the patients' skin [Ellis et al. 1959]. By placing the bolus closer to the beam source, it becomes necessary to geometrically distort the bolus's shape so as to account for beam divergence (see Figure 3.13b). The resulting geometrically retracted bolus is known as a missing tissue compensator. The missing tissue compensator can be placed a significant distance away from the source in order to take advantage of the skin sparing effect.

At the Cross Cancer Institute, compensators are normally constructed out of pliable water equivalent material, such as wax, using a computer operated milling machine that can cut compensator molds to millimetre accuracy. These molds may consist of single or multiple styrofoam blocks, which have a density roughly that of air, and can be mounted at the linac port.
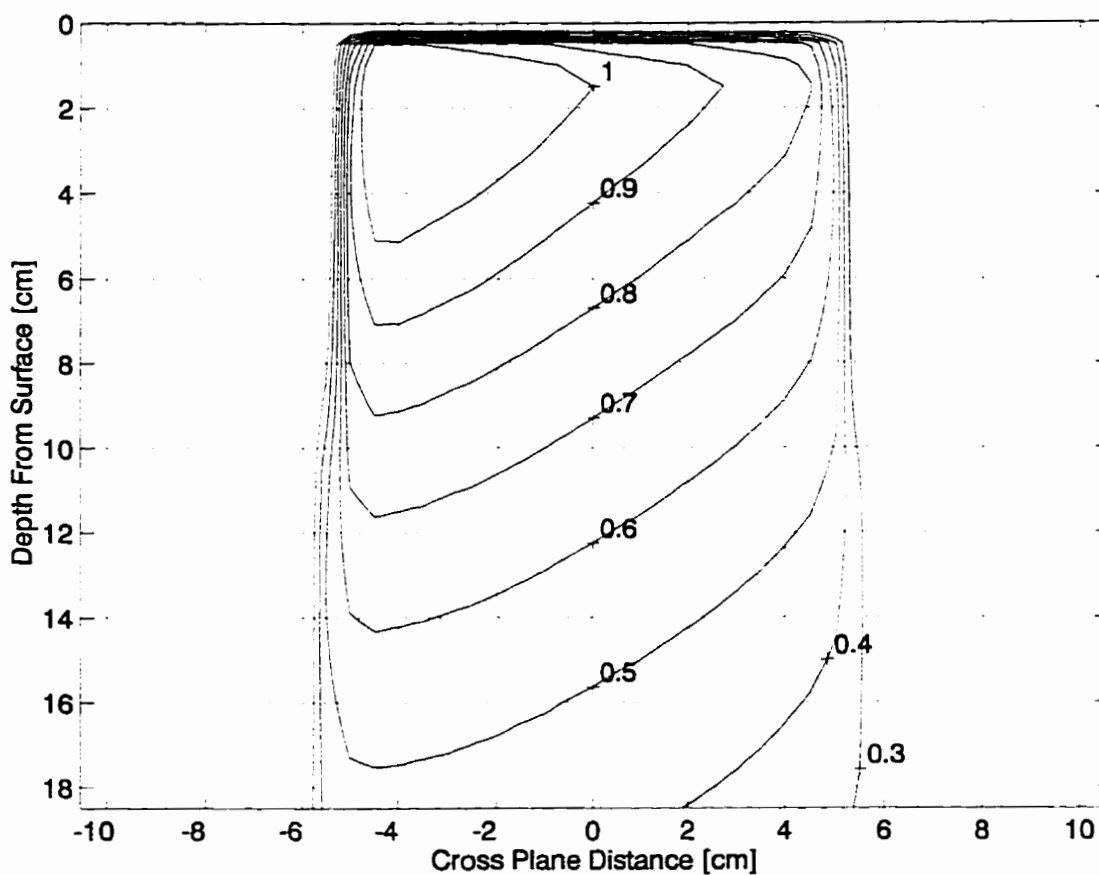
Figure 3.12: Dose distribution as generated by a physical 45L degree wedge in a 10 x 10 cm field of 6MV photons, incident to a homogeneous water phantom. The dose is normalised to the maximum dose along the central axis -which occurs 1.5 cm below the surface- for 6 MV photons.
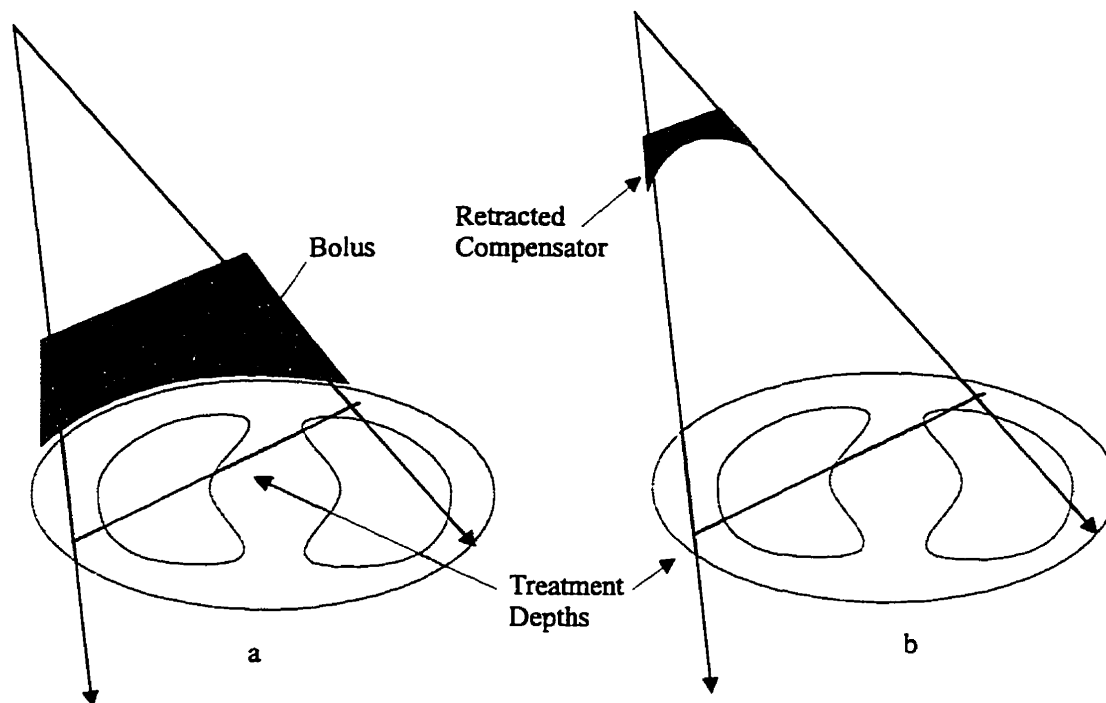
Figure 3.13a & 3.13b: A bolus, a, and a retracted compensator, b. Both devices achieve the required isodose at the specified treatment depth.

The construction of the compensator at the Cross Cancer Institute is accomplished by first digitising the surface contour. A magnetic probe is used to measure the relative height of various points of the contour and the acquired points are interpolated to create a three dimensional surface contour of the anatomy. The missing tissue compensator then acts as an equivalent bolus, using as minimal amount of material as necessary, to create a uniform dose below the surface of the patient. After the styrofoam is cut, wax is packed into the styrofoam block and mounted on an accessory tray that fits into the linear accelerator portal.

The variation of surface contours is not the only factor that may change the beam intensity as it passes through matter. Internal structures that have densities different from uniform tissue will change the photon attenuation and, therefore, the dose deposited.

3.4.2.3 Design of Missing Tissue Compensators

There are many methods to construct a compensator [Mageras et al. 1991, Robinson et al. 1990, Faddegon et al. 1988, Shragge et al. 1981, Cunningham et al. 1976, Hall et al. 1961]. Some methods employ a more stringent approach to account for scatter, whereas some are simple iteration algorithms. Outlined below are two methods used to construct a compensator both of which are relevant in this thesis work.

The first method employs a geometrical retraction of the missing tissue and a scaling of the retracted compensator to account for lack of scatter [Ansbacher et al. 1992, Van de Geijn 1965]. As a crude approximation, we assume that the energy fluence attenuates exponentially within the compensator. Therefore, the amount of material necessary to attenuate the beam is determined by the equation,

$$\Psi = \Psi_o \exp(-\mu t), \text{ (Equation 3.4)}$$

where Ψ_o is the energy fluence entering the medium, Ψ is the energy fluence leaving the medium, μ is the linear attenuation coefficient of the medium, and t is the thickness of the material. For a varied geometry, such as that given in Figure 3.12, the compensator is designed to create a plane of uniform dose below the surface at some reference depth, d. The amount of material necessary to attenuate the photons such that a uniform dose is delivered at the distance ssd + d can be derived from the above equation. Rearranging Equation 3.4 to isolate thickness of material gives,

$$t = \ln(\Psi / \Psi_o)/\mu. \text{ (Equation 3.4a)}$$

Therefore, it is relatively straight forward to compute the amount of material necessary to establish a uniform dose below the surface of a variable contour.
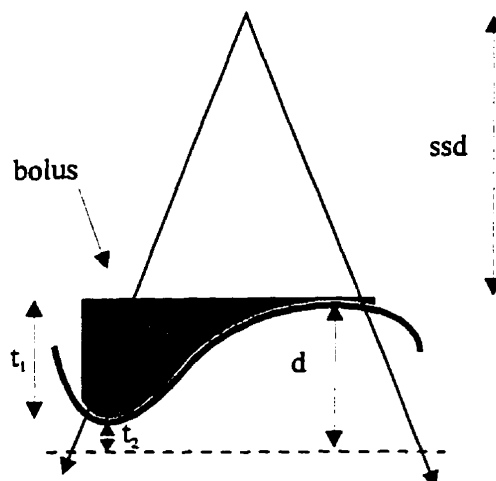
Figure 3.14: A bolus, used to create a uniform dose at some fixed distance below the patient surface.

Since the bolus no longer provides the scatter contribution at depth as it would if it were placed directly above the patient, it is becomes necessary to scale the dimensions of the retracted compensator by an amount referred to as the tissue reduction ratio. Because of the lack of scatter contribution by displacing the bolus, it is necessary to scale the retracted compensator to a smaller vertical dimension. This scaling ensures that the dose is uniform at the specified treatment depth.

The scaling factor, or tissue reduction ratio, is calculated using the method described by Ansbacher et al. (1992). The distance t_1 represents the maximum air gap as observed on the phantom surface and therefore reflects the maximum amount of "lack of scatter" for the retracted compensator. For a given field size, and photon energy, tissue phantom ratios can be used as opposed to fluence data in order to determine the relative amounts of dose received at a specified depth. The thickness reduction ratio is computed through the following equation,

$$trr = \frac{\mu \cdot t_1}{\ln\left(\dfrac{TPR(t_2)}{TPR(d)}\right)}. \text{ (Equation 3.5b)}$$

Thus, the amount of material necessary to compensate the beam at thickness t_1 becomes t_1/trr. A single value of trr is used for the whole field and thus all dimensions of the bolus are scaled by a constant factor.

Another approach for producing a compensator is to use an iterative approach [Mageras et al. 1991, Renner et al. 1989]. In this technique, the plane of uniform dose is defined and an open beam dose distribution is computed. The compensator shape is based on the dose values at the specified depth. Neglecting the penumbra and the heel of the penumbra, a minimal dose value within the beam is found and stored. Assuming exponential attenuation, the approximate amount of material necessary to attenuate the beam to create a uniform dose at the specified depth is computed with Equation 3.4a. We use the dose distribution generated from the open field and use dose as opposed to energy fluence in Equation 3.4a to determine the amount of material necessary. The first iteration can be likened to correcting the primary contribution of dose to the specified plane. For ray lines emanating from the source, an equivalent amount of material is placed by the collimator head using Equation 3.4a.

After the first compensator is constructed, a calculation of the field with the compensator in place is performed. The resulting dose at the specified plane is extracted in order to assess the degree of dose uniformity. After the field is specified, the minimal dose level is found and each point within the field is compared. If the dose at any point within the field plane is greater than some tolerance level, a compensator shape is constructed for that dose point. If the dose at a point within the plane is less than the tolerance from the original minimal dose value, no compensating material is added. If the dose at a point within the specified field is greater or less than 2% of the minimum dose level, a small amount of compensating material is either added to or subtracted from the original compensator. This process is repeated until a uniform dose is achieved throughout the specified field. Mageras et al. (1991) found that normally two iterations are necessary to establish a uniform profile.

3.5 Treatment Verification

The last step involved in radiotherapy delivery is verification of the treatment field. During the course of treatment, positioning errors may occur which may be significant enough to modify dose distributions. The advents of on-line image verification tools, such as Digital Portal Imaging Device, have decreased localization errors in routine patient set-ups [Michalski et al. 1993]. Michalski et al. report that such devices can differentiate between both systematic and random errors in positioning. With respect to lung cancer treatment, Ohara et al. (1987) obtained verification portal films while a phantom had undergone respiratory like conditions. To date, portal verification of lung cancer targets under the influence of respiratory motion has not been reported in the literature.

4. Respiratory Motion

The intent of this chapter is to introduce some basic anatomy and physiology of the chest as well as discussing some of the consequences of respiratory motion in radiotherapy. A detailed anatomic description of the thorax may be found in more suitable anatomy textbooks [Tortora 1992]. This section will focus only on the relevant anatomy encountered in this thesis work. The effects of respiratory motion during CT the image acquisition, clinical consequences, and methods that incorporate respiratory motion in the treatment plan are discussed.

4.1 Anatomy of the Thorax

The lungs play an essential role in the respiratory system by providing the gas-blood interface through which oxygen diffuses. Gases pass through the mouth, down the trachea and the primary bronchus. The primary bronchus then divides into secondary bronchi, which separate the lung lobes. For the left lung, two secondary bronchi aerate the superior and inferior lobes. For the right lung, three secondary bronchi aerate the superior, inferior, and middle lobes. Each lung lobe is separated by fissures. The passageways divide into smaller and smaller branches: from the secondary bronchi, tertiary bronchi, bronchioles and eventually to terminal bronchioles. These passageways consist mainly of cartilage and smooth muscle, and their inner surfaces are lined with a mucous membrane. As the branches become smaller, the content of cartilage decreases while the content of smooth muscle increases.
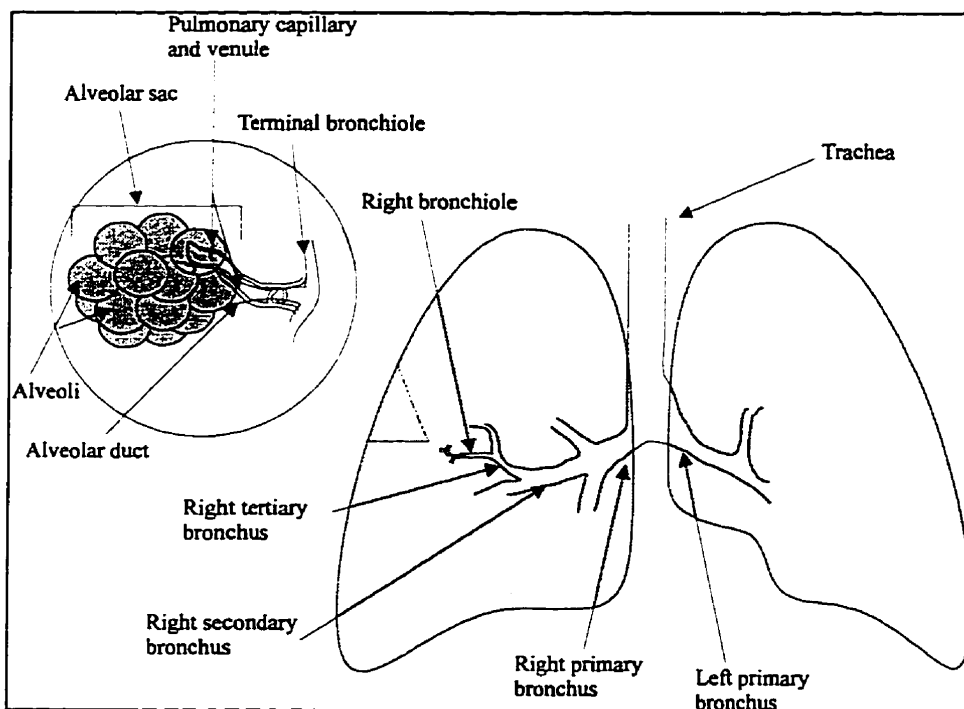
Figure 4.1: A normal lung anatomy. The heart normally sits left of centre, underneath the bifurcation of the left and right bronchi.

Connected to the terminal bronchiole are the respiratory bronchioles. Respiratory bronchioles divide further into the alveolar ducts. Surrounding the alveolar ducts are alveoli within the alveolar sacs. Alveoli are semicircular pouches that provide the gas-blood interface for respiration. If several alveoli are connected to the duct, the connecting unit is called the alveolar sac. In a normal lung, there are about 30 million alveoli, constituting a surface area of about 70 m^2 for gas exchange.

Alveoli are surrounded by arteries that carry both oxygenated and deoxygenated blood to and from the heart. The gases exchange through the alveolar-capillary membrane, typically 0.5 mm thick, through diffusion. At the interface, the waste carbon dioxide (CO_2) gases go from high pressure (inside the capillaries) to low pressure (beyond the interface). For oxygen (O_2), the process is reverse; O_2 exists outside the interface at high pressures that allows for O_2 diffusion, oxygenating the blood. The pressure variances within the alveolar sac are created by muscular contractions of the thorax.

Surrounding the lungs are the ribs and the rib cage. The ribs have muscles that connect in the superior-inferior direction, along the dorso-ventral and transverse sides of the rib cage. These muscles are known as intercostal, or accessory, muscles. Underneath the anterior and inferior portion of the rib cage lies the major tendon of the diaphragm. The diaphragm is a dome shaped muscle that lays inferior to the lungs and separates the thoracic and abdominal cavities. This flat and sheet-like muscle anchors itself along the perimeter of the abdominal cavity, inferior to the rib cage.

The lungs are lined with a thin sac of water called the pleural cavity underneath the rib cage muscles. This thin membrane couples the lung tissue (parenchyma) and the respiratory muscles that surround it.

4.2 Physiology and Mechanics of Respiration

The respiratory system consists of two parts: the gas exchange organs and the pumping mechanisms. The gas exchange organs consist of the lung, bronchi, and other organs that provide the passageways for gases. The pumping mechanisms consist of structures such as the rib cage, diaphragm, abdomen, along with other mechanisms that regulate the flow of gases. Generally, the analysis of muscle motion may be defined through three variables: force, length, and velocity. In terms of lung mechanics, the pressure is related to force exerted by the muscle, the volume is related to the length of a muscle, and the change in volume per time is related to the velocity of muscular contraction. There exist many models that describe the various pressures, forces and volume changes within the thorax. Many of these models describe the variations through a differential equation, similar to a LRC circuit [Primiano 1982, Pengelly 1979, Derenne et al. 1978]. Some models involve the use of computers and discrete analysis [Martonen et al. 1995, Fung et al. 1986, Vogel et al. 1976, Vawter et al. 1975].

Studies suggest that healthy lung parenchyma can be assumed to be homogeneous and isotropic [Tai et al. 1981]. In addition, there appears to be a roughly exponential relationship between stress and strain for the lung parenchyma, thereby behaving pseudoelastically [Wilson 1982]. We assume, as a first approximation, that the lung behaves pseudoelastically; thus for small displacements, the behaviour of the lung may be likened to that of an elastic membrane.

Describing the behaviour of tumours within this framework would be relatively straightforward were it not for the fact that unhealthy lungs are not isotropic and homogeneous.

Diseased lung tissues generally exhibit densitometric differences from the normal lung parenchyma [Genereux 1985]. In addition, asynchronous motion of the rib cage and diaphragm has been observed for patients with asthma [Nochomovitz et al. 1986]. Many lung cancer patients have additional respiratory complications such as asthma. Therefore, describing the exact behavior lung motion for lung cancer patients is a formidable task.

4.2.1 The Diaphragm

During tidal, or normal, breathing the diaphragm is responsible for approximately 70% of the total volume change while in the supine position [Campbell et al. 1970]. The muscular contraction of the diaphragm pulls the central tendon inferiorly, causing the height of the dome to decrease (see Figure 5.2). A change in height of the diaphragm creates the change in thoracic volume and, therefore, a change in lung pressure. This change in pressure allows for gases to be inhaled and exhaled. A reasonable approximation is that the pressure the diaphragm cavity exerts on the lung cavity is inversely proportional to the radius of curvature of the diaphragm itself [Whitelaw et al. 1983]. Assuming a constant diaphragm tension, a decrease in the radius of curvature of the diaphragm creates an increase in pressure of the diaphragm surface. The pressure is directed normal and inferior to the diaphragm surface. The pressure above the surface becomes negative and, thus, creates a low pressure area. This allows O_2 to diffuse through the blood-gas barrier and oxygenate the blood cells. Figure 4.2 shows the diaphragm contracting (inhaling) and flaccid (exhaling).
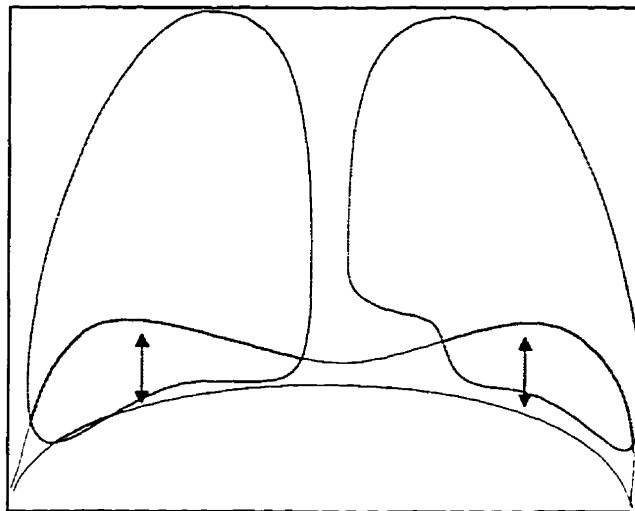
Figure 4.2: Various shapes of the diaphragm. The two lines below the lung show the shape of the diaphragm during inhalation (inferior) and exhalation (superior).

During exhalation, the diaphragm membrane becomes flaccid. Increased abdominal pressures cause an increase in pressure below the membrane. This causes the diaphragmatic radii to increase; that is, both the length and width of the diaphragm increase. For constant diaphragmatic tension, the pressure superior to the dome increases. This pressure pushes the gases out of the lungs. Some typical diaphragmatic displacements are given in Table 4.1.

Reference	Quiet Breathing (mm)	Deep Breathing (mm)
Davies et al. 1994	12 (7)	43 (10)
Weiss et al. 1994	13 (5)	-
Korin et al. 1992	13	39
Wade 1954	17.4 (2.5)	100.8 (19.0)

Table 4.1: Data of diaphragmatic displacements for anteroposterior projections of the diaphragmatic dome. The numbers in brackets are the standard errors.

The above data are measurements of diaphragmatic displacements for healthy subjects. There are no appreciable displacements greater than 2 mm in the lateral direction for the diaphragm during normal tidal breathing for normal subjects. Movements are primarily observed in the superior-inferior direction [Davies et al. 1994, Campbell et al. 1970]. Campbell et al. report that there appears to be no appreciable difference in displacements for males and females.

4.2.2 The Rib Cage (Intercostal) Muscles

These muscles elevate the ribs during inhalation and pull the ribs closer together during forced exhalation. During inhalation, the lateral and anterior-posterior diameters of the rib cage increase, thereby creating a larger volume and lower pressure in the rib cage. The low pressure within the thorax allows O_2 to enter into the lungs. The opposite is true during exhalation, where the smaller volume creates a higher pressure inside the lungs, pushing out the gases contained in the thorax.

Through a vector analysis, it has been shown that the ribs rotate with respect to a fixed axis located by the neck [Wilson et al. 1987]. The motion of the rib cage may be defined as "pump" or "bucket" handle motions. Shown in Figure 4.3 is a diagram of these possible motions.
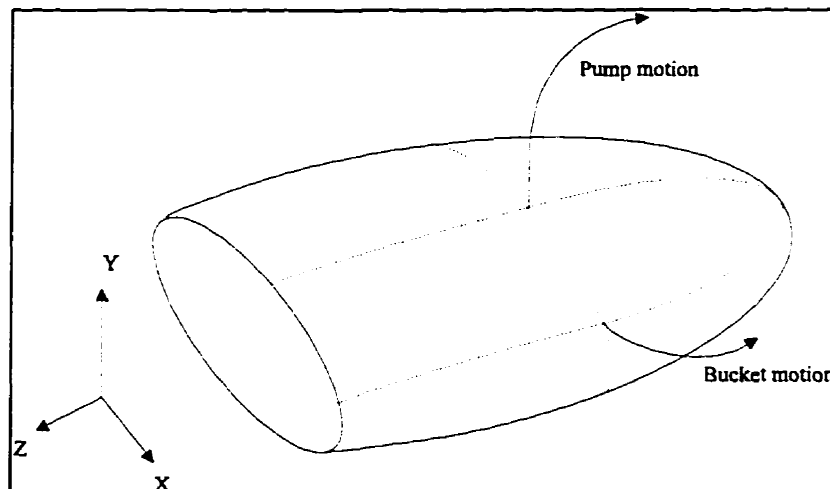
Figure 4.3: Bucket and pump motion of the rib cage.

The motion in the sagittal-transverse direction is described as pump motion and the motion in the transverse-vertical direction is described as the bucket motion. The pump motion may be defined as the rotation about the X axis and the bucket motion as the rotation about the Y axis. For most practical purposes, the change in rib cage shape may be approximated by changes in lateral and dorso-ventral diameters assuming an elliptical thoracic cross section [Campbell et al. 1970].

4.2.3 The Abdominal Muscles

The abdominal muscles line the dorsal part of the abdominal cavity and contribute to respiration, mobilisation, and stabilisation. A reasonable approximation when modeling abdominal and diaphragmatic pressures is that the abdominal cavity consists of an incompressible fluid: this implies hydrostatic equilibrium at the abdominal and diaphragmatic surfaces. Of all the respiratory muscles, the abdominal muscles and diaphragm contribute the most to the respiratory process while in the supine position. The diaphragm and abdomen both remain flaccid, as either the abdomen or diaphragm instigates exhalation or inspiration.

4.3 Effects of Motion in Lung Cancer Treatment

A volumetric change of the thorax due to respiration may modify the dose delivered to a target by an external photon beam in two ways. First, there may be fluctuations in lung density during respiration that could result in a change in the photon interactions, thereby changing the deposited dose. Second, muscular contractions may cause the target and other relevant anatomical structures to move within, and possibly outside the treatment field.

Ross et al. (1990) imaged patients with various thoracic complications while freely breathing. The total acquisition time for each image was approximately 0.7 seconds for a 8 cm axial section of the patient. Because of the long scanning times, displacements in the anteroposterior direction were not possible to measure. It was found that for tumours situated in the mediastinum, displacements are greater in the lateral direction than in the anteroposterior direction. Lateral displacements by the vicinity of the aorta or heart averaged displacements of 9 mm. They also found little motion of the target in the upper lung. All displacements in the lateral direction were closely tied to cardiac motion.

Given the high frequency of cardiac motion and its high velocity of motion, it may be neither beneficial nor practical to minimise this margin by gating the radiotherapy beam to the pulses of the heart. Through the use of an ultrafast CT scanner, Ritchie et al. (1992) measured the healthy heart to move at a velocity of 52.5 mm/s. From this information, it was determined that a CT scan that did not exhibit any motion artifacts would have to be obtained in 19.1 ms. Existing technologies does not allow for scanning at these speeds unless the image is gated to the cardiac cycle. It is unlikely that clinics will adopt cardiac gating for their CT scans until the technologies become commercially available. In addition, it is unlikely that treatment plans can avoid PTV margins required for cardiac motions, unless it can be contiguously defined on the CT images. For this reason, the effects of cardiac motion are not pursued in this thesis.

4.3.1 Respiration: Density Considerations

During respiration, the volume of the thorax varies. Along with the expected shifts in organ position, there is also a change in the overall lung density. Although the density of CO_2 and H_2O are greater than that of O_2, their mass abundance within the lung is very small and thus not very likely to contribute significantly to density variations. If we assume that the mass and density of air within the lung remains constant throughout the respiratory cycle, the mass of the lung will depend on the amount of the lung parenchyma and blood. The effect of pulmonary blood volume changes to CT attenuation is still uncertain, but it is likely that the effect of blood volume change is small [Robinson et al. 1979]. It is more likely that the change in density is due to the change in air volume within the thorax.

Several CT based studies indicate that there is a small but significant change in lung density variation during respiration [Webb et al. 1993, Van Dyk et al. 1982]. The degree of variation is very patient specific; variations may exist not only between different populations, but also within populations themselves. Robinson et al. have shown that, for healthy male subjects, the lung density decreases during exhalation. This fact is accentuated during forced breathing. When comparing forced inhale-exhale CT numbers, differences in attenuation of 173 ± 38 Hounsefeld Units, have been observed. This amounts to approximately a 17% change in electron density relative to water. Van Dyk et al. report maximum changes in relative electron density of 0.28 ± 0.08 for children of the age of 5 and 0.19 ± 0.03 for those of the age of 80.

For such variances in electron density, a reasonable question one may ask is whether they are significant enough to modify the prescription dose. Van Dyk et al. found a correlation between relative electron density and volumetric displacement. A typical volumetric tidal displacement is about 0.4 litres that, when using Van Dyk's data, correlates to about a change in relative electron density of 0.02. To approximate these effects, consider the geometry in Figure 3.3.

If we take the relative electron density of lung and surrounding tissue to be $0.30 \text{ cm}^3/\text{g}$ and $1.00 \text{ cm}^3/\text{g}$ respectively, and $z_1 = 2.0$ cm and $z_2 = 7.0$ cm, for a 10 x 10 field of Co-60 photons, a Batho inhomogeneity correction factor at this relative density produces a result of 1.142. This implies that the dose at point p is 1.142 times greater than if the phantom consisted of water only. If the relative electron density decreases 0.18, we obtain a correction factor of 1.182.

Assuming the Batho correction is accurate, this corresponds to a reduction in dose of about 4%. Although these variations in dose seem to be significant, two important facts were not considered in this approximation: The physical pathlength between states remains constant, and of course, electron density changes due to tidal volumes displacements are not typical.

Webb et al. report that the changes in lung density occur in a relatively homogeneous fashion [Webb et al. 1993]. Also, Van Dyk and Webb report a linear correlation between relative electron density of the lung and volume change. This implies that the effective pathlength remains constant for any point within the lung volume. If that is the case, the primary contributions to dose will not be greatly affected for a fixed volume with a uniform density variation. Thus, one would expect corrections in dose to be much less than 4%. In addition, a more realistic tidal volume displacement of 0.4 litres results in a change in electron density of 0.02. A change of this magnitude would result in a reduction in the correction factor by 0.3%.

In addition, 6 MV photons more commonly used for lung treatments because of its longer effective distance. Lower energy photons have less penetration and thus greater variances in dose in homogeneous to inhomogeneous tissue. Higher photon energies have greater penetrability and the fall-off in dose is not as for photons of lesser energy. The variances in correction factors in homogeneous to inhomogeneous tissue for higher energy photons will not be as large as those calculated for Co-60 photons.

In light of these arguments, it is assumed throughout this thesis work that the changes in dosimetry due to respiration are primarily due to physical displacements as opposed to density variations. Under normal tidal breathing, the density variations within the lung are assumed to be not significant.

4.3.2 Respiration: Displacement Considerations

The primary effects of respiration in a radiation treatment plan are internal and external contours and volume displacements. The implications of such motions need to be assessed at each stage of the planning process.

4.3.2.1 Effects on Diagnosis

For transmission radiographs and diagnostic CT scans, patients normally are told to hold their breath during imaging. Motion artifacts are not a problem for radiographs since the X-ray beam may only be on for milliseconds. For CT images, however, scan times can range from milliseconds to minutes, depending on the image resolution, depth of the scan, and scanner type. Ritchie et al. (1992) found that a minimum scan time of 93.5 msec is necessary to account for respiratory motion. The fastest CT scanners available on the market can acquire scans in 50 msec; however, because of their expense other methods must be used to suppress motion artifacts.

Most common CT scanners are known as Third Generation scanners. These types of scanners consist of a rotating anode opposite to a detector array, both that rapidly spin around the patient. Images are created by performing a filtered back-projection image reconstruction of the transmission data. At the Cross Cancer Institute, CT data can be acquired by two methods: "step and shoot" and helical scanning.

In the step and shoot technique, the couch moves in the superior-inferior direction at intervals that determine the resolution along the z axis. The image acquisition process for a single slice is on the order of milliseconds; however, reconstruction is performed immediately after each data slice acquisition, and therefore each scan may require several seconds. Since respiration periods can range from 2 to 5 seconds, the effects of respiration may create motion artifacts in the image. Patients can hold their breath during the acquisition, but often this is not possible. Many patients are elderly and have respiratory problems; thus, one cannot expect to prolong the image acquisition period longer than several tens of seconds.

Besides speeding up the image acquisition process, the simplest and most effective method to reduce motion artifacts is to gate the CT scanner to the respiratory cycle [Mori et al. 1994, Ritchie et al. 1994]. In addition to gating, the image acquisition time may be reduced through spiral CT scanning. By modifying the conventional Third Generation CT scanner, the imaging sequence can be modified to obtain much faster images. Instead of stepping the couch throughout the image acquisition, one can continuously move the couch in the superior-inferior direction and process the information in the required intervals. The helical data is interpolated to produce information in the same format as the step and shoot method. Since the imaging

beam is on continuously, image processing time is dependent on the heat load characteristics of the anode. Because of this, processing times are unequal, gradually increasing at the latter stages of acquisition. The amount of time to complete the total scan becomes considerably smaller, however, as the total X-ray exposure time increases, the period for each scan also increases. Helical scanning times may range from 5-20 seconds, depending on the resolution required. Because the scanning times are short, helical scanning is normally done for diagnostic scans. During the scan, patients are normally told to hold their breath to reduce motion artifacts; this allows for more accurate clinical diagnosis.

4.3.2.2 Effects on Treatment Planning and Delivery

Contour variations of 1 cm or greater can significantly alter the dose distribution [Hobday et al. 1979]. The variations in dose may be due to geographical displacement of the target and both internal and external contours. The effects of respiratory motion are not simply constrained to movement of the thorax. Abdominal structures may also move significantly from the contractions of the diaphragm. For tumours situated close to the kidney, which is a radiosensitive structure, Schwartz et al. (1994) advocate respiration gated radiotherapy. Average displacements of the kidney were measured at 4 mm. Moreland et al. (1994) measured kidney displacements due to respiration of 2-35 mm for normal breathing, and 10-86 mm for forced breathing. The doses to kidneys for ovarian cancer patients have been found increase due to respiratory motion. Displacements of the liver in nuclear medicine studies have been measured at 14-18 mm in the superior-inferior direction, most likely due to diaphragmatic excursions [Haruaz et al. 1979].

Hobday et al. found contour variations of 1 cm or more for the thorax and the abdomen due to respiration, some of which changed the dose to tumours significantly. Displacements of tumour volumes due to respiration occurred primarily in the superior-inferior direction. These changes in body contours will effect the radiological distance the beam traverses [Jacobs et al. 1996]. In so doing, more, or less dose may be deposited at the target site depending on the position of the target with respect to the beam aperature. The greatest change in radiological distances was found to be in the anteroposterior direction, most likely due to the "pump" handle motion of the rib cage. Jacobs et al. found for a two field AP treatment, if the time average contour of the patient is not used in dose calculation, errors greater that 1% in dose at the centre may occur.

4.3.3 Accounting for Respiration in Lung Cancer Treatment

The most common approach to account for respiratory motion when planning photon therapy is to simply increase the margins irradiated such that a certain fraction of healthy tissue becomes irradiated. Ross et al. (1987) have found that margins of approximately 2.0 cm are necessary to account for motion in the lateral direction. This accounts primarily for cardiac motion since the beating of the heart invokes net lateral displacements of objects within the lung. The extent of lateral field margins will depend greatly on the degree of cardiac and "pump handle" motion exhibited by the patient. Superior-inferior margins will depend on the degree of diaphragmatic displacement. Superior-Inferior margins may be assessed during the fluoroscopic simulation of the treatment plan.

Another approach is to incorporate organ motion into the PTV. Mageras et al. (1996) have recently developed a method that predicts the effect of organ motion in the calculated dose. Several reference CT images are used to determine the likely location of the object and

the volume of interest's contour is modified through each reference scan. Dose volume histograms are obtained for each reference scan and used as a clinical endpoint. Killoran et al. (1997) employ a Monte Carlo methodology to simulate target motion and overall position. A PTV margin is then generated through a gaussian like approximation of the target volume, which accounts for systematic and random motion. Potential dose volume histograms for the likely positions of the volume of interest are generated as an endpoint. Healthy tissue will be included in the PTV generated through this method.

There are two things that may be done to spare PTV margins allotted for respiratory motion; one can gate the radiation beam to the respiratory cycle [Kubo et al. 1996, Ohara et al. 1989], or the patient can be asked to hold their breath while the beam is on [Huang et al. 1996]. Ohara et al. (1989) found that a stable and reproducible position of the target was achievable during the end-expiratory phase of quiet respiration. Kubo et al. (1996) have found that a strain gauge wrapped around the patient's torso provides an inexpensive and efficient tool that can produce a desirable signal that can be correlated to target displacements. The digitised signal from the strain gauge can be temporally correlated to target displacements as observed on fluoroscopy. In such a setup, it would be necessary to attach the strain gauge (or other measuring device) from the patient to the treatment machine during the treatment.

Regardless of method employed, care must be taken to ensure that the delivered plan can be adequately modeled. In order to do this accurately, the CT data used to calculate the dose must be reflective of the patient's treatment configuration. The inaccurate assessment of the volumes will have further implications not only to the dose calculation, but also the subsequent calculations during the planning evaluation. Baltar et al. (1996) investigated the uncertainties in CT based radiation treatment planning specifically addressing patient breathing. Their studies have shown that free breathing CT data acquisition may improperly estimate both the volume and position of objects. In addition, subsequent calculations of dose-volume histograms and normal tissue complication probabilities may also be in error. For the lung, up to an 18% variance in complication probabilities has been observed when comparing inhale to exhale CT data.

5. Treatment Planning Optimisation

The purpose of this chapter is to present the findings of a portion of the thesis work. In this chapter, a method of obtaining a high and uniform dose to an arbirtrary tumour volume is presented. The method address internal and external inhomogeneities and has the ability to handle complicated three dimensional geometries in a straight-forward manner. Section 5.1 discusses some work that was done prior to the thesis, whose results are relevant in the thesis work.

5.1 Dose Optimisation: Internal Inhomogeneity Compensation

As briefly mentioned in Section 3.2.3, there are many methods of achieving high and uniform dose to planning target volumes. Feasible and clinically deliverable methods may include both algorithmic minimisation of objective functions and user controlled constraints and tolerances. Regardless of the exact technique used, it is essential that the optimisation routine model inhomogeities accurately. Neglecting lung tissue inhomogeneities in the optimisation may result in higher (5 to 15%) than prescribed doses to targets [Morrill et al. 1994]. Section 3.2.4 describes a method of dose optimization through selection of certain parameters such as beam weights, collimator, wedge, and gantry angles. Described in this chapter is an optimisation approach that establishes high and uniform dose to the target area through the use of compensators and the gradient vector approach.

Before we can address the issue of multiple beams in a treatment plan, the effects of inhomogeneities are first addressed for individual beams. A great deal of effort is made in ensuring that dose distributions are flat in homogeneous phantoms such that the isodoses are perpendicular to the beam's central axis. The existence internal inhomogenieties may modify the distribution significantly such that the distribution is not flat and heavily dependent on the amount of contour variations and internal inhomogeneities. Described below are methods to correct for internal inhomogeneities so as to achieve a flat distribution at a desired depth.

5.1.1 TRR Method for Internal Inhomogeneity Compensation.

Two experiments were performed to test whether internal inhomogeneities could be compensated. Two phantoms were constructed that mimicked internal inhomogeneities in a water tank. The first phantom consisted of a cylindrical air cavity immersed in a water tank (see Figure 5.1). A second experiment was conducted to test the compensation technique with more realistic densities and contours. A lung phantom with an irregular geometry was constructed and placed in a water tank (see Figure 5.2). The measured data was then compared to ATP's inhomogeneity algorithms to test its reliability. The configurations consisted of 2D geometries that could be modeled in the treatment planning software.

5.1.2 Methods and Materials

The air cavity casing was constructed out of polystyrene that has a density of 1.06 g/cm^3. The thickness of the polystyrene casing was 0.32 cm. The inner radius of the air cavity was 4.13 cm. The relative electron density of the polystyrene is 3.238 x 10^{23} electrons per gram, which is approximately 3% less than that of water. We assume that in these energy ranges, Compton interactions dominate and photoelectric effects are small. In addition, the

ratio of mass collisional stopping powers between water and polystyrene, or the amount of energy lost per unit length, is about 1.035 for 6 MV photons. That is, the amount of kinetic energy released in the material through ionisation in water is slightly greater (about 4%) than in polystyrene. Despite this difference, we assume that energy dissipated between the two mediums are relatively the same and that transient charged particle equilibrium is not greatly perturbed for interactions between the water and polystyrene interfaces.

The lung phantom consisted of cork with a density of 0.30 g/cm^3, providing a typical density that one may encounter for a thoracic treatment. The geometric design mimics a more realistic posterior-anterior lung view. The cork was wrapped with a thin amount of plastic wrap in order to ensure that it was dry and not saturated with water. The plastic frames, that held the phantom in place, connected the sides of the phantom to a 30 x 30 cm sheet above the phantom. The frame and sheet also consisted of polystyrene.

For the first phantom, cylindrical symmetry could be exploited to recreate the exact geometric shape of the phantom by the head of the linac. Through simple ray tracing, an analytic expression was derived to determine the thicknesses of air as seen through the beam's eye view. The resolution of the thickness strips at the horizontal plane of the air cavity was 0.28 cm. With the accessory tray at 61.6 cm, the thickness of each compensated ray was 0.16 cm. For the second experiment, the abnormal shape of the inhomogeneity required direct measurements of thicknesses traversed as seen from the beam's eye view. Thickness resolution of the lung phantom's compensator was 0.33 cm.
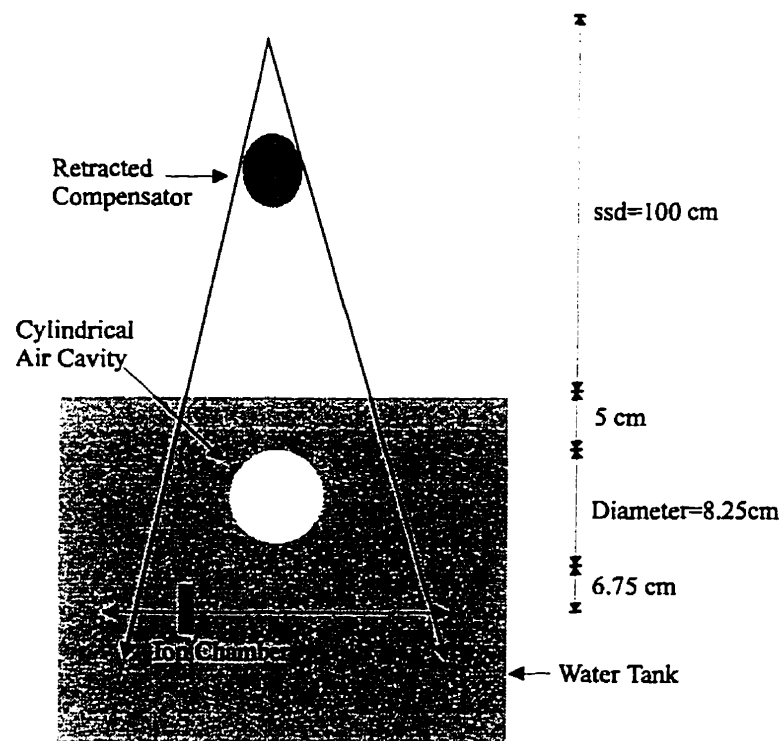
Figure 5.1: Experimental design of first experiment. Field size at correction depth was 30 x 30 cm, for a 6MV linear accelerator.

To correct for lack of scatter at the correction depths, each ray was scaled by a single thickness reduction ratio using Equation 3.4a. In the case of the cylindrical phantom, the calculation was straight forward; t_1 and d were 8.25 and 20.0 cm, respectively, and values of TPR could easily be looked up to compute the trr ratio. The trr ratio for the first phantom was 1.24. For the second phantom, the lung phantom was decomposed into its water and air equivalents by finding the equivalent radiological distances of the lung phantom.

For the largest extent of the lung (10 cm), it was assumed that 7 cm of the phantom could be described of consisting completely of air and 3 cm consists of water. The placement of the water equivalent material was arbitrarily placed at the bottom of the lung cavity, thus making t_1 and d equal to 15.0 and 22.0 cm, respectively. The trr for the lung phantom was computed as 1.31. All scaling was done in 2 dimensions; that is, the corrections were performed assuming that a uniform 1D profile could be established beneath the inhomogeneity. No corrections nor measurements were made in the patient Z axis (as defined in Figure 3.6).
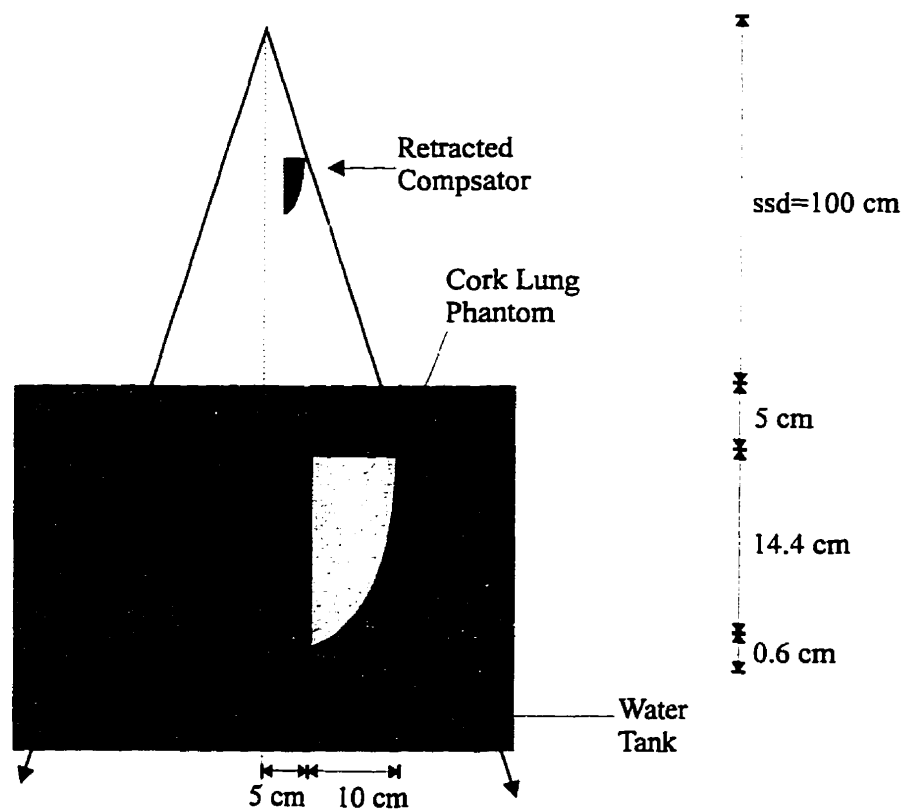

Figure 5.2: Experimental design of second experiment. Field size at correction depth was 30 x 30 cm, for a 6 MV linear accelerator.

A *Welhoëfer*[3] three dimensional scanner was used to scan an ion chamber dosimeter at 0.1 mm intervals underneath the inhomogeneity with and without the compensator in place. An open field measurement of a 10 x 10 cm field and a 30 x 30 cm field for future comparison with the ATP algorithm (see Figure 2.4 for depth dose for the 30 x 30 cm field). When the inhomogeneities were put in place, water was pumped out to ensure that the source to surface distance remained 100 cm. The amount of measurable data was limited to profiles below the inhomogeneities.

ATP's inhomogeneity algorithms include Batho and ETAR routines (See Section 3.2.2). Measured data was compared to the Batho algorithm with and without the compensator in place. Dose resolution of the matrix was dependent on the field sizes; in this case the dose resolution was 0.6 cm for both computations.

5.1.2 Results and Discussions

For the first phantom, measured data with and without the compensators in place are shown in Figure 5.3. Shown in Figure 5.4 are the dose profiles with and without the compensators at the correction depth. Figures 5.5 and 5.6 show the same distributions for the second phantom. Without the compensators in place, significant amounts of dose are deposited due to the inhomogeneity. For the first phantom, approximately 32% more dose is deposited at the central axis than if the inhomogeneity was removed. With the compensator in place, the relative amount of dose is reduced by 28%. For the second phantom, the maximum deviation of dose from an open distribution with and without the compensator is 39% and 5%, respectively. Both compensators show improved homogeneity of dose at the target depths. The isodose profiles generally show improved uniformity at the correction depth. This improved uniformity does not come without the increase in surface dose adjacent and upstream from the phantom and build up of dose beneath the inhomogeneity further downstream.

The TRR method over corrects the amount of material required, except in areas beneath the periphery of the phantom. Even if transient charged particle were maintained by using large inhomogeneities, there would still be an under correction using this method. This is because this method does not account for the scatter contributions adequately for the internal inhomogeneity. The scatter dose at a point beneath an inhomogeneity will be greater than if the inhomogeneity existed on the surface. This is due to the fact that scatter contributions become greater with depth. Thus, if a correction is made that assumes the inhomogeneity lays on the surface, the TRR value will be in error.

Another important factor is the rebuilding of dose that occurs within the two cavities. As illustrated in the open dose profile, dose builds up at a surface due to contaminant electrons from the air as they penetrate the water. For the first phantom, this is not so much the case since the second air-water distance was much greater than 2 cm and transient charged particle equilibrium is most likely re-established. However, this is not the case for the second phantom since the correction depth is much less than 1 cm. It has been shown that electron ranges for interactions within lung phantoms may extend well beyond 10 cm [Mackie et al. 1984].

---

3 Welhoëfer Dosimetrie, Germany

Figure 5.3: Isodose profiles for the first phantom

— With Compensator
— — Without Compensator
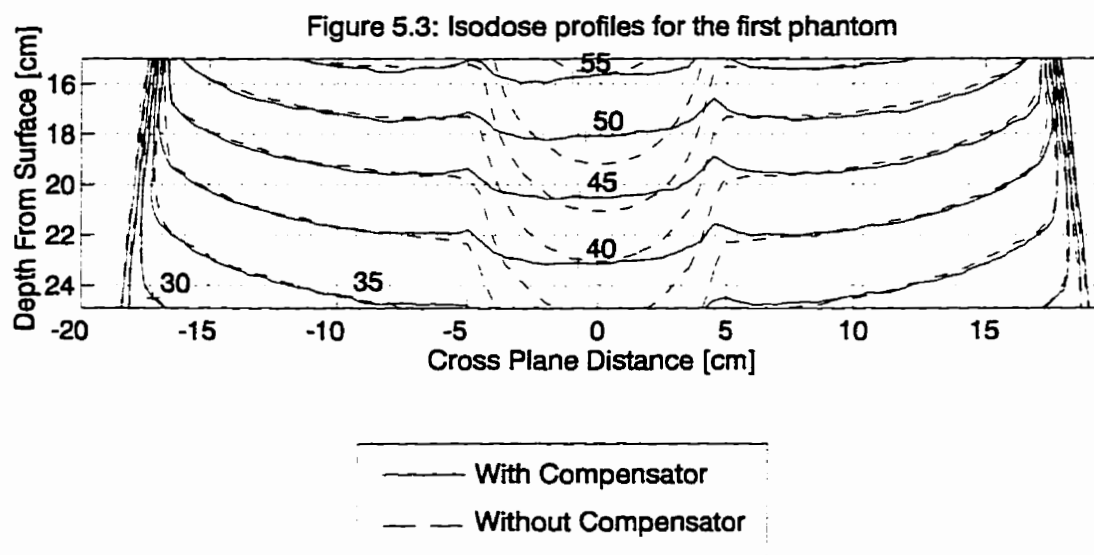
Figure 5.4: Dose profiles for the first phantom at the
correction depth (20 cm).
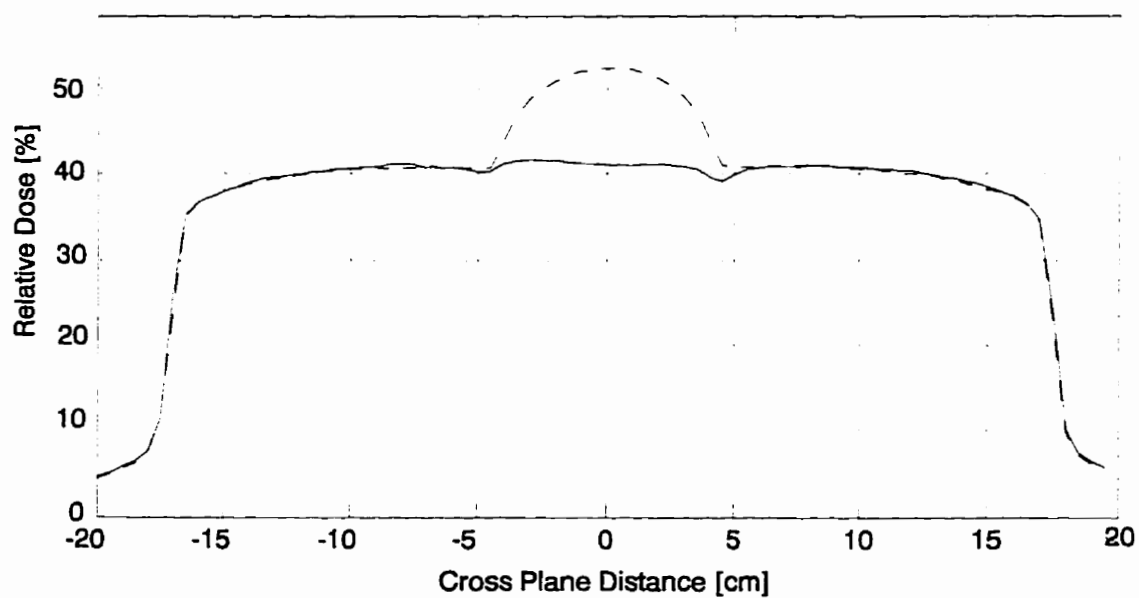
Figure 5.5: Isodose profiles for the second phantom.

With Compensator

— — Without Compensator

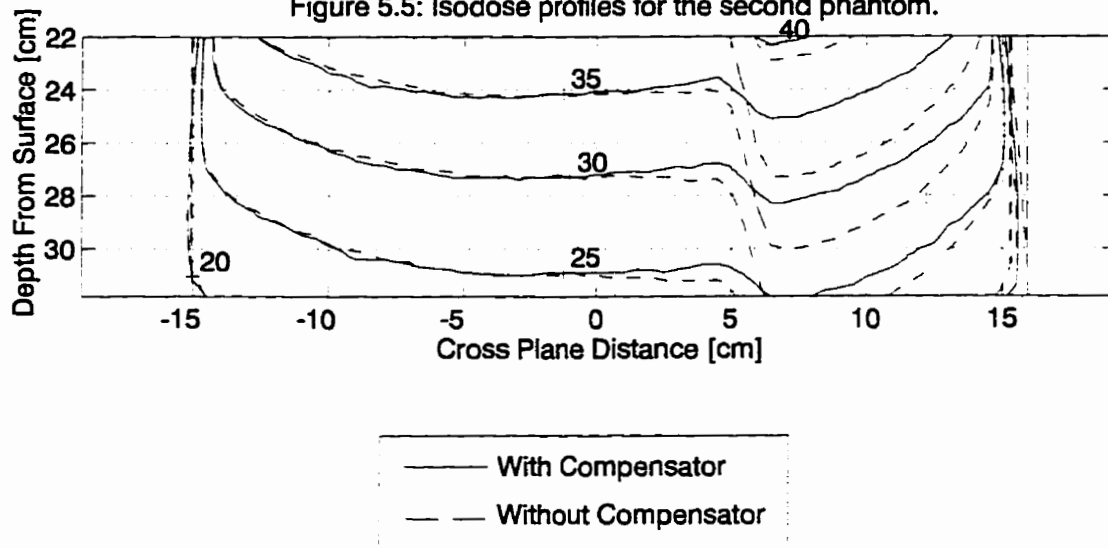Figure 5.6: Dose profiles for the second phantom at
the correction depth(22 cm).
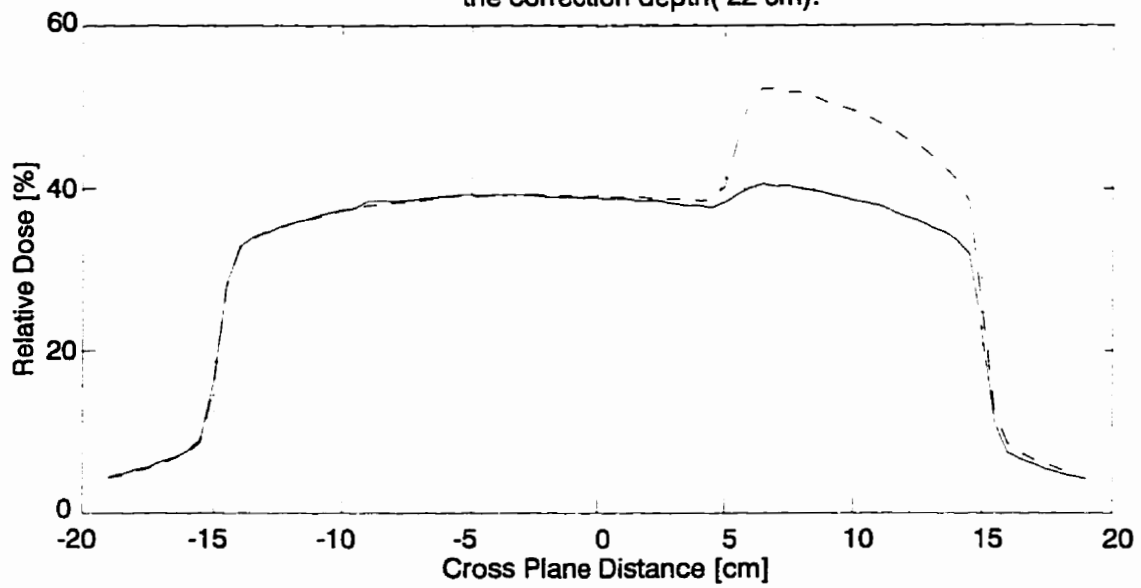
Figure 5.7: Isodose profiles for the first phantom without compensator.
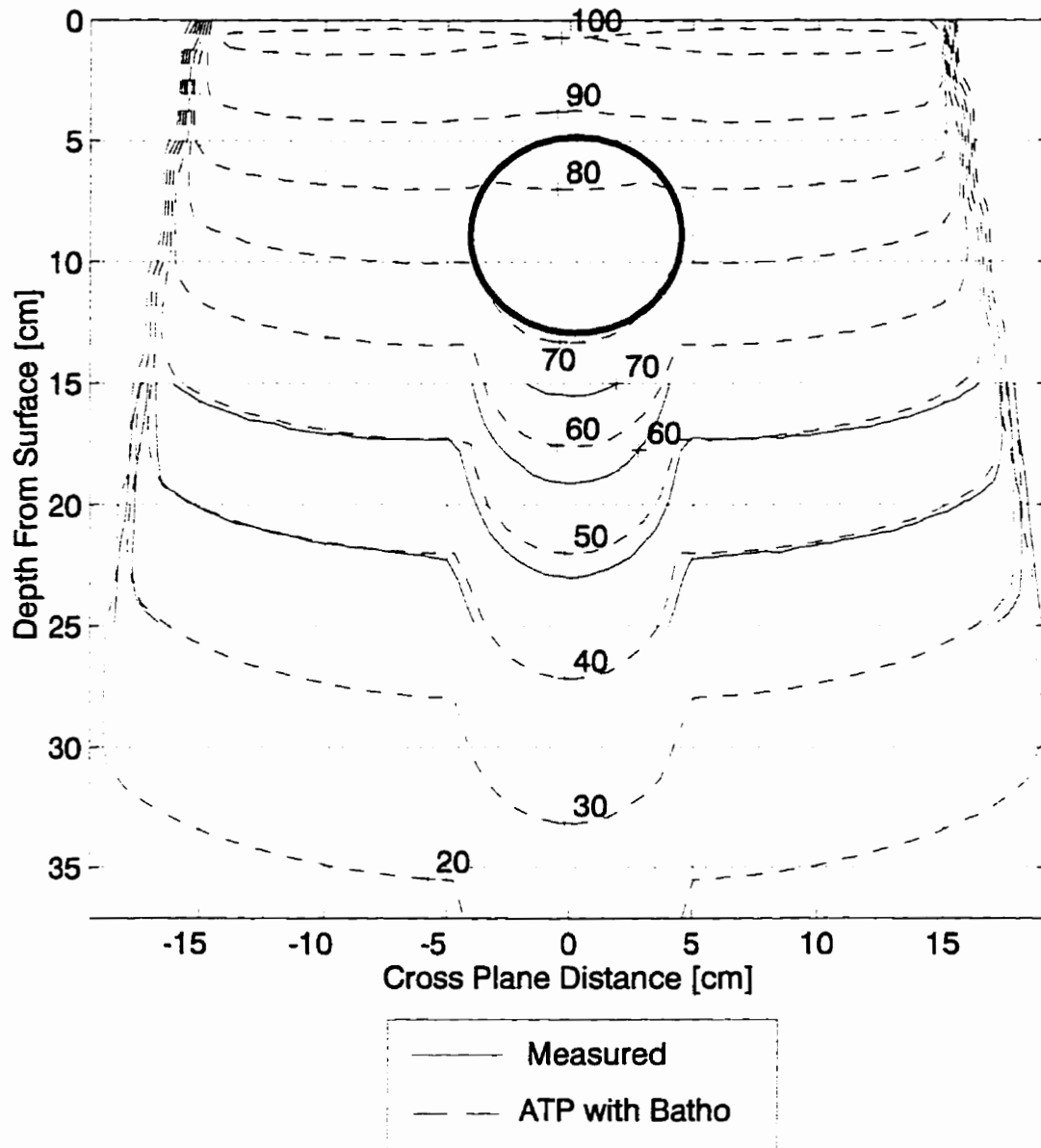
Figure 5.8: Isodose profiles for the first phantom with compensator.
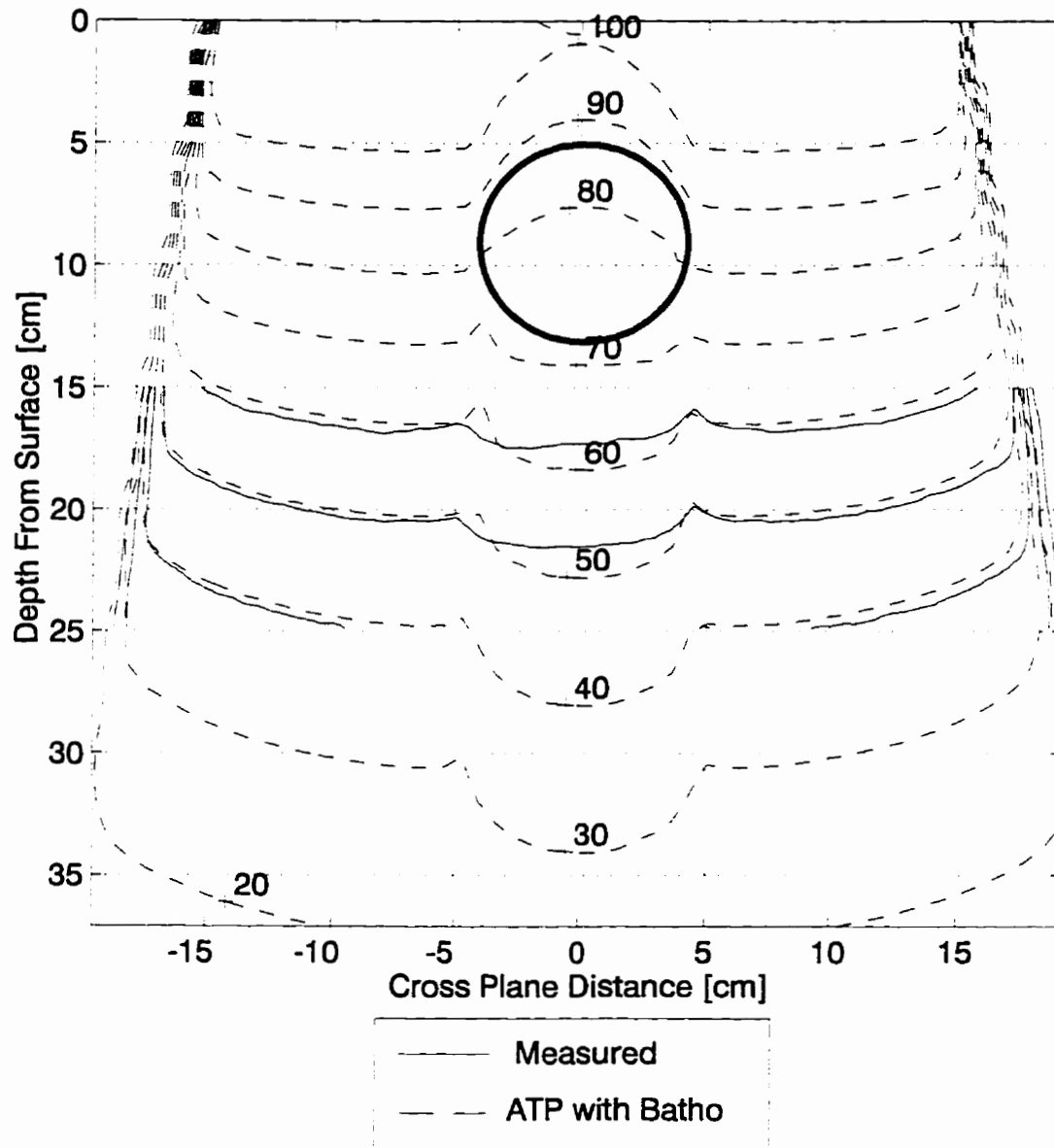
Figure 5.9: Isodose profiles for the second phantom without compensator.

Measured

— — ATP with Batho
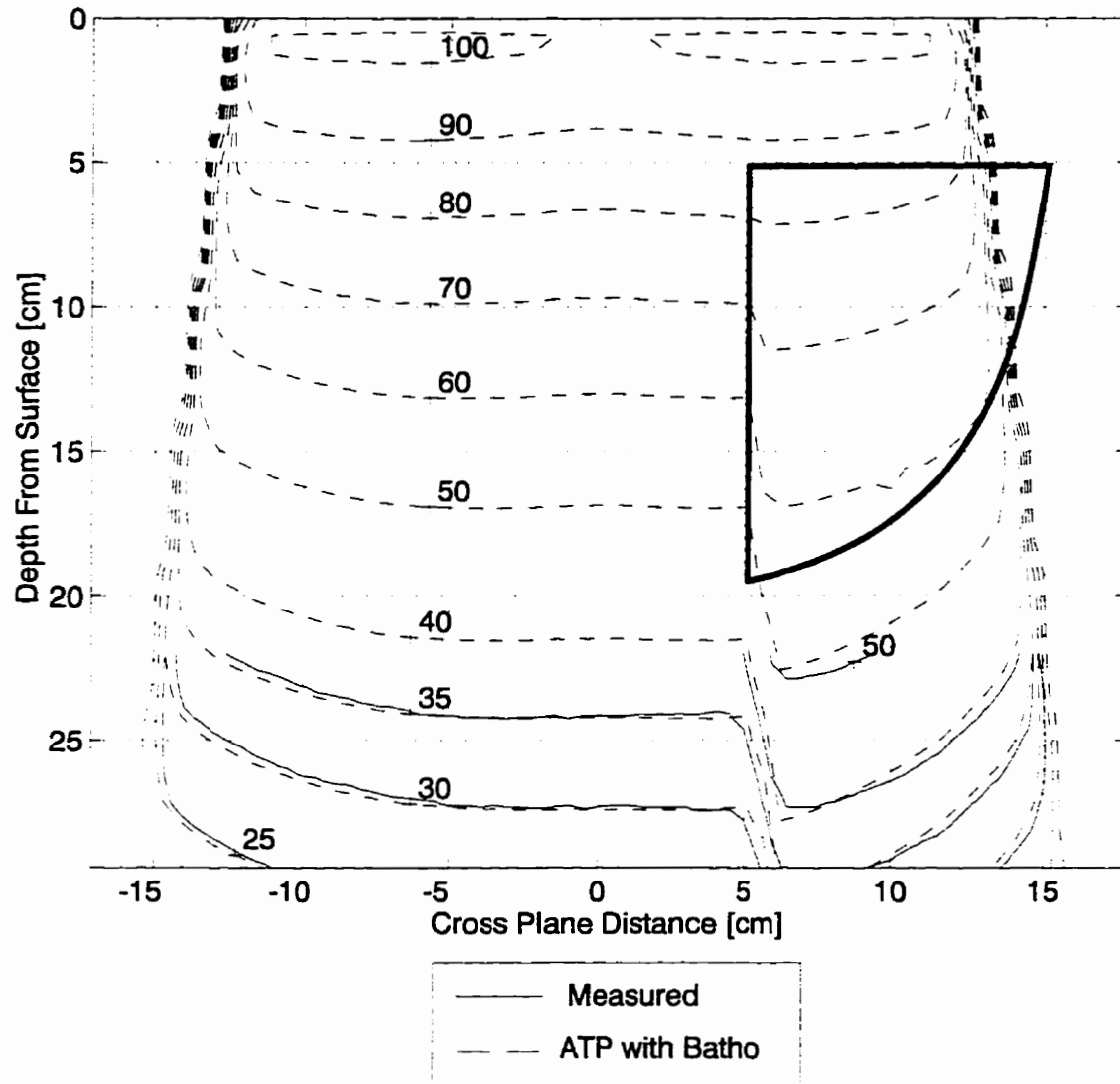
Figure 5.10: Isodose profiles for second phantom with compensator.
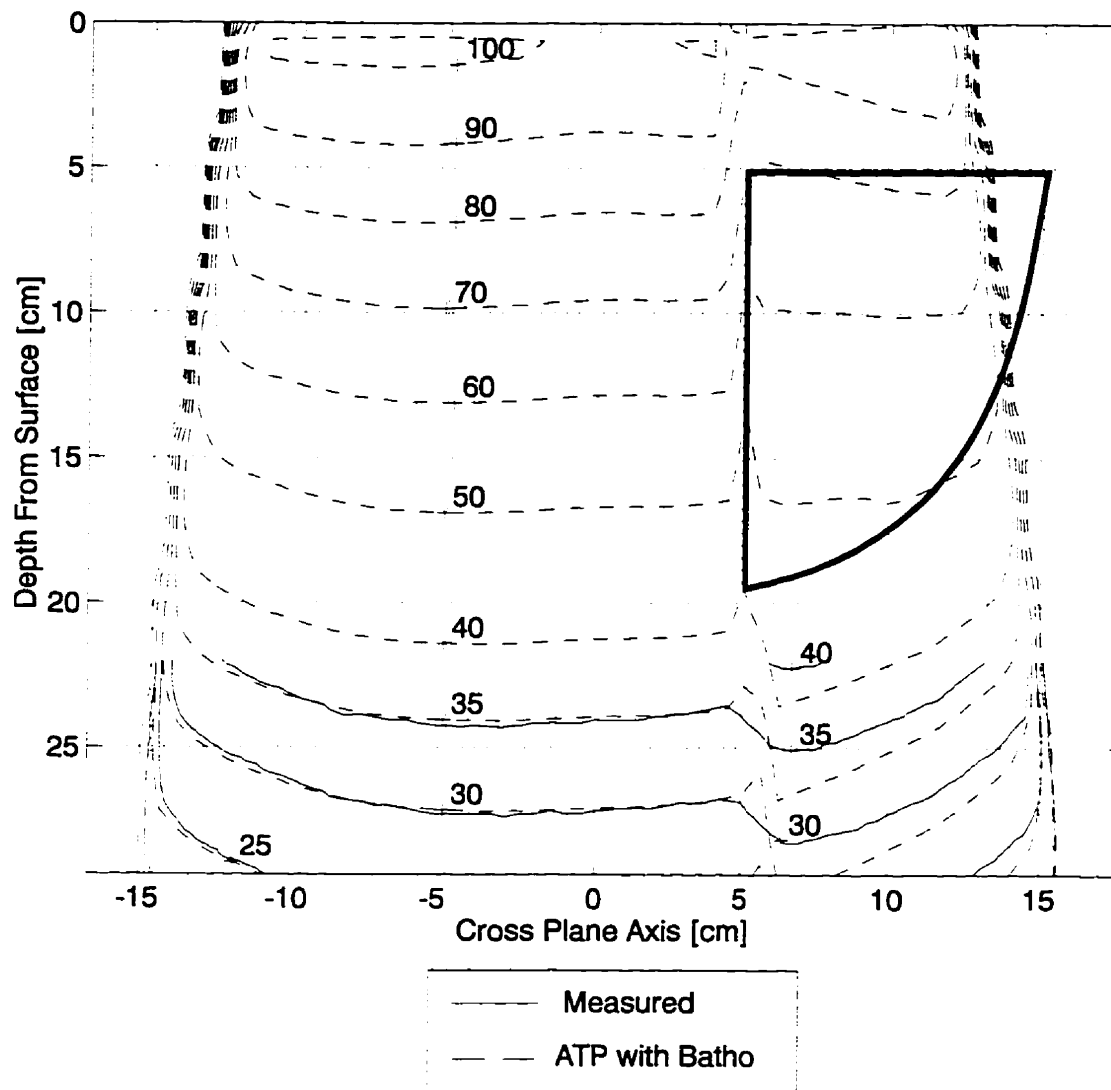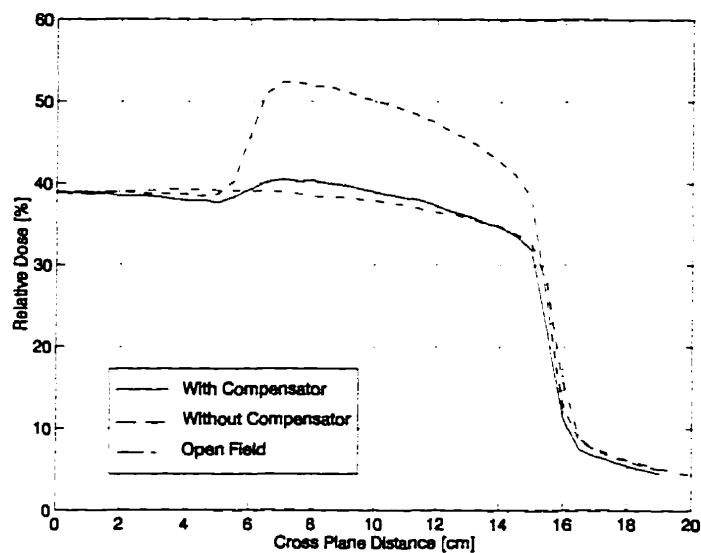
Figure 5.11: Dose profiles for second phantom from central axis.

In Figures 5.7 and 5.8, uncompensated and compensated profiles of the first phantom are compared to the ATP Batho inhomogeneity algorithm. The same is done for the second phantom on Figures 5.9 and 5.10. The doses were normalised to a point off axis for both phantoms. This was done to ensure that normalisation point was not perturbed by the inhomogeneity. There is good agreement between the measured data and the Batho algorithm despite the fact that it consistently underestimates the dose beneath the inhomogeneity. The average discrepancy between the Batho algorithm and measured data at the correction depth with the compensator in place is approximately 3%. The maximum error observed between the algorithm and measured data is 5%. Figure 5.11 shows the efficacy of the compensator when comparing to an open beam profile at the target depth.

It is interesting to note the way the Batho algorithm behaves for vertical interfaces of the phantoms. There is a sharp discontinuity in calculated dose in the "shadow" of the sharp lung boundary. Although the measured dose distribution beneath the boundary is relatively continuous, the Batho algorithm predicts a sharp under and over dosage. This is primarily due to alignment errors from modelling the compensator by the portal head. Figure 5.10 displays the fact that the sharp discontinuity stems from the difference in the primary dose contributions between the two media. The discontinuity in the shadow can amplify the dose discontinuities if there are alignment errors of the compensator at the portal head. Minor displacements can amplify this sharp discontinuity; therefore precautions should be made that the compensator is aligned accurately.

There are two main conclusions from these experiments. First, the wax retraction technique used in producing the compensators proves to be an efficient method to create a uniform dose distribution at depth. Internal inhomogeneities were adequately compensated to within 2-3% using this method.

The second conclusion was that the inhomogeneity correction algorithm, ATP, agrees well with measured results. The largest error observed while using the Batho inhomogeneity correction algorithm was 5%. The average error observed for the Batho correction on ATP

was 3%. This result compares well with published results [Kappas et al. 1995, Wong et al. 1990]. It is likely that these errors stem primarily from the calculation algorithm itself. As mentioned earlier, the Batho correction algorithm does not account for build up regions such as those found at interfaces. This may be of relevance in these experiments since measurements were taken very close to the phantom inhomogeneities. The undercorrection of dose, which is apparent in our results, is in agreement with other published results.

5.2 Iterative Techniques for Internal and External Inhomogeneity Compensation

In most clinical settings, establishing a uniform profile at depth would require knowledge of both the surface contour and the geometry of the internal heterogeneity. The experiments conducted in the last section had no such surface contour variations. As explained in Section 3.4.2.3, another technique to establish a uniform profile at depth is to use an iterative technique [Mageras et al. 1991]. In this method, individually accounting for internal and external inhomogeneities is completely circumvented by simply examining the relative doses delivered at the plane of compensation. The iteration method's efficacy is greatly determined by the accuracy of the dose calculation algorithm. If the dose is computed incorrectly, the compensator shape will be in error. The algorithm must be able to handle inhomogeneity calculations, contour corrections, scatter corrections, and beam modulation devices all within reasonable error.

In Section 5.1.1 it was found that all the ATP Batho algorithm is sufficiently capable of handling internal inhomogeneities to well within 5% error. It was demonstrated in the last section that the Batho algorithm consistently underestimates the dose with the compensator in place by about 3% for depths equal to or greater than 20 cm. If the ATP Batho algorithm was used in constructing an internal inhomogeneity compensator, we can expect the resulting compensator to overcompensate by about 3% when comparing measured and calculated distributions. The compensators constructed through the trr method consistently show about a 2% undercompensation; that is the dose is greater than the optimal value by 2%. Therefore, we can expect the compensator thicknesses constructed through the iterative method to be greater than those generated though the trr method. The additional material should bring the dose lower and closer to the optimal value.

5.2.1 Methods and Materials

An algorithm was created in the MATLAB[4] programming environment to derive compensator shapes from the ATP generated dose distributions. Batho corrected dose distributions were generated in the ATP enviornment with compensators through the Matlab algorithm. The algorithm works external from the ATP dose calculation algorithm, so it may be used in other dose calculation algorithms. The compensator shape is limited to 2 dimensions because ATP computes dose in 2 dimensions only. The algorithm is "user friendly"; it prompts the user for relevant information regarding the desired depth of uniform dose, width of compensation of that plane, geometrical set-up (SSD or SAD), and height of the accessory tray that holds the compensator.

4: MATLAB, Mathworks Inc., Nattix MS

To implement the method, an open field calculation is performed and the dose matrix is stored. Before storing, a problem often encountered is the normalisation. Dose is often given in percentage with respect to a point as opposed to the dose unit of Gray. In the iterative method, material is added or subtracted based on the relative dose values at the target depth. A problem arises as to what point should the relative dose value refer to. If the normalisation is chosen arbitrarily, the compensating material may under or over correct the desired plane of uniform dose. This is because the normalisation will accentuate differences at the depth correction depth more so than if a point further upstream was used. Also, since no measurements of dose are done during the construction of the compensator, it is necessary that the dose at the normalisation point compares well with both measured and simulated data. If the dose at the normalised point compares well, the relative distributions of the measured and simulated data will also be similar. Therefore, in order to circumvent potential normalisation problems, a point is chosen within the field that compares well with measured data, such as a point 2 cm below the surface of the phantom.

The normalised distribution is then exported to a PC and some minor data formatting is done. The dose distribution is then read into a subroutine and the user is prompted for necessary information. The dose distribution is displayed along with the dose profile at the desired depth and relative error with respect to the minimum dose in the field of compensation. The error of the dose profile is computed with respect to the desired dose value, which for the first iteration is the minimum value. The error can be chosen to be arbitrarily small. Using a 2% error has proven to show relatively fast convergence to dose uniformity within about 2 iterations. Compensator thicknesses are then constructed using Equation 3.3a, where percentage dose is used as opposed to fluence to estimate the required thickness. The compensator geometry is then geometrically modified to account for beam divergence.

For a default, the resolution of the compensator is equal to the equivalent distance at the tray height. There is no appreciable difference in the resultant profiles if the resolution of the compensator is changed while keeping the dose matrix resolution fixed. However, there is an appreciable difference if the dose resolution is changed. Such a change not only affects the compensator thickness but also the calculation accuracy. Since it is essential to have accurate dose calculation in this iterative technique, the dose resolution is always chosen to be as small as possible. This ensures that the dose profiles remains smooth functions of position, which allows for a more accurate determination of the compensator thicknesses required. Dose resolutions on the order of 0.65 cm or less proved to be adequate in produce an effective modulation of the beam intensity.

In order to ensure that penumbral effects are not accentuated with the placement of the compensator, material is added to both sides of the compensator that extend beyond the penumbra of the field. Thus, all points within the plane of compensation become attenuated.

For illustration, Figure 5.13a-d shows the outputs of one iteration for the lung phantom used in the previous experiments. The starred point plots in the open dose profile indicate the points of compensation. The compensation points are defined by the user and may be extended to the boundaries of the field to also correct for scatter contributions with depth. The corresponding error with respect to the local field minimum is plotted below the dose profile.

The compensator shape is then output into the format required for the ATP algorithm and entered. The resulting distribution is then computed and the process is repeated. For later iterations, the dimensions of compensation field are unchanged, however, the target dose level within the field of compensation is changed. In order to ensure that the amount of material

used is kept to a minimum, the average dose within the field of compensation of the first corrected profile is used as the target dose for compensation. Since dose values may be less than the average dose, material may be removed from the existing compensator in order to achieve field flatness. The removed material is often very small and under no instances has this method yielded a negative thickness. Even if this were the case, the thicknesses are rescaled such that the least amount of material used within the field of compensation is kept to a minimum. This ensures that the full extent of the beam is not (unnecessarily) uniformly attenuated. The process can be repeated as many times necessary to achieve the desired flatness.
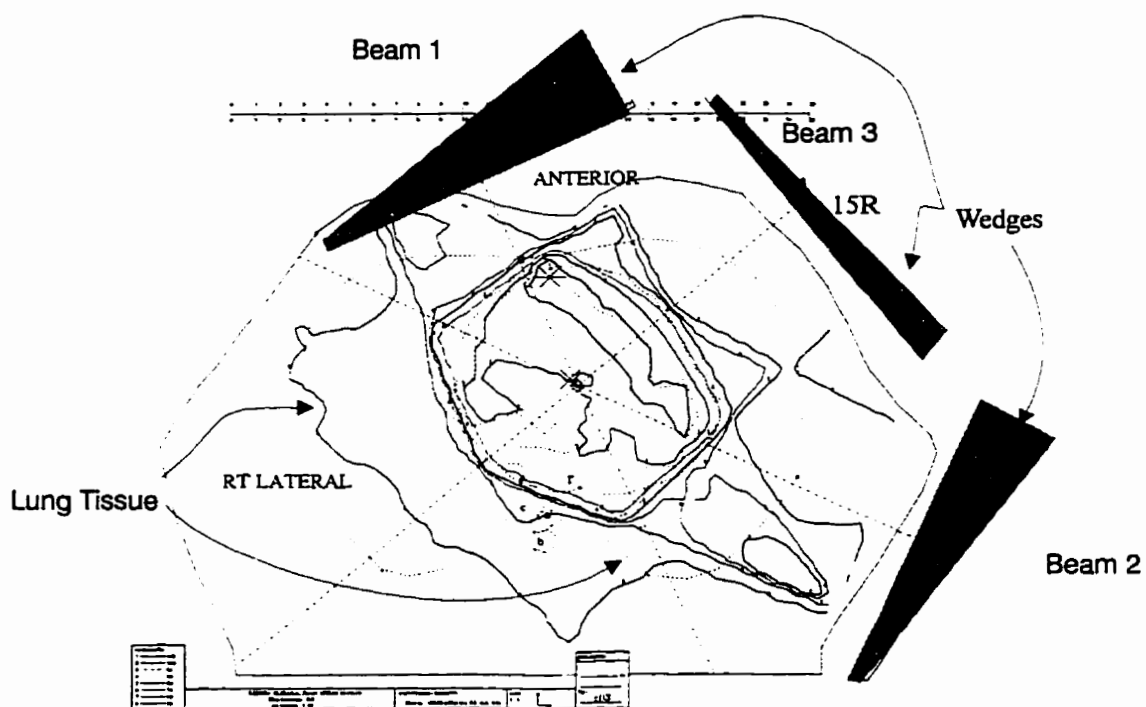
Figure 5.12: Patient anatomy and treatment plan configuration of the first phantom.

Often, this method will overlook the effects of lateral scatter and may unnecessarily attenuate the beam at point resulting in sharp dose "discontinuities". The algorithm tests for field discontinuities by computing the derivatives of the open and first corrected fields. If there are large changes in the derivatives, sharp boundaries potentially exist within the corrected

field and the user is prompted. If the dose matrix cannot be increased, the process halts and the compensator constructed from the first iteration is stored and used.

The algorithm was tested within the ATP environment for the second phantom illustrated in Section 5.1.1 and again for a realistic phantom consisting of both internal and external inhomogeneities, shown in Figure 5.12. Beam 1 is compensated beam, without the wedge in place, for this simulation.

5.2.2 Results and Discussion

Figures 5.13a-d, 5.14a-d, and 5.15a-d display the outputs of the algorithm for the first, second, and third iteration for the lung phantom. The solid lines illustrate the distributions after the iteration where the hatched lines illustrate the distributions of the open field and previous iterations. With each pass, dose within the correction points becomes more uniform, up until convergence is met with the third pass. The final distribution of the compensator constructed for the lung phantom shows improved homogeneity at the target depth as illustrated in Figure 5.15a. Minor artifacts are observed in the shadow of the lung interface. The ATP algorithm implies that the average error in the compensated field is 1.7% where the maximum error is 4.6 %.

The dose profile normalised to the central axis point is displayed in Figure 5.16 for the open field and first corrected profiles in the patient phantom. Figure 5.17 displays isodoses normalised at the isocentre to illustrate the distributions up and down stream and the degree of homogeneity at the target site. Because of the tissue deficit on the right side of the beam, there is an increase in beam intensity at the right side of the mediastinum. On the left side of the beam, there exists more lung tissue. Therefore, the beam intensity is lower initially, but begins to "catch up" while traversing through the less dense lung tissue. The compensator correctly accounts for both the internal and external inhomogeneities such at a relatively homogeneous distribution is observed at the ordinate perpendicular to the beam's axis.

The trr method consistently undercorrects the dose at depth while the iterative method overcorrects. This is best exemplified by comparing the compensator shapes predicted by the trr method (shaded region) and the iterative method (dotted and solid lines) shown in Figure 5.14d. Clearly, the compensator constructed through the iterative method will attenuate the beam intensity more than the trr constructed compensator. There may be negative consequences for this overcompensation. The overcorrection may underdose the target plane by an amount equal to the error of the inhomogeneity algorithm. Structures upstream will also be underdosed accordingly. When a multibeam arrangement is used in the plan, this may have consequences to the overall dose distribution. This will be discussed further in the next section.

The overcompensation can be avoided by placing a larger error tolerance during the compensator construction. For these simulations, an error of 2% was used to determine whether material needed to be added or not. This seemed to be a reasonable limit given the results from earlier experiments. A smaller error limit will not only overcorrect, the number of iterations required will increase. Divergence in the field homogeneity becomes a problem when the number of iterations are increased. Overcompensation can be avoided by allowing the iterations to halt after one pass or by scaling the thicknesses of material by a factor less than unity. The average electron density along the central beam's axis would be suitable for

the scaling parameter since that value would properly correct for primaries along the central axis; in effect being a reduction ratio.

Divergent solutions are observed when there is an overcorrection of underdosed portions of the beam or an undercorrection of overdosed portions of the beam. These "artifacts" are dependent on the compensator thickness to dose matrix resolution and alignment of the compensator geometry to the dose matrix. Slight shifts in compensator may greatly amplify the loss or build up of dose along the periphery of sharp geometric or density boundaries (including the penumbra). In order for avoid potential misalignment, the resolution of the compensator should be less than or equal to the dose resolution multiplied by the ratio of source-to-tray and source-to-compensation plane distances. This ensures that the compensator is observed as a smooth function relative to the dose matrix. In addition, the compensator thickness should lay in-line with the calculated dose points.

Both phantom simulations would suggest that reasonable uniformity is achievable through this iterative procedure. Both distributions in the simulations show flat distributions within the points of compensation.

Figure 5.13a: Open dose profile.

Figure 5.13a: Open dose profile.

Figure 5.13b: Open isodose.
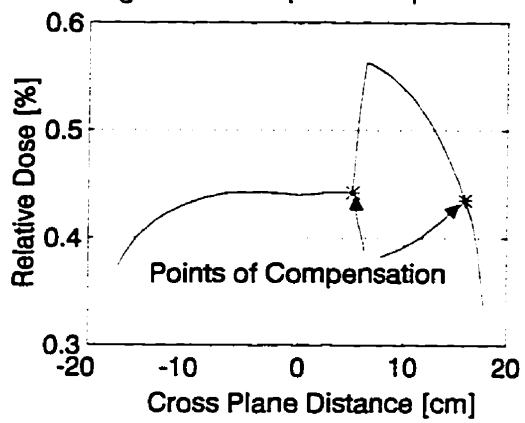
Figure 5.13b: Open isodose.

Figure 5.13c: Relative error.

Figure 5.13c: Relative error.
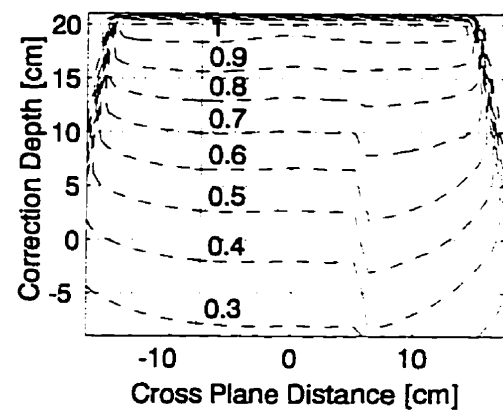
Figure 5.13d: Height of compensator.
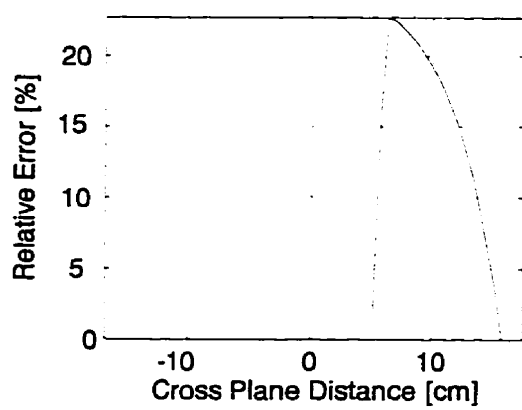
Figure 5.13d: Height of compensator.
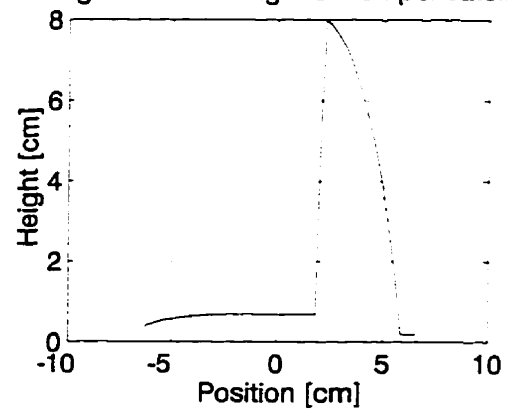
Figure 5.13a-d: First correction outputs.

Figure 5.14a: Open and first corrected dose profiles.
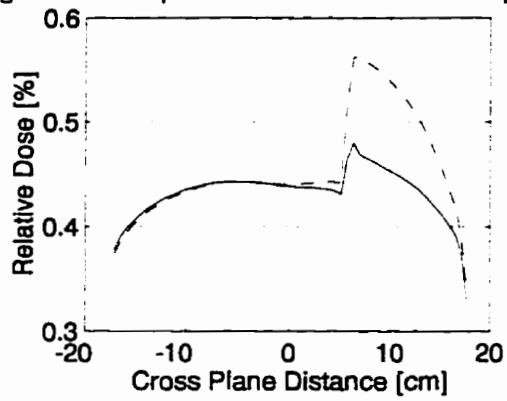
Figure 5.14b: Isodose profiles.

Open Field
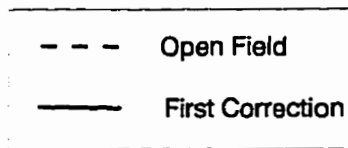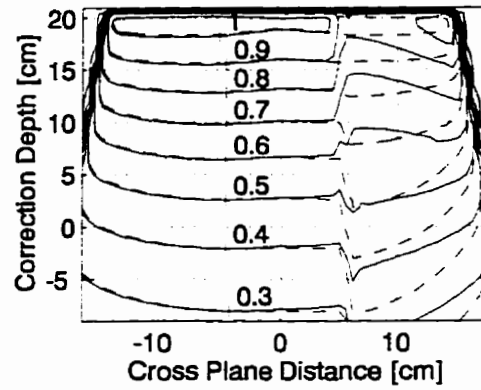
First Correction

Figure 5.14c: Relative error with first correction.
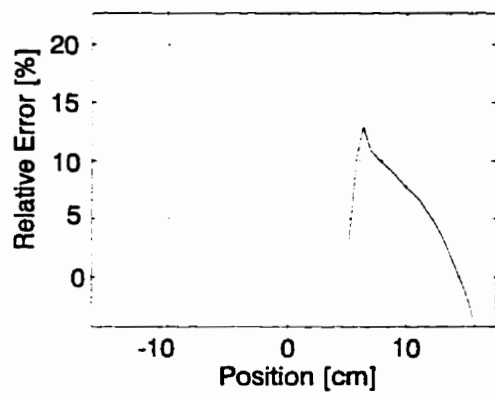
Figure 5.14d: Height of compensators.
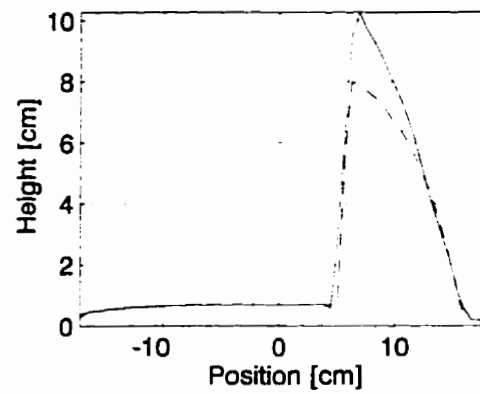
Figure 5.14a-d: Second correction outputs.

Figure 5.15a: Open and third corrected profiles.
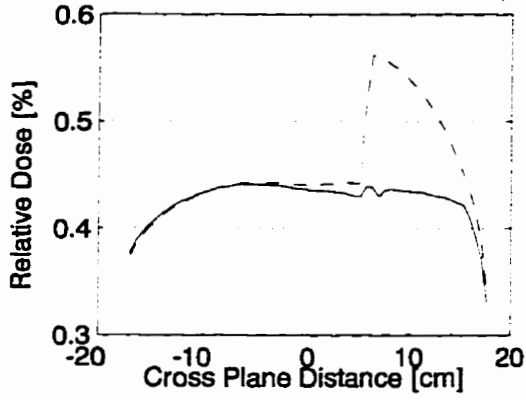
Figure 5.15b: Isodose profiles.
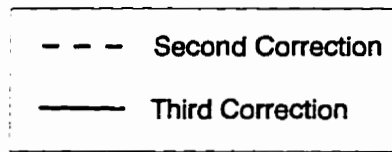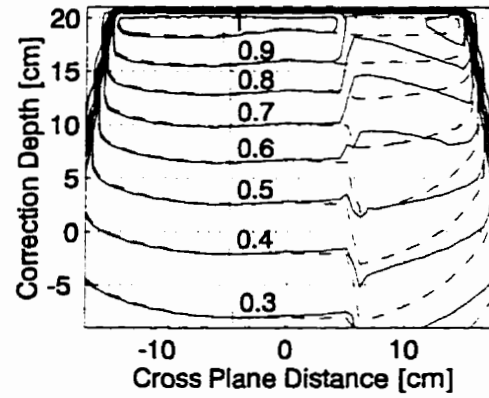
Figure 5.15c: Relative error with third correction.
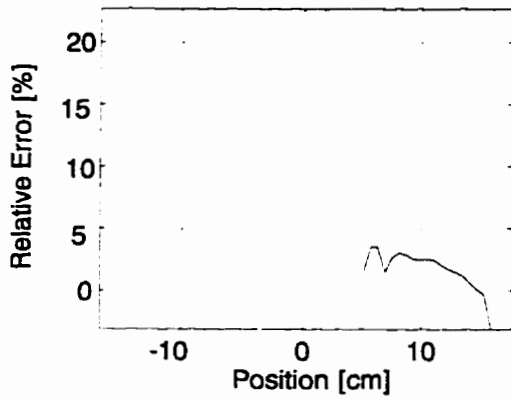
Figure 5.15c: Height of compensators.

TRR compensator shape
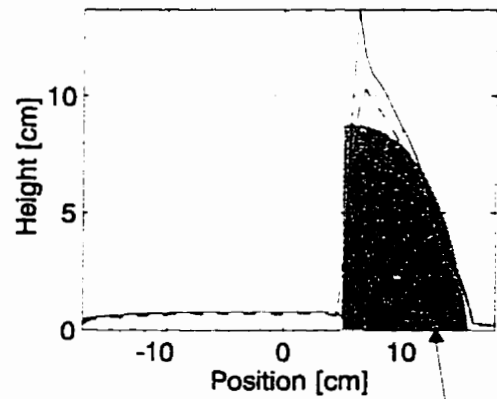
Second Correction

Third Correction

Figure 5.15a-d: Third correction outputs.
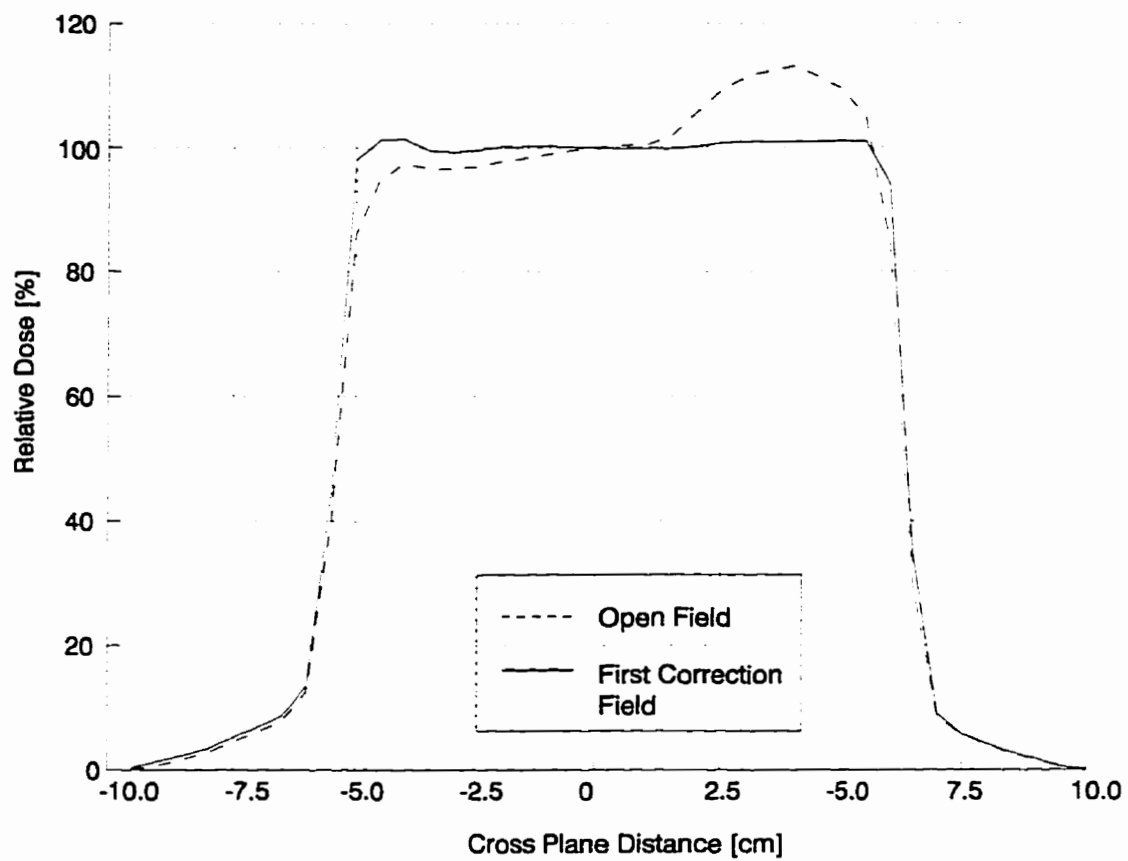
Figure 5.16: Open field and first corrected field for Beam 1.

Figure 5.17: Open and first correction isodoses for Beam 1.
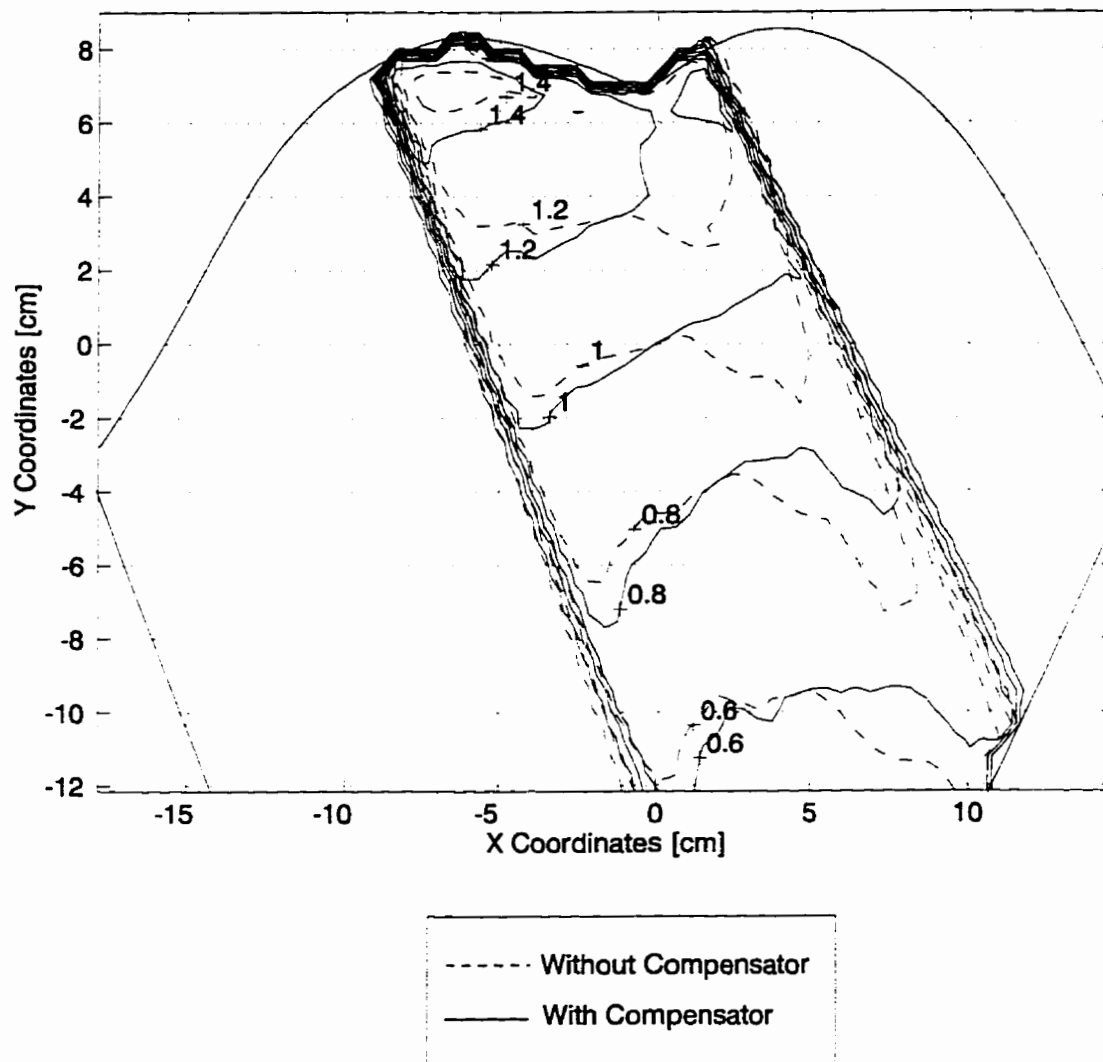
5.3 Treatment Plan Optimisation: Multibeam Optimisation

We have discussed a technique that establishes a uniform distribution at depth given internal and external inhomogeneities. For multibeam arrangements individual compensation can be carried out for each beam so as to create a flat distribution for each beam at a desired depth. This alone will not be sufficient to produce a uniform distribution for a planning target volume. To create a uniform distribution, the gradient vector method can be employed to achieve a uniform volume with a PTV.

As mentioned in Chapter 3, Sherouse (1993) has proposed a simple mathematical technique to create a uniform distribution at depth for a uniform density phantom with no external contour variations. In the gradient vector approach, each beam is completely

characterised through a vector with a magnitude. The magnitude is primarily determined by the beam weight, whereas the direction is determined by the angle from a line perpendicular to the isocentre's isodose to the beam's central axis (See Figure 3.6). The angle of the gradient vector is a function of gantry, collimator, wedge and table rotations.

In clinical situations, the isodose angle will also be a function of the patient contour and internal heterogeneities. It is very unlikely that there is a flat isodose distribution at the patient's isocentre patient given the presence of internal and external contour variations. However, techniques for developing a uniform distribution at depth have been discussed and developed in the previous sections. Thus, by performing the corrections at a plane perpendicular to the central axis within a patient, we can employ the gradient vector technique to achieve a uniform distribution for a volume as if the phantom had no internal or external heterogeneities. This then establishes uniform profiles at the isocentre much like a uniform density phantom. It then becomes possible to assign each beam a vector and employ the technique described by Sherouse.

When developing the treatment plan, we rely on the expertise of a treatment planner to define the beam sizes and beam entry points. Specifying the beam entry points fixes the gantry and table angles. Left for manipulation are the collimator and wedge angles, and the beam weightings. A null gradient vector is sought by allowing the wedge and collimator angles and beam weightings to vary. There often are a large number of solutions since the problem is overspecified algebraically. Finding a solution may be done in one of two ways.

First, one can iterate all possible wedge angles, collimator angles, and beam weightings to find a global minimum vector. This process would be time consuming since the range of potential wedge and collimator angles and beam weightings are large. The potential configurations increase geometrically when more beams are added. In addition, the global minimum solution may not produce the most homogeneous distribution for the planning target volume. Employing the gradient vector approach most likely will produce a homogeneous distribution at and about isocentre. The dose to peripheral structures may vary, depending on factors such as the amount of inhomogeneous tissue, wedge and collimator angles, and beam weightings. The dose to these peripheral structures must be monitored if such an iteration is performed.

The second approach is to define some of the parameters in this algebraically overspecified problem. One approach is to define wedge angles to available physical wedges. In addition, one can define the beam weightings so that they lie within a given range of potential values. This restricts the magnitude of the gradient vectors and, thus, the collimator and wedge angles will vary correspondingly. If a coplanar, i.e., the entry points lay in a plane, plan is desired collimator angles need not be specified. This would be tantamount to saying the treatment plan does not involve a table rotation. This then greatly minimises the potential solutions that one can generate.

5.3.1 Methods and Materials

Two CT images of a patient anatomy and a tumor volume were obtained; one that already contained a treatment plan of a patient receiving a large field thoracic plan at the CCI, the other consisting of contours entered in ATP for a typical NSCLC coin lesion defined by an Oncologist. The first plan, shown in Figure 5.12, already contained information regarding

beam entry points, beam sizes and weightings. For the second phantom, shown in Figure 5.18, beam entry points, beam sizes and weightings were devised with the aid of an experienced dosimetrist. The gantry angles and beam widths were specified such as to avoid dose to critical structures, such as the heart and spinal cord, that lay adjacent to the coin lesion. Both plans were performed on two dimensional slices and the plans were isocentric about the target center. The configurations mimic what is often encountered in conventional two dimensional CT treatment planning.
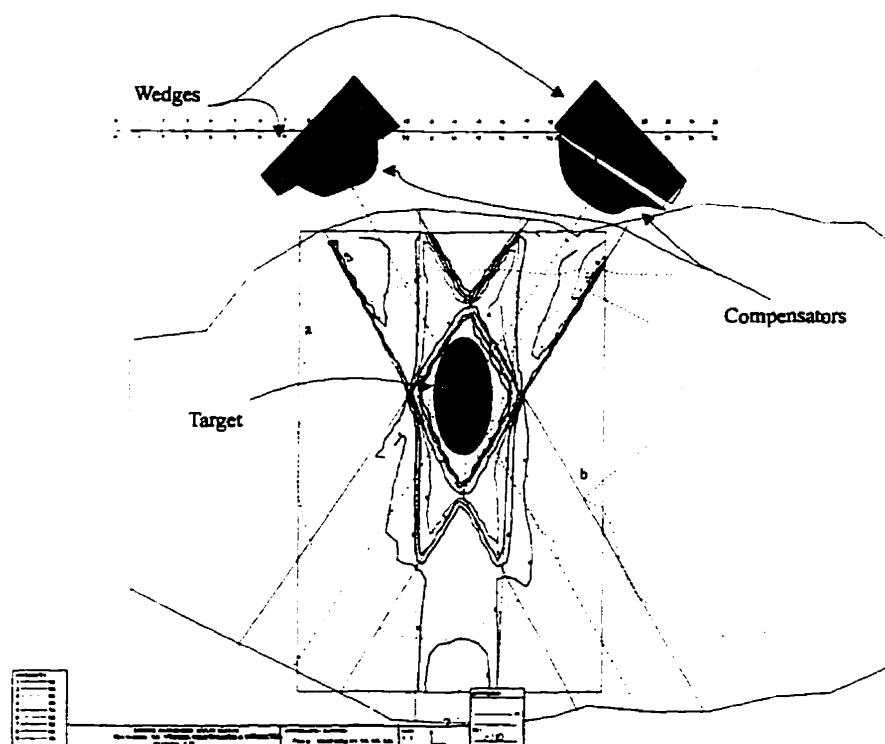
Figure 5.18: Patient anatomy and treatment plan configuration of the second phantom.

Each beam was compensated, through the iterative method, to a plane perpendicular to the central axis. The iterative algorithm employed in Section 5.1.2 assumed normal incidence to the target. To extract the open dose profile for beams at various gantry angles, a subroutine was constructed that can extract the plane desired dose through rotating the dose distribution by the gantry angle. It was later found that interpolation artifacts from rotating the matrix may produce erroneous compensator thicknesses. Since the number of beams were not great, the patient's contours were rotated and entered in ATP as if the gantry angle was zero and the patient was rotated opposite to the gantry rotation. The tolerance for uniformity was set at 2%.

Following compensation for each beam, full field distributions were computed with their appropriate beam weightings.

Both plans were two dimensional, therefore, the constraint of collimator settings could be circumvented by avoiding all table rotations. The selection of appropriate wedge angle and beam weightings for each beam was computed by hand with the gradient vector approach. For instance, consider the second phantom. Let G_1, G_2, G_3, w_1, w_2, and w_3 be the gradient vectors and beam weightings for beams 1, 2, and 3. The planner has specified the following: three beams are to be used, where $\varphi_1 = 32°$, $\varphi_2 = 181°$, and $\varphi_3 = 331°$. Also, the planner has specified that $w_1=w_3$, and w_2 be no less than 0.26, which implies $w_1=w_3=0.37$. We have,

$$\bar{G}_T = w_1\bar{G}_1 + w_2\bar{G}_2 + w_3\bar{G}_3 .$$

Each beam can be decomposed into its axial and longitudinal equivalents. Since the magnitude of the axial component scales with beam weight, regardless of wedge angle. the magnitude of the transaxial component will be,

$$G_{i,tr} = G_{i,ax} \cdot \tan(\varphi_i) .$$

We wish to obtain a total vector, described as the sum of axial and longitudinal components, equal to zero. The longitudinal components are perpendicular to the axial vectors. A gantry rotation produces a rotation in the axial vector. We wish to achieve,

$$0 = \sum_{i=1}^{3} G_{i,ax} + \sum_{i=1}^{3} G_{i,tr} , \text{ or in the patient coordinate system,}$$

$$0 = \sum_{i=1}^{3} w_i \left[\sin(\varphi_i)\hat{i} + \cos(\varphi_i)\hat{j}\right] + \sum_{i=1}^{3} w_i \tan(\phi_i)\left[\sin(\varphi_i + 90)\hat{i} + \cos(\varphi_i + 90)\hat{j}\right].$$

We can substitute the beam weightings and gantry angles to solve for the wedge angles. We constrain wedge angles to physical wedges, available in multiples of $15°$ up to $60°$. After some algebra, we produce two simultaneous equations for the unit vectors $\hat{i}$ and $\hat{j}$ with the gantry angles as unknowns. The exact solution of the two equations will not yield a null gradient since we constrain the wedge angles to be in multiples of 15, up to a maximum of 60. However, as long at the resultant gradient vector has a magnitude less than the beam weighting, a uniform distribution can be achieved. The resulting wedge angles and beam weightings are displayed in Table 5.2, which displays one solution of potentially many.

It was found that for the first phantom, a slight modification in the gantry angles produced a zero gradient vector. Therefore, the plan as devised by the treatment planner was slightly modified. Table 5.1 displays the beam configuration by the planner and those generated through the gradient approach. Displayed is one solution of potentially many.

	Beam 1	Beam 2	Beam 3
Gantry Angle	333 (335)	105	50
Wedge Angle	45R	45L	15L
Beam Weight	0.33 (0.37)	0.33 (0.37)	0.34 (0.26)

Table 5.1: Beam data for the first phantom. The planner's results are in brackets if different form optimised plan.

	Beam 1	Beam 2	Beam 3
Gantry Angle	32	181	331
Wedge Angle	60L	0	60R
Beam Weight	0.37	0.26	0.37

Table 5.2: Beam data for the second phantom.

For the first plan, the resulting dose distribution could be compared to the treatment planners dose distribution. The two plans differ primarily through the introduction of compensators for each beam. Thus, each of the plans were compared with and without compensators. The effect of the wedges on the compensated distributions was also examined. The dose "area" histograms of the 2D plans were computed for the target volume and the surrounding structures to assess potential biological risk. Lastly, the PTVs for each of the distributions were examined for uniformity of dose and the normal tissues located upstream the beams were examined.

5.3.2 Results

Figures 5.19a-d display the dose profiles, isodose profiles, relative error, and final shape of the compensator for the first phantom (displayed in Figure 5.12). All beams in the first plan required one iteration to produce a reasonably flat isodose distribution at isocentre. The displayed distributions are shown normalised to isocentre; this normalisation was not chosen in the development of the individual compensators. They are normalised at the isocentre here to display the field flatness and variability of dose up- and downstream.

Figures 5.20a-c show the compensated distributions of the three beams. At the isocentre point, which has its coordinates at the origin, field flatness is achieved for all the beams in this plan. The introduction of the wedges into the fields is displayed in Figures 5.21a-c. For uniform density phantoms with no surface variations, the wedge serves to tilt the isodoses about the central axis. The wedge angle is defined as angle between the isodose curve and the plane normal to the central axis. Wedges are often constructed to establish the angular tilt at a depth of 10 cm below the surface in a uniform phantom. There are minor perturbations in the dose profiles after the introduction of the wedges. This is due to the existence of internal density and contour variations. Because the beam intensity is modulated significantly to create the isodose effect, the modulation has consequences to most notably the primary photon dose contribution at the compensated plane. If the phantom had surface contours but no internal density variations or contours, the compensator would be a missing tissue compensator.

Figure 5.19a: Open and first corrected dose profiles.
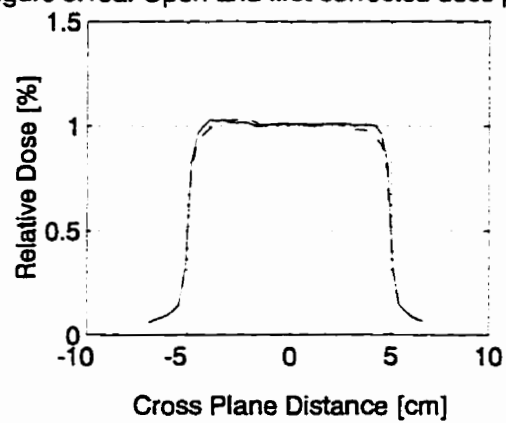
Figure 5.19b: Isodose profiles.

Cross Plane Distance [cm]

Cross Plane Distance [cm]

- - - Open Beam
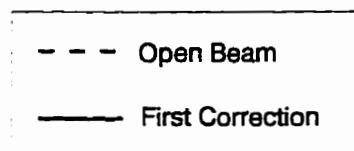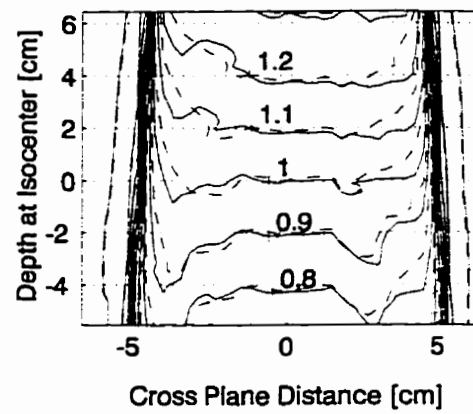
——— First Correction

Figure 5.19c: Relative error after primary correction.
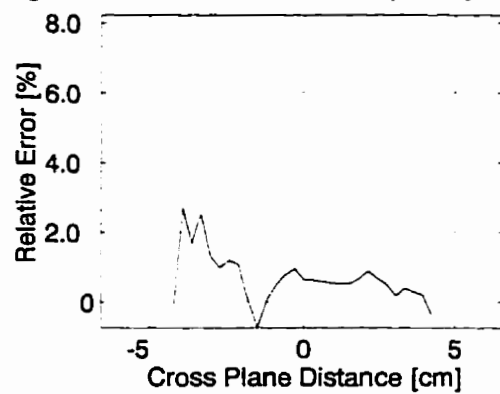
Figure 5.19d: Height of compensator.

Cross Plane Distance [cm]

Position [cm]
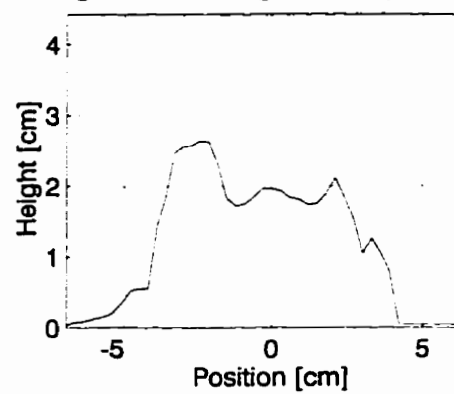
Figure 5.19a-d: First correction outputs.

Figure 5.20a: Isodose profiles for Beam 1.
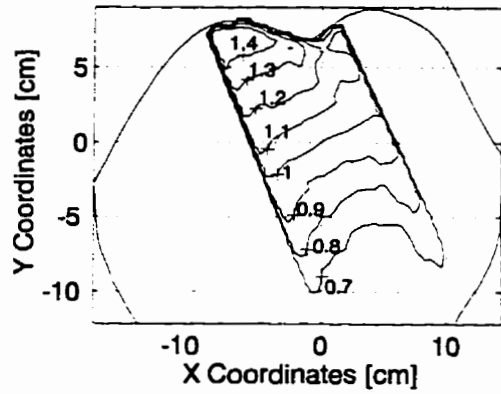
Figure 5.20b: Isodose profiles for Beam 2.
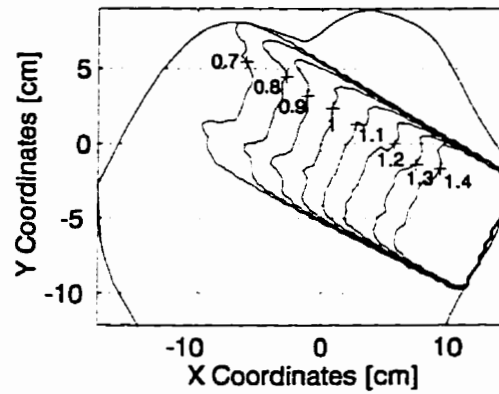
Figure 5.20c: Isodose profiles for Beam 3.
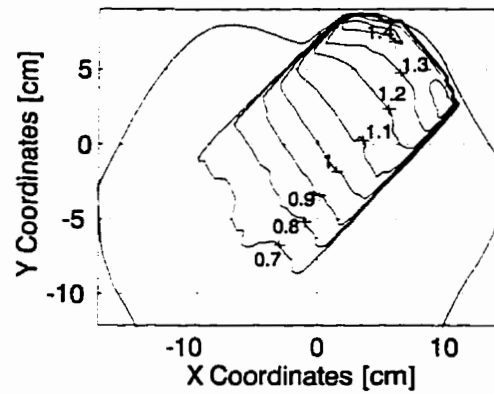
Figure 5.20a-c: First correction isodoses.

Figure 5.21a: Wedged isodose profiles
for Beam 1.
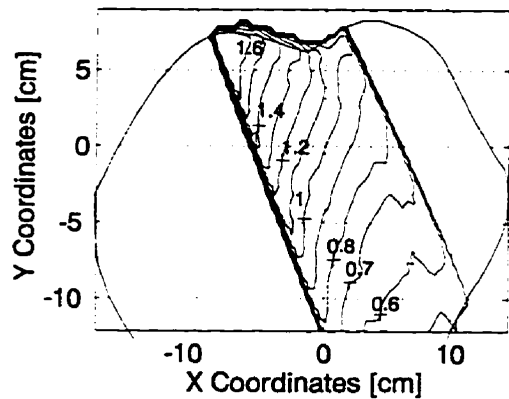
Figure 5.21b: Wedged isodose profiles
for Beam 2.
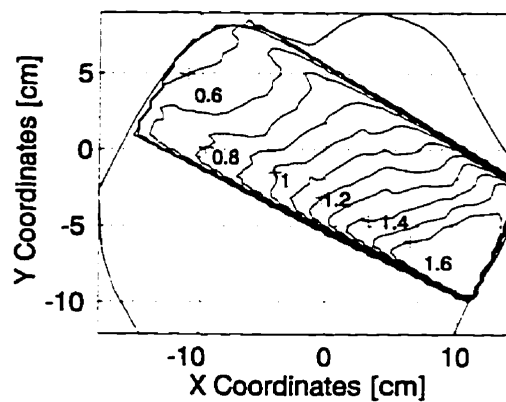
Figure 5.21c: Wedged isodose profiles
for Beam 3.
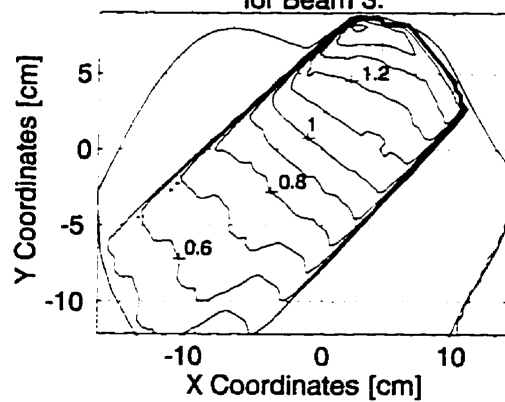
Figure 5.21a-d: Corrected and wedged isodoses.

Figure 5.22: Optimised dose distribution for the first phantom.
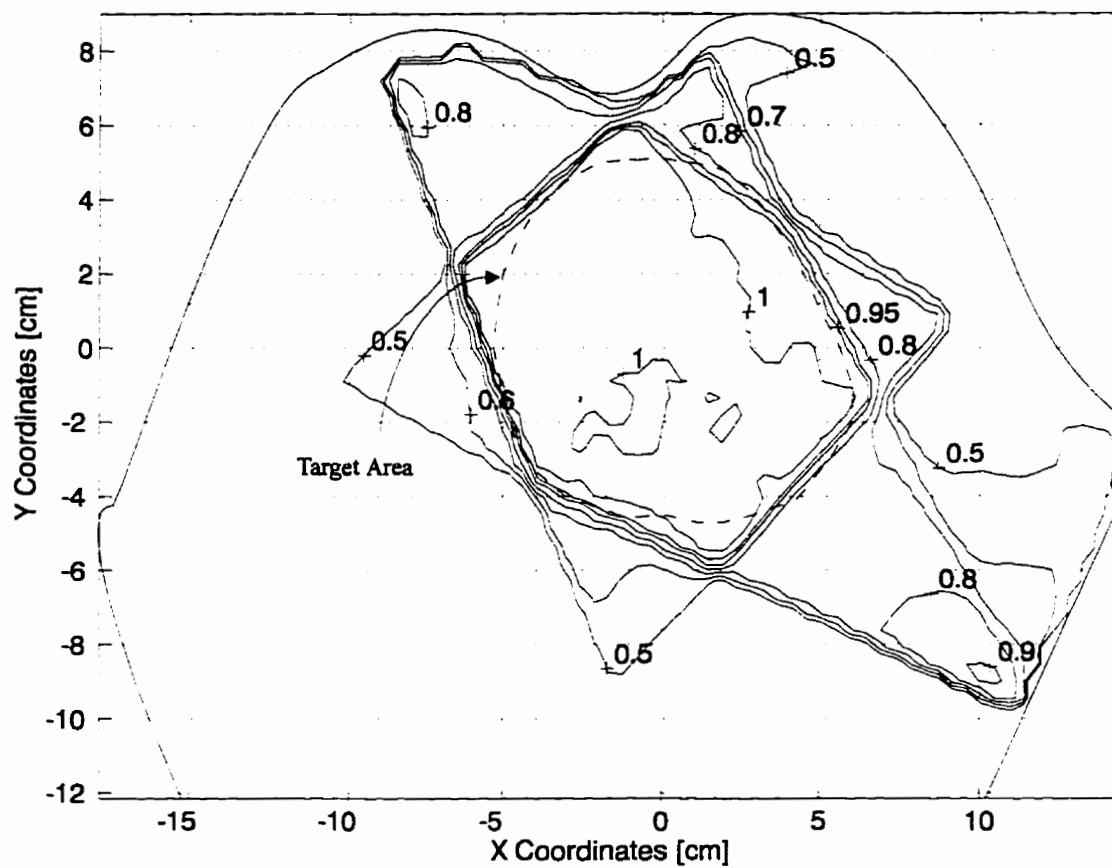
Figure 5.23: Total dose distribution of the original plan.
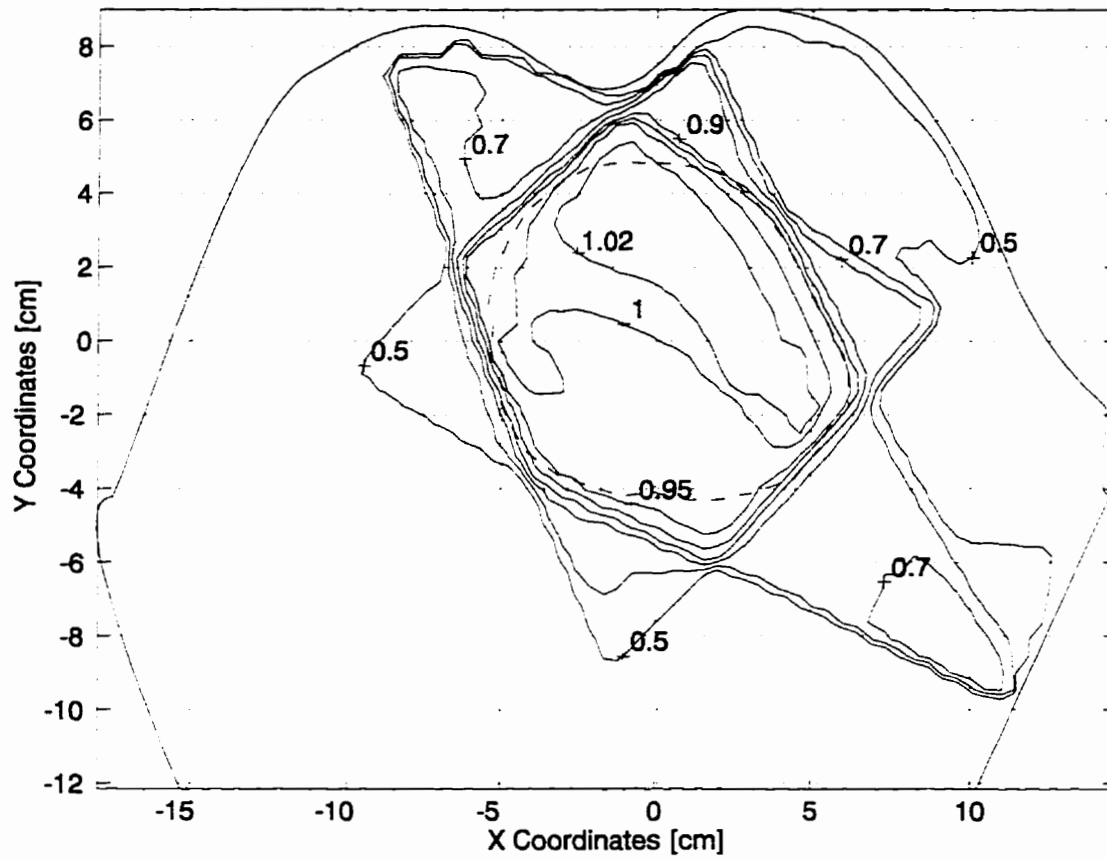
Figure 5.24a: Optimised minus original plan.   Figure 5.24b: Original minus optimised plan.
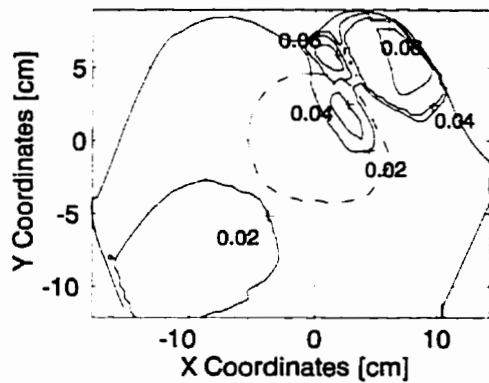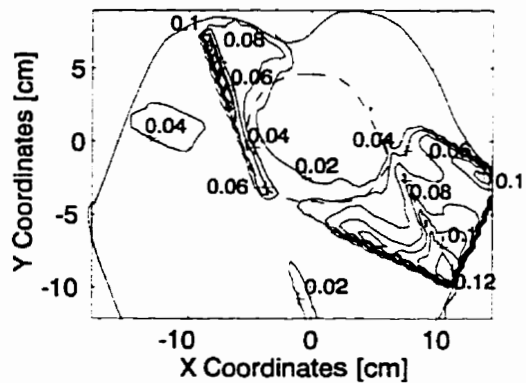
Figure 5.24a-b: Dose difference maps of optimised and original plan.
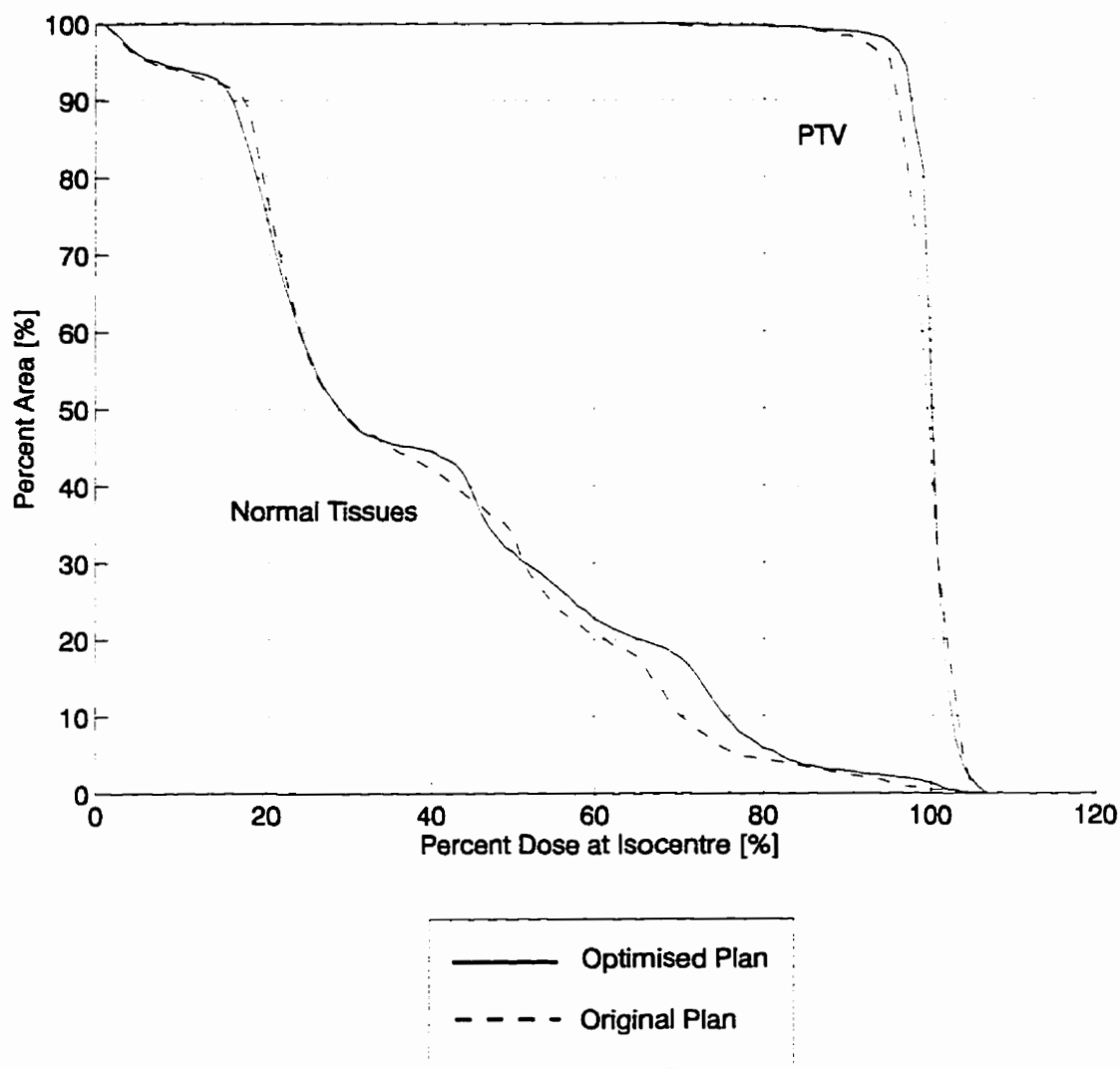
Figure 5.25: Dose area histograms of optimised and original plan.

With such a phantom, a flat and tilted isodose distribution would be expected, much like the wedge distribution on Figure 3.12, excluding beam hardening effects. The internal structures will invoke higher primary and lower scatter dose contributions from those contributions generated in a uniform distribution.

The complete optimised plan for the first phantoms is displayed in Figure 5.22. The optimised dose distribution exhibits slightly improved uniformity through out the PTV. For comparison, Figure 5.23 displays the original plan as generated by the planner. Both show high uniformity as the 95% isodose line wraps the target reasonably well. To illustrate the differences in the two distributions, a dose difference map is generated in Figures 5.24a-b. Figure 5.24a is the optimised plan minus the original plan, and Figure 5.24b is the original plan

minus the optimised plan. In the optimised plans, the beams develop "horns", or a build up of dose at the entrance and to the sides of the central axis. This is primarily due to the lack of modeling the penumbra and the build up of dose off axis.

The resultant effects of the additional dose to the normal tissue is best illustrated in the dose area histogram in Figure 5.25. At lower doses, less healthy tissue is irradiated, however, at higher doses, more healthy tissue is irradiated. This may be some cause for concern for this method.

Despite the overdosing of normal structures upstream, there appears to be improved homogeneity in dose throughout the target volume. The hot spot within the PTV in the original plan is reduced in the optimised plan. Also, along the periphery of the PTV, doses homogeneity is improved. The improvement in dose homogeneity is primarily due to the tissue compensation. More inhomogeneous material is present by the edges of the fields resulting in greater deposited dose than at the central axis. The compensator decreases the beam intensity along the central portions of the beam so that the energy fluence becomes more uniform at the corrected plane.

The average dose within the PTV is $100.5 \pm 2.8\%$ and $99.9 \pm 3.5\%$ of the isocentric dose within one standard deviation for the optimised and original plan; thus, it would seem that there is slightly improved homogeneity when comparing the plans. The corresponding dose area histograms for the PTV are displayed in Figure 5.25; again showing little improvements in the resulting dose.

It would appear that for large field treatments, the optimisation does little to improve the dose distribution. This is not the case for the smaller coin lesion; generally, the dose distribution displays much more uniformity of dose within the PTV when comparing distributions generated from uncompensated and compensated profiles. The dose distribution for each beam of the second optimised plan is shown in Figures 5.26a-c.

a: Beam 1

b: Beam 2

c: Beam 3
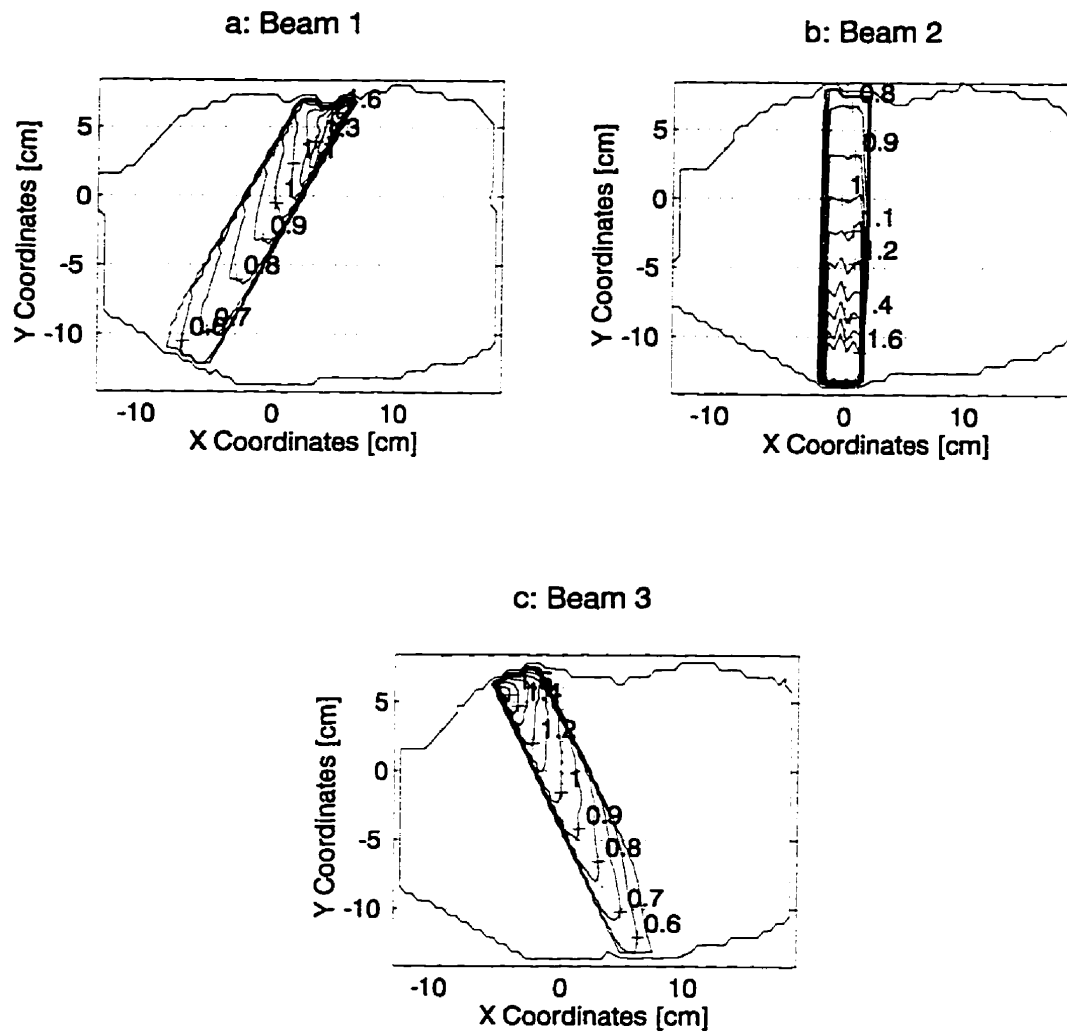
Figures 5.26a-c: Corrected and wedged isodose profiles.
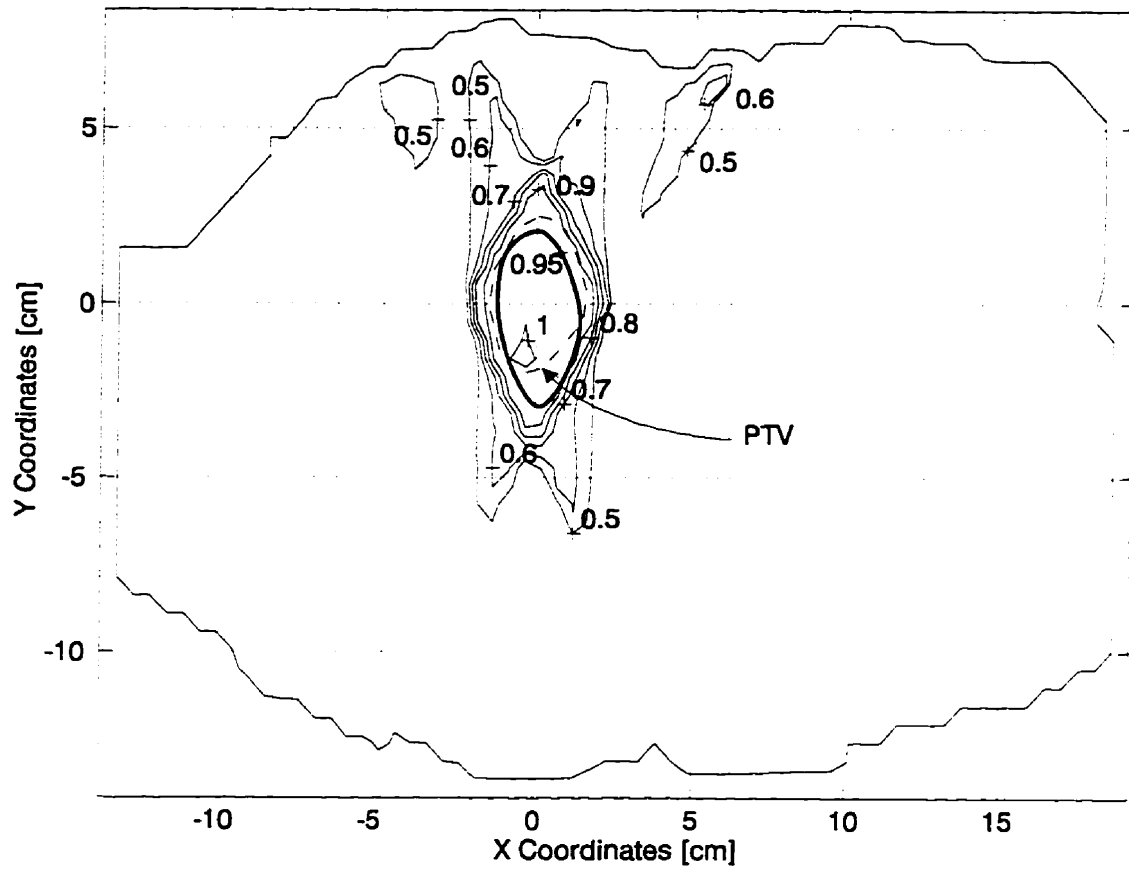
Figure 5.27: Total distribution of optimised plan.
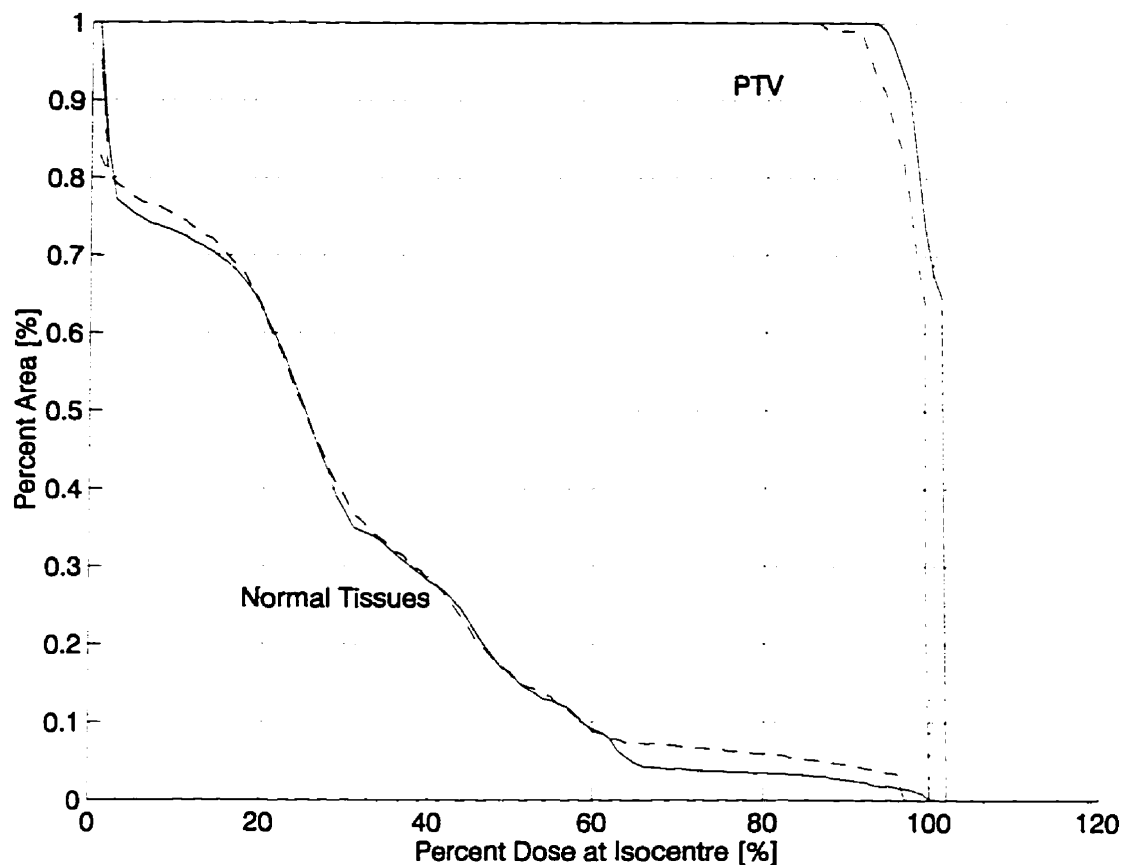
Figure 5.28: Dose area histograms of optimised and original plan.

For the uncompensated plan, the dose within the PTV ranges from 83% to 100% of the dose to isocentre. With the addition of compensators, the dose distributions display higher dose gradients as well as improved homogeneity. For the compensated and wedged plan, the dose homogeneity of the target ranges from 92% to 102% of the dose to isocentre.

The dose area histograms illustrates in Figure 5.28 that the difference in the uniformity in dose, where the fall off by the 100% isodose line is slightly sharper. The target also receives more dose than the prescription dose for the compensated plan. For normal tissues, less volume is irradiated to dose 65% or less than the dose to isocentre. More healthy tissue is irradiated at doses greater than 65%. The healthy tissue irradiated at the prescription dose is due to the treatment plan configuration. The average doses delivered to the target is 98.3 ± 1.7% and 96.1 ± 2.7% for the compensated and uncompensated beams. Uniformity is slightly better with fewer deviations for the optimised distribution. Employing a higher dose resolution may illustrate the dosimetric effects more accurately, however, the computations were performed at ATP's highest dose resolution, which in this case was 0.6 cm/pixel.

Again, it is worth pointing out the differences in the dose steepness, or gradients, at the beam intersection points. This is best illustrated through Figures 5.29a&b that magnify the

dose distributions at the target. The distance between the 70% and 90% isodose lines is at most 0.47 cm in the compensated plan where the distance is at most 1.87 cm in the uncompensated plan.
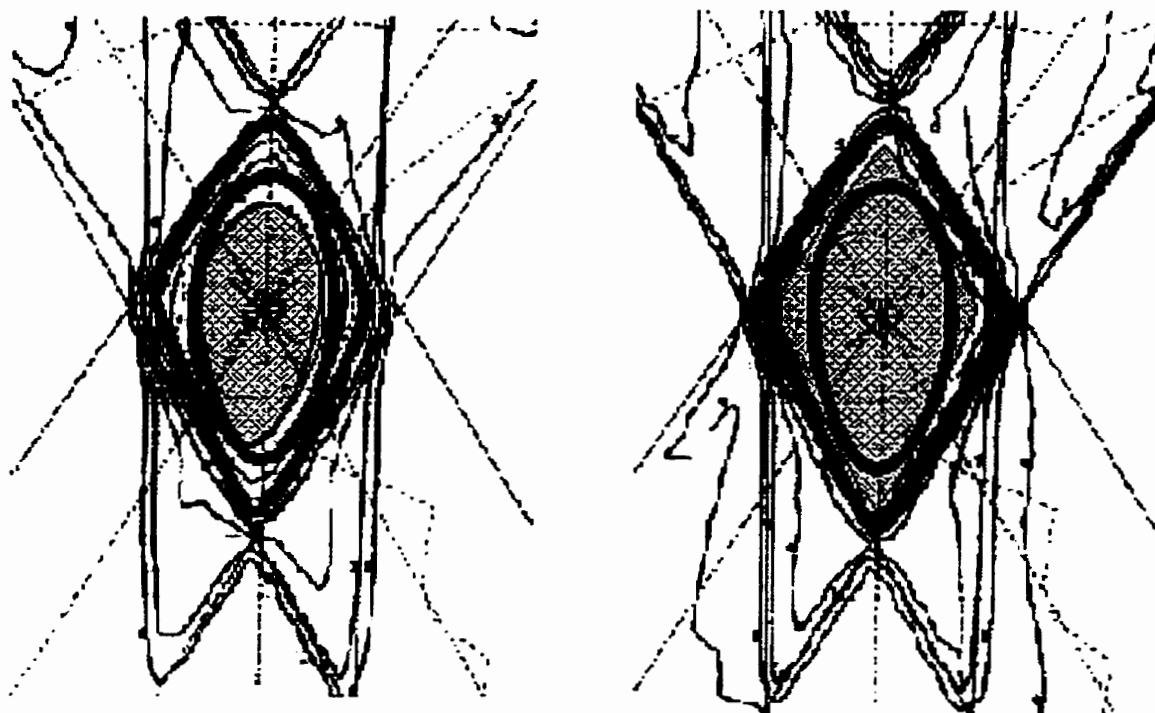
Figure 5.29a-b: Uncompensated and compensated dose plans. The innermost isodose displays the 100% dose contour and is shaded light gray. The external contours display the 70% isodoses which are the darker gray lines. The target is the thick black line.

5.3.3 Discussion

The purpose of this simulation was to investigate the gradient vector approach while considering internal and external inhomogeneities. The beam optimization routine employed for the two phantoms illustrate that a high and uniform dose can be delivered to the PTV provided that the beam covers the dimensions of the PTV adequately. The distributions exhibit very sharp dose gradients at the point of beam intersection and conform tightly to the beam intersection points. It appears that the smaller fields benefit greatly from the beam compensation. For larger fields, the benefits are not as obvious. However, analysis of the dose volume histograms imply that substantially improved dose uniformity is achievable through compensation.

Although the technique shows little improvements over the conventional approach for large field treatments, much of the guess work is circumvented by employing some simple

mathematics. The greatest advantage of this technique is its adaptability to three dimensions. For these simulations, the plans were constrained to two dimensions. The optimisation for these plans required seeking suitable wedge angles since gantry angles and weights were predefined. Through the conventional method, solutions can be sought rather easily because the optimisation is constrained for solutions generated within a transverse plane. Extensions of this method to three dimensions would require optimisation of wedge and collimator angles if table and gantry angles are predefined. This is much more difficult to visualise. For this reason alone, the gradient vector approach is a fruitful method of generating solutions for treatment planning, regardless of the degrees of freedom in the treatment plan configuration. These simulations suggest that compensation for large field treatments little improvements are observed in the overall dose distributions. For smaller fields, compensators used within this framework may generate highly uniform doses to PTVs and conform tightly to the beam intersection points. Due to the shape of the dose area histograms, it is reasonable to assume that there may be a clinical advantage to compensating the isodose plan. Provided that the beam configurations adequately cover the PTV, the dose to the target generally will be more uniform for the lung inhomogeneity corrected plans. By the same token, however, there potentially exists a clinical disadvantage from the additional dose the surface receives from the "horns" in the beam. The horns may arise at regions where the plane of compensation lies outside the patient, such as in head and neck treatments, or alternatively, when the plane of compensation is in the build up region. This additional dose can be reduced by adequately modeling the penumbral effects and the relative off axis dose during compensator construction [Mageras et al. 1991].

The simulations suggest that improved homogeneity to the target volume can be achieved through one correction of the open beam profiles. Additional corrections may be pursued but the clinical benefits decrease through the increased importance of primary dose and beam weightings in the multibeam plan. More over, the correction need not be an entirely accurate one. Figure 5.30a&b illustrates the dose profile and relative error of the first corrected field for beam 2 in the second phantom. Although the errors in the compensator profile are greater than 4% at the edges of the field, its cumulative effect to the resulting distribution is not a factor to the combined field distribution.

Errors in the simulations stem primarily from the accuracy calculation algorithm itself. It was previously found that errors using the Batho inhomogeneity correction algorithm are approximately 2% with a maximum error of 5%. It is much easier to simulate these experiments on computer than to perform physical measurements *in vivo*. Given that our uncertainty in computed dose is less than or equal to the ICRU 50 recommended limit of $\pm 5\%$, errors in dose homogeneity seem acceptable. Thus, physical measurements employing this technique, even if possible, are not necessary.

Figure 5.30a: Dose Profiles of Open Beam and Primary Correction

Figure 5.30b: Relative Error with Primary Correction
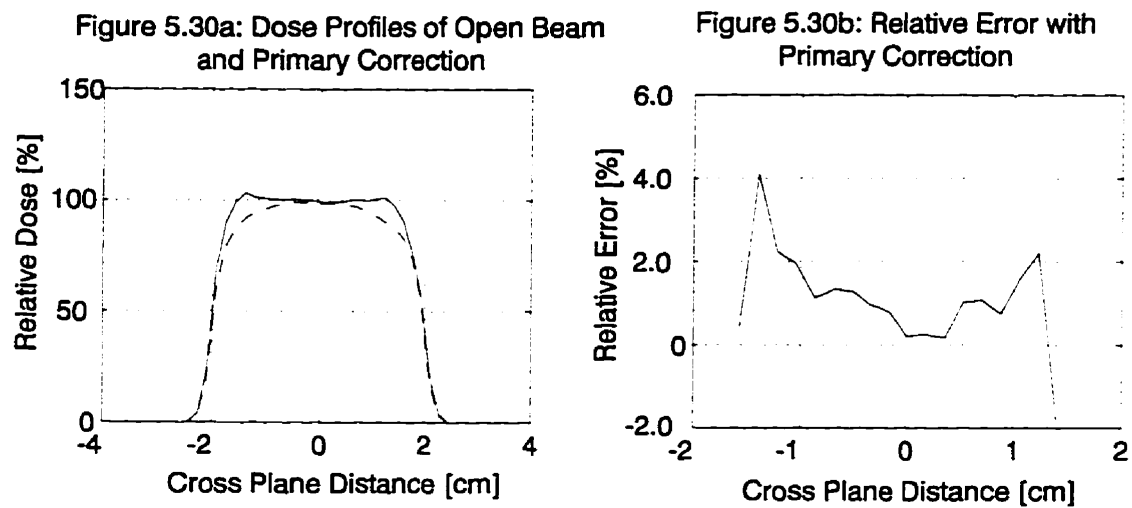
Figure 5.30a-b: Dose and error profiles after primary correction.

6. Effects of Respiration in Lung Cancer Treatment

A volumetric change of the thorax due to respiration may modify the dose delivered to a target by an external photon beam in two ways. First, there may be fluctuations in lung density during respiration that could result in a change in the photon interactions, thereby changing the deposited dose. Second, muscular contractions may cause the target and other relevant anatomical structures to move within, and possibly outside the treatment field. It is assumed here and throughout this thesis work that the changes in dosimetry due to respiration are primarily due to physical displacements as opposed to density variations. Under normal tidal breathing, the density variations within the lung are assumed to be not significant.

In this chapter, the extent of lung motion is quantified. This data is then used to model the potential dosimetric effects of margins specifically alloted for respiratory displacements. Gated radiotherapy is investigated as an alternate form of therapy to account for respiratory displacements.

6.1 Physical Displacements of Lung due to Respiration

To obtain a better understanding of the degree and extent of lung motion, an MRI[5] image was taken of myself during forced exhalation, inspiration, and normal tidal breathing. Several scans were taken; most of which were in the sagittal plane. At 256 x 256 pixel resolution, acquisition of a sagittal slice took slightly less than 9 s. Images were acquired during breath hold at inhalation and exhalation. The hardcopy film images were read with a Vision 10, V-Scan film scanner[6] for digitisation. Figures 6.1 display sagittal sections at inhalation and exhalation.

A subroutine was written in the Matlab environment to read in the digitised image and compute the "signature" of the lung. A signature is a one dimensional function that plots the radius of an object as a function of angle. Signatures are useful functions that can illustrate the relative displacements of objects with respect to a fixed point. They are invariant to translation but dependent on rotation and scaling. Since the original MRI images did not contain calibration distances, the signature would correspond to relative changes in distance with respect to some fixed coordinate. The central point selected for this initial trial was located close to the first bifurcation within the lung. This point was chosen since it does not move significantly during respiration.

---

5 Phillips Gyroscan
6 Vision Ten Inc. Carlstadt. NJ
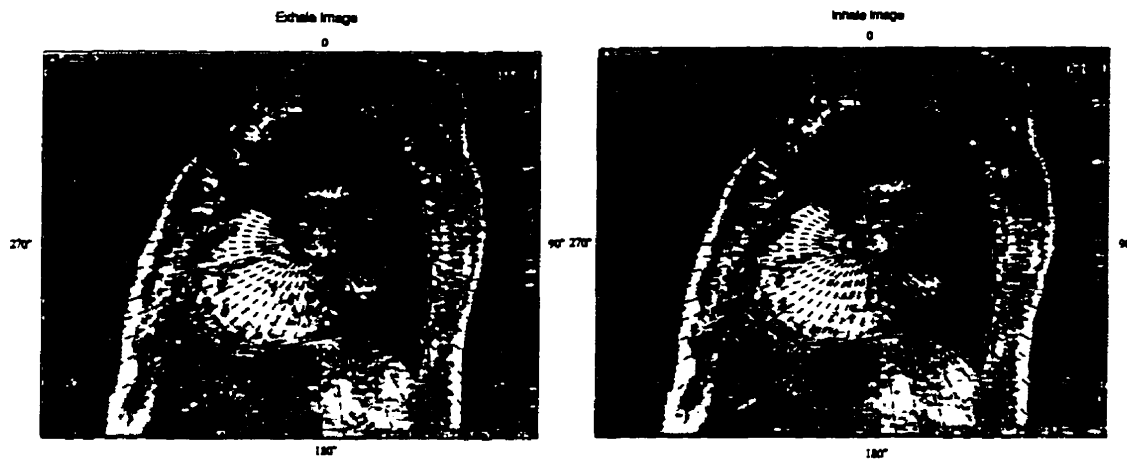
Figure 6.1: Sagittal sections of the thorax at exhalation (left) and inhalation (right).

To implement the subroutine, the image was displayed on a computer screen and a mouse was used to outline the contour of the lung in the image. Then, a central point was defined within the lung contour and the two dimensional contour was sampled at regular angles in a clockwise direction, starting from the apex of the lung. For data points lying between the sample points, an angularly weighted interpolation was carried out (See Figure 6.2). Figure 6.1 illustrates the sampling of the lung's contour discretised into 64 sectors.
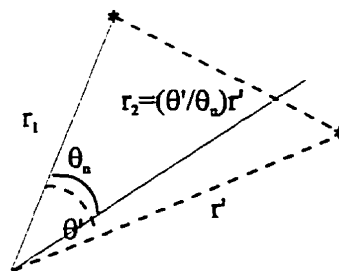
Figure 6.2: Interpolation of radius for randomly sampled data points. The two stars indicate contour points entered with the mouse. For a regularly sampled signature with angular intervals of θ_n, r_2 is an interpolated average.

A data plot of displacements with respect to angle could be plotted to determine the regions within the lung that exhibited the greatest amount of motion. The signatures at inhale and exhale are plotted in Figure 6.3. Rotating in a clockwise sense and designating the superior direction as $0°$, the figure illustrates that motion with respect to the bifurcation point appears to be the greatest from from $114°$ to $200°$. This is essentially where the diaphragm resides. Also, minor deviations are observed in regions where the chest wall resides ($230°$ to $315°$). As expected, the posterior portion of the lung exhibited little relative displacements.

Since the image was acquired in the supine position, the back of the lung appears to remains stationary.

The results of these measurements indicate that the greatest extent of motion within the lung is clearly due to the diaphragm and not the chest wall. Little or no motion can be expected at the apex and the posterior portion of the lung. This is expected for healthy patients as indicated in the literature.

There is little data in the literature regarding lung displacements due to respiration for those who have respiratory problems or lung cancer [Baltar et al. 1996, Ross et al. 1990, Willet et al. 1987]. To better understand the margins of error involved due to respiration for typical patients at the Cross Cancer Institute, measurements of diaphragmatic and rib cage displacements were measured from lung cancer patients undergoing normal fluoroscopy sessions. Measuring the extent and range of motion for the lung tumours themselves is much more a formidable task since the motion will depend on a host of patient and disease specific information. This would require a large sample of patients with similar diagnosis, which is unavailable to date.
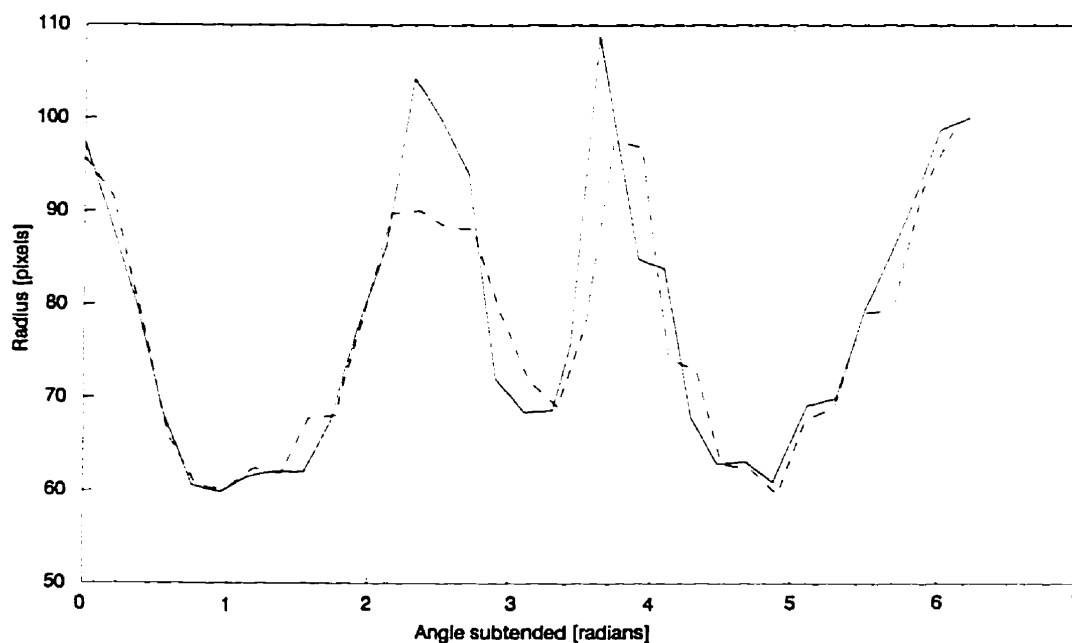
Figure 6.3: Signature of exhale and inhale contours, taken in 64 radial intervals, from the apex of the lung clockwise.

6.1.1 Methods and Materials

Measuring the motion of the diaphragm and chest wall is often much easier than measuring the motion of tumour volumes. This data may provide more reasonalby expected ranges of motion for lung cancer targets and may aid in defining planning target volumes for tumours attached to the diaphragm or chest wall.

Lung cancer patients undergoing fluoroscopic examination with a simulator[7] were videotaped. The video output of the fluoroscopic video feed was split to a television monitor and to a video tape recorder. The fluoroscopic sessions were videotaped at the lowest speed setting (LP) for the best resolution. After the images were videotaped, the images were retrieved by using super VHS videotape playback and pausing images during the respiratory cycle. Frame by frame, the greatest extent of displacements was observed and a frame grabber board[8] was used to capture the still images. The frame grabber board was configured to grab 640 x 480 pixel images. The highest resolution achievable is 1500 x 1125 pixels, however, the additional information yields little and data storage becomes unnecessarily large. The frame grabber board samples the images several times before producing the final image. This allows for a higher signal to noise ratio (SNR) and thus more clear images. Generally, the grabbed images have better contrast resolution than the videotaped images because of the lower SNR. The highest sampling frequency is 12.5 MHz, and each frame is sampled in 1/60 s. There are also several control features in the software that control the brightness, color, contrast, sharpness, tint, and picture. These were all set to their default values to ensure the images were original and untampered. The aspect ratio was kept constant throughout all of the analysis of the images to ensure that pixels were square and that real distances could be measured in both directions.

By recording the magnification factor and source to detector distance for each projection, it was possible to calculate actual displacements:

$$d\,[cm] = MF \cdot \left(\# \, pixels \cdot \frac{cm}{pixel} \right).$$

MF is the geometric magnification factor, which is the source to detector distance over the source to object distance. The cm/pixel ratio is determined through a calibration for a magnification factor for a known field size. Since all images were in a 640 x 480 pixel format, the MF and the cm/pixel values were computed once for all the geometric arrangements.

Before measurements were made, the rows of the image were checked to be horizontal. This was done by manually drawing a line from left to right on the image and comparing it with the cross-hairs of the simulator. Some of the images were distorted, displaying pin-cushion like distortion. These effects were less than 0.1 cm and were neglected. Since consecutive inhale-exhale images often had the same distortion, the resultant effects of this distortion are assumed to be negligible (See Figure 6.4 for an example of this distortion).

Measurements on each image were made with respect to a landmark. The selection of this landmark is arbitrary and not important as long as the exhale-inhale displacements are made with respect to the same landmark. Because consecutively grabbed images would sometimes be offset by several rows or columns, the landmarks were defined to be common points on each image. The bullseye, or the intersection of the cross-hairs aligned at the center

7 Phillips 80CP Universal Therapy Simulator
8 Snappy Video Snapshot, Play Inc. CA

of the tumour volumes, was used because it normally remained in the same position between the two images. When the bullseye could not be used, a vertebra was used since the spine remains relatively motionless during respiration in the supine position. The coordinate system defined here is a "relative" one where the absolute displacements were measured, i.e., no negative displacements were measured. All measurements were made within the Matlab environment.
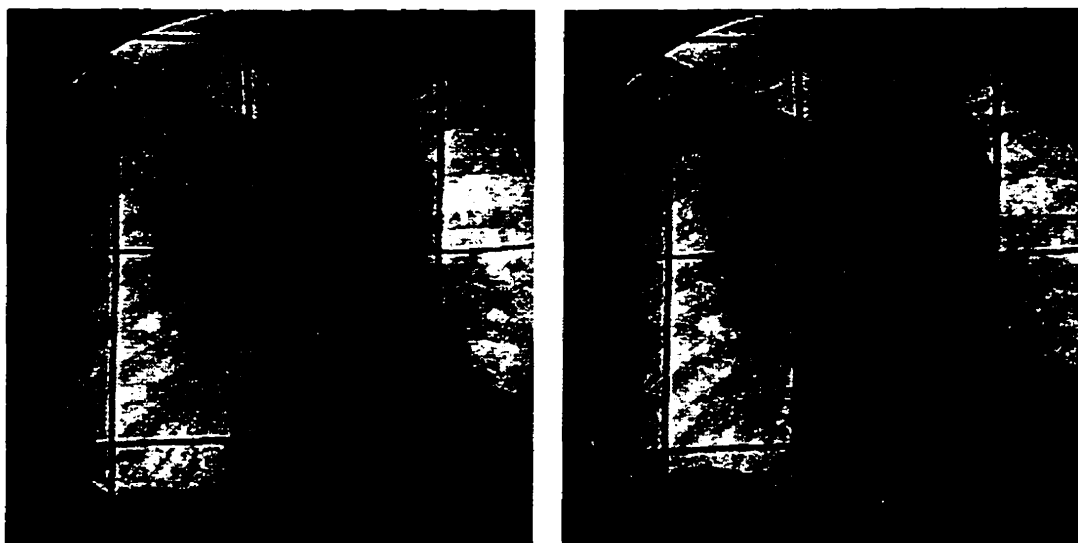
Figure 6.4: Typical images of displacements for the motion study. The image on the left shows the lung volume at inhalation while the right is shown at exhalation. The horizontal cross-hairs within the field of view show the displacement of the diaphragm in the sup-inf direction. Also shown is the minor distortion observed on all captured images.

In total, 10 patients with fluoroscopy of the lung were videotaped. Of these 10, only 7 patients had fluoroscopic sessions that could allow for proper quantitative analysis. All of these patients had an adequate number of AP views available for capturing. Of the 7 patients, only one lateral view was obtainable. The lateral measurement was recorded but not represented in the full summary of the data. Lateral chest wall excursions could be measured from the AP views and are included here in the analysis.

Both left and right diaphragm dome displacements in the superior-inferior direction were measured when possible. Likewise, lateral displacements of the chest wall were measured in both directions when possible. Points exhibiting the largest displacements observed for both the diaphragm and chest walls within the field of view were measured and recorded.

Also, respiratory frequencies were recorded for the 7 patients. The frequencies, determined as the rate at which the diaphragm increases and decreases in height, were measured with a stopwatch. The respiratory periods of each patient were recorded along with their standard deviation.

Lastly, a temporal measurement of displacements was also taken for one patient. This was done for patient whose field of view clearly showed the fullest extent of the diaphragm in the respiratory cycle. Since the diaphragm is the largest moving organ in the lungs, measurements of superior-inferior displacements were made for the height of the diaphragm with respect to a stationary point. This was done by capturing consecutive images in intervals as short as the VCR would allow. A point on the diaphragm could then be traced out for each image to generate a displacement with respect to time.

No efforts were made to selectively "weed out" large scale displacements caused by sighs, yawning, or other normal bodily functions. Although this may skew the results to potentially larger values, it reflectives the actual displacements observed during the treatment.

6.1.2 Results

Each of the 7 patients videotaped showed various degrees of respiratory motion. Generally, it was observed that the degree of target motion was a function of tumour position within the lung, size of the tumour, and other individual case specific factors.

For the one patient whose lateral field could be measured, 12 pairs of exhale and inhale images were captured. Displacements of the left lung diaphragm were measured at 8 mm with a standard deviation of 2 mm. That is, the average uncertainty in one measurement would be ± 2 mm, 63% of the time, and ± 4 mm, 95% of the time. The best estimate of the average displacement, d, is equal to,

$$\delta d = \frac{\sigma_{\bar{x}}}{\sqrt{N}},$$

or 1 mm, which gives a best estimate of 9 ± 1 mm. The dorso-ventral displacement of the left chest wall was measured as 3 mm with a standard deviation of 2 mm, or a average displacement of 3 ± 1 mm.

For the AP views, the relative tumour positions, field sizes for each patient, and the number of images acquired for each view and lungs are summarised in Table 6.1.

Patient	Tumor Position	Field Size X x Y [cm]	AP: SI Left	AP: LA Left	AP: SI Right	AP: LA Right
P0002	L Mediastinum	14.6 x 16.0	24	-	14	13
P0006	R Upper Lung	19.2 x 14.4	-	-	6	14
P0007	L Upper Lung	11.9 x 15.0	7	7	-	-
P0008	C Mediastinum	18.4 x 14.4	9	9	9	9
P0010	C Mediastinum	16.0 x 13.3	13	13	7	-
P0011	R Mediastinum	13.0 x 11.5	7	-	7	7
P0012	L Mediastinum	15.1 x 12.0	13	13	13	-

(Column header span: "Number of Images Acquired" covers AP: SI Left, AP: LA Left, AP: SI Right, AP: LA Right)

Table 6.1: Summary of patient data. SI refers to superior-inferior displacements of the diaphragm and LA refers to the lateral displacements of the chest wall.

The AP field sizes for the patients were very large, being on average 15 x 14 cm^2, and the locations of the tumours were situated, on average, in the mediastinum. The results of the measured displacements are summarised in Table 6.2.

Patient Number	Left Diaphragm [mm] x (σ)	Right Diaphragm [mm] x (σ)	Left Lateral Chest Wall [mm] x (σ)	Right Lateral Chest Wall [mm] x (σ)
P0002	10 (9)	31 (26)	-	4 (3)
P0006	-	19 (10)	-	2 (2)
P0007	15 (11)	-	2 (1)	-
P0010	7 (4)	11 (7)	1 (1)	-
P0011	19 (3)	39 (5)	-	7 (6)
P0012	12 (2)	31 (3)	2 (2)	-
MEAN	**13 (5)**	**26 (11)**	**2 (1)**	**4 (2)**

Table 6.2: Results of motion displacements as measured from fluoroscopy sessions. All measurements are in millimetres.

The diaphragm contributed the largest displacement, from 13 to 26 mm, as seen in the anterior-posterior projections. Less significant is the lateral motion of the chest wall, which was measured at 2 to 4 mm. The largest displacement observed for either the left and right diaphragm was 48 mm. The largest displacement observed for the lateral displacements for either the left or right chest wall was 10 mm.

Tumours situated close to functional diaphragms displayed greater ranges of motion than those tumours situated superior to the diaphragm. Tumours situated in the mediastinum area displayed smaller ranges of motion than those tumours situated lateral to the mediastinum. Obviously, the closer the tumour was situated to a functional respiratory muscle, the more prone it was to displacement subject to that muscular contraction.

Larger tumours, possibly due to their inertia, moved less whereas smaller tumours showed larger displacements. The larger tumours most often lay in the mediastinal region, which was found to be less mobile. Tumour extensions were observed to "anchor" themselves to various portions of the lung and mediastinum. These extensions added complexity to the tumour dynamics.

In some instances, a few of the respiratory muscles were dysfunctional or completely collapsed. This required the functional respiratory muscles to compensate for the lack of pleural pressure necessary for inducing an adequate expansion of lung volume for oxygenation. Therefore, the patterns of respiratory displacements were unique for every patient observed. In some instances, functional portions of the diaphragm were observed to displace up to 48 mm, whereas nonfunctional portions of the diaphragm remained flaccid.

The respiratory frequencies of the patients are displayed in Table 6.3. The average respiratory period was 3.2 seconds with the lowest and highest being 2.4 and 4.0 seconds, respectively. Large deviations were not observed in the respiratory periods. The effects of sighs, deep breaths and other normal physiologic behaviours were not rejected when computing the averages. We assume that these small deviations are random and eventually average out when the number of samples become large. There are no obvious correlations between respiratory period and displacements of the lung.

Patient	Respiratory Period [s]
P0002	2.5
P0007	2.4
P0008	3.5
P0009	3.5
P0010	2.9
P0011	3.7
P0012	4.0
Mean	**3.2 (0.6)**

Table 6.3: Respiratory periods for the various patients.

A temporal displacement pattern of the right diaphragm was recorded for patient P0002. The pattern is displayed in Figure 6.5. The peaks show when the diaphragm was contracting, in the inferior direction, and the "valleys" indicate the end exhalation phase. Only 6 cycles were recorded; digitizing the trace required more than 200 samples of images and was, therefore, a time consuming process. Measurements of displacement were recorded with respect to the initial position so at to observe the minor shifts in the end exhale position. Figure 6.5 illustrates the migration of end exhalation return positions with an almost equal maximum inhale displacement increases. A sinusoidal pattern is also illustrated to show the differences between the two displacement schemes.

A useful indicator of the likely position of the target is the time averaged position of the displacement pattern. This is computed as,

$$\hat{x} = \frac{\int_0^{t_f} x(t)dt}{\int_0^{t_f} dt} ,$$

and it describes the mean position of the object over the full length of time. For the sinusoidal pattern, the time averaged position is simply the mid point of the total displacement, which is 1.6 cm. The time averaged position of the realistic pattern is 1.1 cm, which significantly less than the sinusoidally time averaged position. It is reasonable to assume that the time average position of a target undergoing respiratory motion is less than half the distance of the largest displacement. In fact, for many of the other patients observed, respiratory patterns are more like a "spike" at inhalation with longer periods of no displacement during the end exhalation phase. The shape of the temporal distribution will greatly affect the time averaged position of the target.
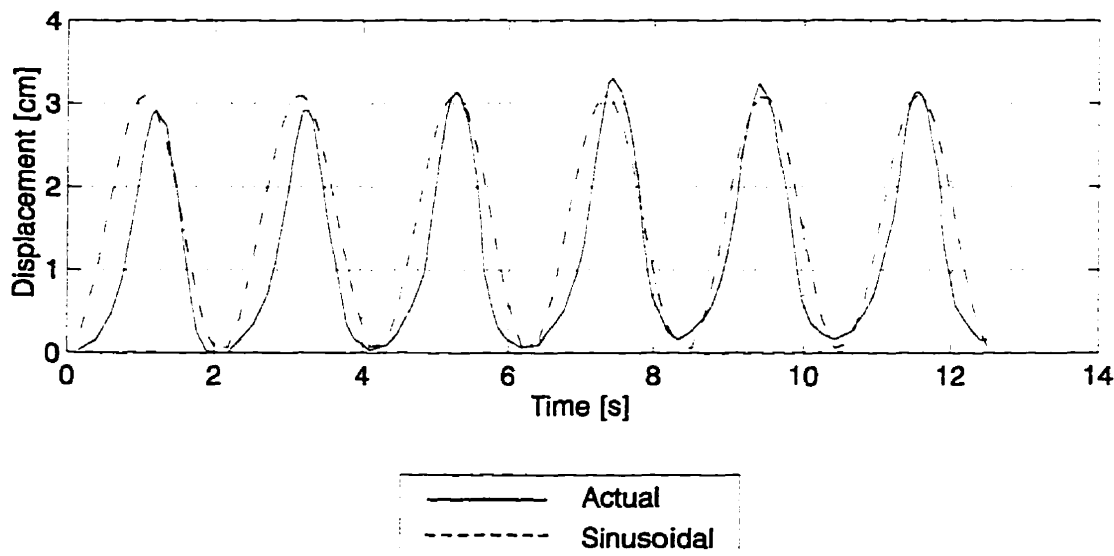
Figure 6.5: Temporal tracing of diaphragm displacement with respect to time for patient P0002. The solid line illustrates the real displacement and the hatched line shows a sinusoid for comparison.

Clearly, the temporal trace measured here is not a reflective description of average temporal displacements one may expect for a typical lung cancer patient. However, the tracing does provide some information with respect to the degree of motion and may serve as a useful starting point for future investigations.

6.1.3 Discussion

The intent of this study was to investigate the ranges of displacements of lung due to respiration for a typical lung cancer patient at the Cross Cancer Institute. From the videotaped data, it has been observed that the ranges of motion for typical lung cancer patients vary significantly among patients and disease locations.

It has been shown here that margins for the MTV, or Mobile Target Volume, may be as great as 26 mm in the superior-inferior direction, and up to 4 mm in the lateral direction for tumours attached to the diaphragm or the chest wall. It is probable that displacements of tumours situated within the boundaries of the chest wall and diaphragm may also be as large as the displacements of the chest wall and diaphragm themselves, if not greater.

Our data of diaphragmatic displacements provide slightly larger results than other published results of healthy patients [Davies et al. 1994, Korin et al. 1990]. This could be due to the fact that many of the patients imaged were elderly and exerted more physical effort than healthy subjects while breathing. Since a significant number of the patient lungs were not functional, more effort is necessary to oxygenate the lungs. Therefore, it is understandable that the displacements would be larger than those found in healthy patients.

With respect to tumour motion, the range and extent of motion appear to depend on several factors that include position of tumour within lung volume, size of tumour, and other patient specific factors, such as the functionality of respiratory muscles. Due to patient

specific clinicalities and the minimal data accrued, it is difficult to quantitate the displacements of tumour volumes from the fluoroscopic sessions. It has been suggested that correlational studies may prove useful in obtaining some context and insight into the extent of motion for variable such as disease types, target position within thorax, patient age and other factors [Moerland et al. 1994]. If the lung is healthy, one can assume that the lung parenchyma is homogeneous and isotropic [Tai et al. 1981]. Under this assumption, the lung would behave pseudoelastically. Thus, the motion of a volume of lung, regardless of its mass, may be assumed to displace linearly from the end-exhalation point within the lung volume. Ross et al. (1987) found little or no motion of tumours in the apex of the lung. Since patients are in the supine position, motion of the chest wall is predominantly in the anteroposterior direction [Jacobs et al. 1996]. However, the presence of micro-extensions makes the range of motion more complicated than an interpolation of displacements of the chest wall and diaphragm boundaries.

Although correlational studies may provide helpful information when assessing the margins of the PTV, it is essential to assess each patient individually so that an adequate determination of the PTV can be made. When using the beam's eye view approach to radiotherapy planning, as often done in 3D-CRT, it becomes important to account for respiratory displacements accurately.

6.2 Dosimetric Consequences of Respiratory Motion

The MTV margin includes healthy tissue; it is the margin necessary to ensure that the CTV is completely irradiated. A major advantage of 3D-CRT is that smaller PTVs can be delivered, thereby reducing the amount of healthy tissue irradiated. Measurements have been taken at the Cross Cancer Institute regarding the extent of respiration motion. Given the potential values of displacement margins, a reasonable question one may ask is whether there is a clinical advantage of reducing the MTV by margins allotted for respiration.

Ten Haken et al. (1993) propose a dose escalation protocol where tumour doses may be increased according to their effective volumes. The technique requires that the dose limiting organ be specified and iso-NTCP curves be generated, much like those illustrated in Figure 3.7. Then, effective volumes are binned and a prescription dose is selected. This allows for the possibility of separating those effects that may arise from the volume of tissue irradiated and those effects that are due to the dose given. The effective volume method amalgamates all the three dimensional dose information into a single number that relates the partial volume of healthy tissue irradiated at a level equal to the prescription dose. Within the NTCP model outlined here, the complications of normal tissues with small volume effects are more sensitive to dose than to volume. At high doses (>70 Gy) tissues with larger volume effects, such as the lung and liver, may be more sensitive to volume than dose [Armstrong et al. 1993]. This may be illustrated through the small slopes of the NTCP curves at higher doses. For marginal changes in effective volumes, larger dose widths are spanned. By selecting effective volume bins, one can define prescription doses that do not exceed a specified complication.

The Radiotherapy Therapy Oncology Group (RTOG) have devised such a protocol for NSCLC Stage I-IIIB tumours [RTOG 93-11, 1995]. In this protocol, a dose escalation protocol is binned according to the fraction of volume receiving a dose greater than or equal to 20 Gy. Shown in Table 6.4 is the protocol.

% Lung recieving dose greater than 20 Gy	Dose Levels Gray (Gy)			
< 25%	70.9	77.4	83.8	90.3
25% < V_{lung} < 37%	70.9	77.8	83.8	
> 37%	64.5	70.9	77.4	

Table 6.4: RTOG 93-11 NSCLC dose escalation study.

Outlined in the protocol, Graham et al. (1996) have found that stratifying the prescription doses according to percentage volume of lung receiving 20 Gy or greater is almost as good as stratifying the doses according to the effective volume method. This data is much simpler to compute and thus helps ensure consistency among institutes. The percentage of lung dose exceeding 20 Gy may be obtained by the cumulative dose volume histograms.

6.2.1 A CT Case Study

There have been several reports in the literature where the MTV is minimised by turning on the beam during portions of the respiratory gate [Huang et al. 1996, Kubo et al. 1996, Ohara et al. 1989]. Kubo et al. have modified a linear accelerator such that the radiation is delivered in pulses that can be synchronised with the respiratory gate. Given that the technology is possible, it is worthwhile to consider the dosimetric consequences of allotting various MTVs in a treatment plan. This simulation attempts to examine whether there is an advantage to minimizing the margins allotted for respiration in the MTV. In light of the RTOG 93-11 NSCLC protocol, the effects of reducing the beam width by various PTV margins are examined.

6.2.2 Methods and Materials

A full thoracic treatment CT data set of a patient was obtained from the patient archives at the Cross Cancer Institute. The data set included 41 slices at 0.5 cm intervals. A spherical object was drawn in the right lung to mimic a tumour volume. The radius of the spherical tumours was varied from 1.5 cm to 3.0 cm, in 0.5 cm intervals, and a 3D treatment plan for the CT phantom was then devised on Helax TMS. The 3D treatment planning optimization was facilitated through inhomogeneity compensation and gradient vector approach, described in Chapter 5. Helax TMS employs a differential pencil beam algorithm for dose computation where the inhomogeneity correction is done through adjusting scatter constribution through a correction factor, based on the effective pathlength (See Section 3.2.2.3 for a description of the algorithm). Helax TMS also contains an algorithm for beam optimisation where a plane perpendicular to the beams axis can be defined and a modulation matrix is generated to establish the uniform dose at depth, similar to those created for the 2D case in Section 5.2. The optimisation accounts for surface inhomogeneities as well as internal inhomogeneities, in 2 dimensions. The accuracy of the optimisation routine is still under investigation. Knöös et al. (1995) have shown the dose calculation algorithm to be in error by 3% for 4 MV photons and upto 14% for 18 MV photons . The inhomogeneity algorithm has been measured to produce results comparable to the ETAR and Batho algorithms in the 2D-ATP algorithms.

To simulate the dosimetric effects of variable MTV margins, the beams used in the planning were increased to margins that could be expected for respiratory displacements (See

Figure 6.6). While fixing the collimator angle, the X jaw settings were varied from 0 to ±1.0 cm in 0.25 cm intervals to account for these movements of the tumour volume. The Y jaw settings were also varied from 0 to ±1.0 cm to account for lateral displacements, and also increased to ±2.0 cm to account for superior-inferior displacements. The values of 1.0 cm and 2.0 cm for the lateral and sup-inf displacements were used based on the results of the measured data in Section 6.1.2. In total, 36 dose computations, at a resolution of 0.25 cm, were performed. On average, dose computation for one plan required less than 30 minutes, depending on the number of clinical cases the system was currently handling.

Helax TMS has a subroutine that calculates dose volume histograms for volumes of interest. The dose volume histograms of the target volume and the lung were computed and later analysed to assess potential biological risks for the additional PTV margins. The dose resolution for the calculations was kept to a minimum to ensure that not only the dose distributions were accurate, but the dose volume histograms were accurate. The dose volume histograms were normally binned in dose levels of 1% of the prescription dose.
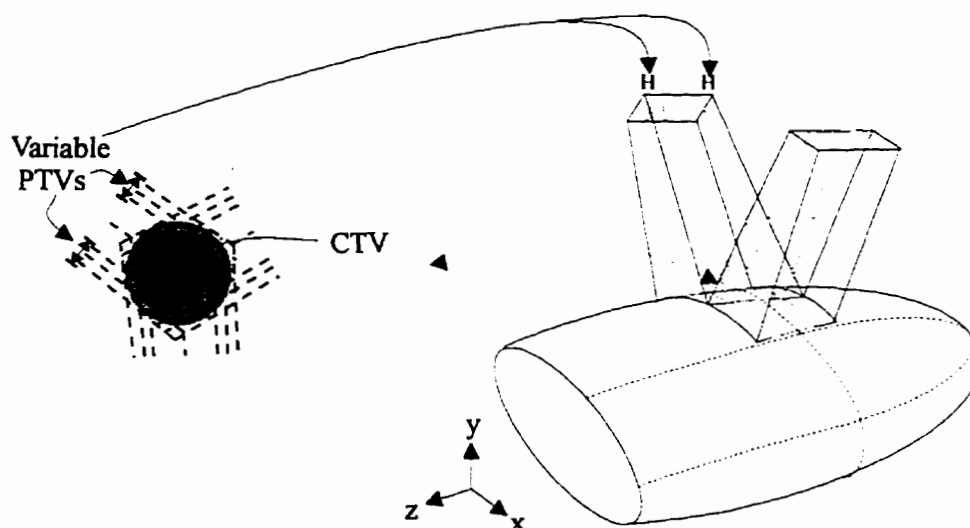
Figure 6.6: Schematic of PTV allotments. Margins in the x-y plane ranged from 0 to 1.0 cm where margins in the z direction ranged from 0 to 2 cm. The third beam, posterior to the anatomy, is not shown.

After the dose volume histograms were calculated, they were exported from the Helax environment to a PC for analysis. A subroutine was written in the Matlab environment that reads in the dose volume histogram, converts it to a differential dose volume histogram, and performs an effective volume computation. The equations used to compute the effective volumes are described in Section 3.3.2. For example, Figure 3.6 illustrates the differential dose volume histogram for the 3.5 cm radius target with lateral and anteroposterior margins of 1.0 cm and 2.0 cm, respectively. The differential dose volume histogram displays the dose per volume in dose bins spaced 1 Gy apart. Referring to Figure 3.9 and Equation 3.2, approximately 50 cm^3 of the lung receives 100% of the prescription dose. ΔV_i in this case is

computed at 50 cm^3 / 3263 cm^3 or 0.015. $(D_i/D_m)^{1/n}$ for this case becomes $(100/100)^{1/0.87}$, which is 1. Thus, the contribution of the maximum dose to the effective volume becomes 1 x 0.015, or 0.015. Another computation of effective dose is carried out for the next dose bin and the process is repeated until all dose bins with their corresponding irradiated volumes are processed. The individual effective volume values are summed to produce the effective volume of the lung, which in this example, is 0.26. The effective volume can now be inserted into the complication probability model described in Section 3.3.1. Using Equations 3.2c, the parameter v=0.26, $TD_{50}(1)$=24.5 Gy and n=0.87 (from Emami's data), we obtain $TD_{50}(v)$=79.1 Gy. Inserting this value into Equation 3.2b and with m=0.18 allowing the dose values to vary from 0 to 120, we obtain t as a function of dose. The function t can then be inserted into 3.2a to produce NTCP values as a function of dose. The curve in Figure 6.7 displays the outputs of Equation 3.2a with dose values ranging from 0 to 120 Gy.
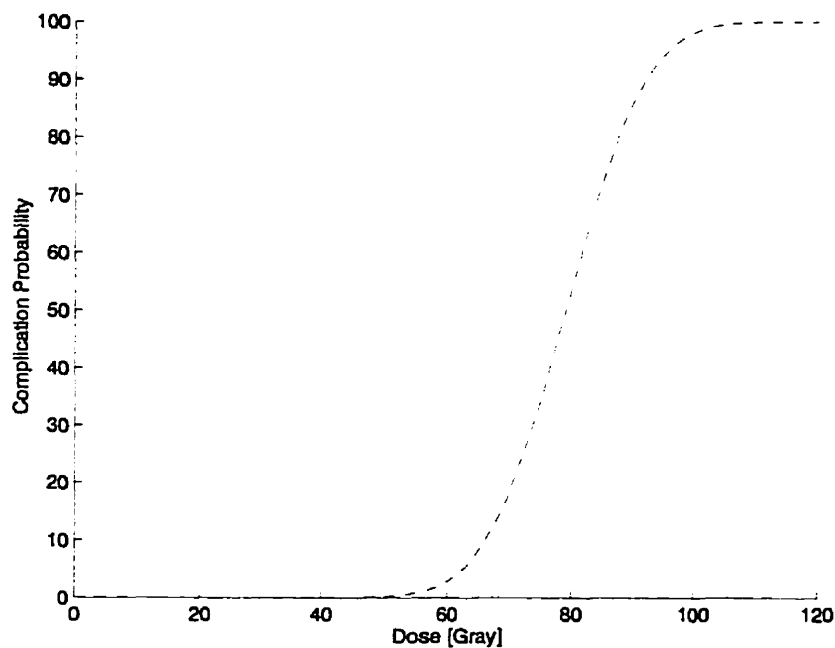
Figure 6.7: Generation of NTCP curve for the differntial dose volume histogram illustrated in Figure 3.9. The effective volume is 0.26, and parameters n and m are 0.87 and 0.18, respectively.

In addition to constructing the normal tissue complication probability curves for the various margins, the dose volume histograms were also used to compute the volume of lung receiving 20 Gy or more for various dose levels. The results were then compared to the current RTOG 93-11 protocol.

6.2.3 Results

Shown in Table 6.5 is the beam configuration along with other treatment planning parameters generated through the gradient vector approach. The treatment plan is illustrated in Figure 1.1 for the 1.5 cm radius target. 6 MV photons were used in the treatment plan, combined with compensators that optimise the dose at the target depth.

Beam Parameters	Beam 1	Beam 2	Beam 3
Gantry Angle	24	163	278
Beam Weighting	0.33	0.33	0.33
SSD (cm)	92.1	88.9	93.4

Table 6.5: Treatment planning parameters. SSD refers to the source to surface distance of each beam. No wedges were used in this (isocentric) plan.

The resulting dose distributions may be summarised through the dose volume histograms for the various volumes of interest. In this simulation, the critical volume of interest is the lung, since it is quite susceptible to radiation damage, or pneumonitis. Figure 6.8 illustrates the dose volume histograms for the target whose radius was 1.5 cm. The three lines on the DVH display the amount of dose the lung receives when the margins are 0, 1.0 cm laterally and anteroposteriorly, and 1.0 cm laterally and 2.0 cm superior-inferiorly. The dose volume histograms for the other targets are also displayed in Figures 6.9 to 6.11. Significant shifts in the dose volume histogram profiles are observed when the margins are increased by a 1.0 cm, both in the lateral and sup-inf direction. As the radius of the target increases, more lung tissue becomes irradiated.

The dose volume histograms were analysed to produce the corresponding effective volumes using the suggested Lyman four parameter model (Equation 3.2). The effective volumes are summarised in Figure 6.12.

As expected, the effective volumes increase as the PTV margins increase. Effective volumes as a function of PTV margins are relatively parallel with differing y-intercepts, or target volumes. The slopes of the 4 curves vary only slightly, with small slopes for the smaller target, and slightly higher slopes for the larger targets. Effective volumes for the four cases span 0.09, 0.11, 0.13, and 0.13 effective volume units for the 1.5, 2.0, 2.5, and 3.0 cm radii targets respectively.
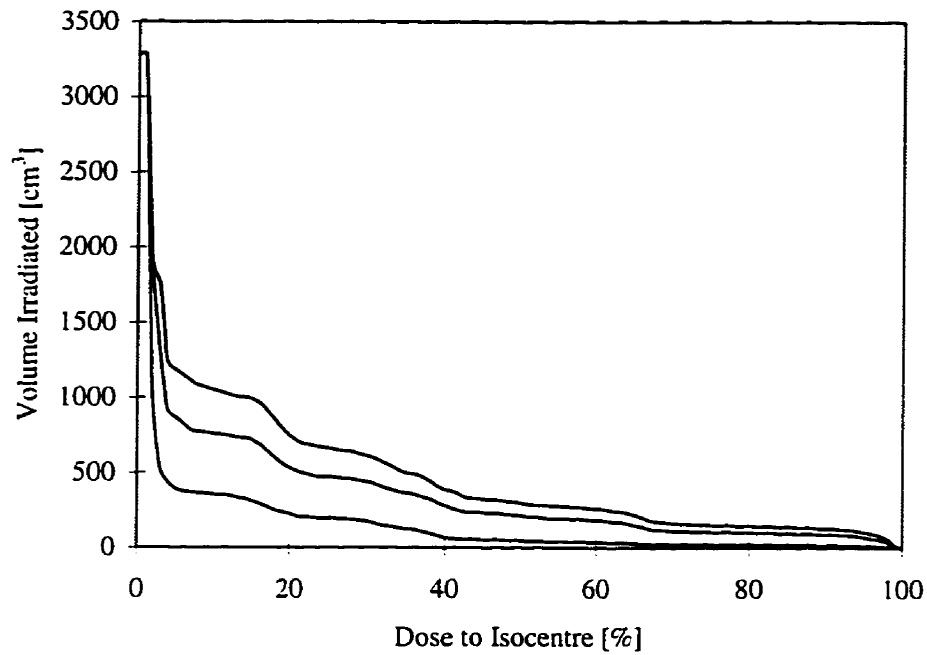
Figure 6.8: DVHs for Radius=1.5 cm. The PTV margins are 0 for the bottom, 1.0 cm in all directions for the middle, 1.0 cm laterally and 2.0 cm in the sup-inf for the highest lines.
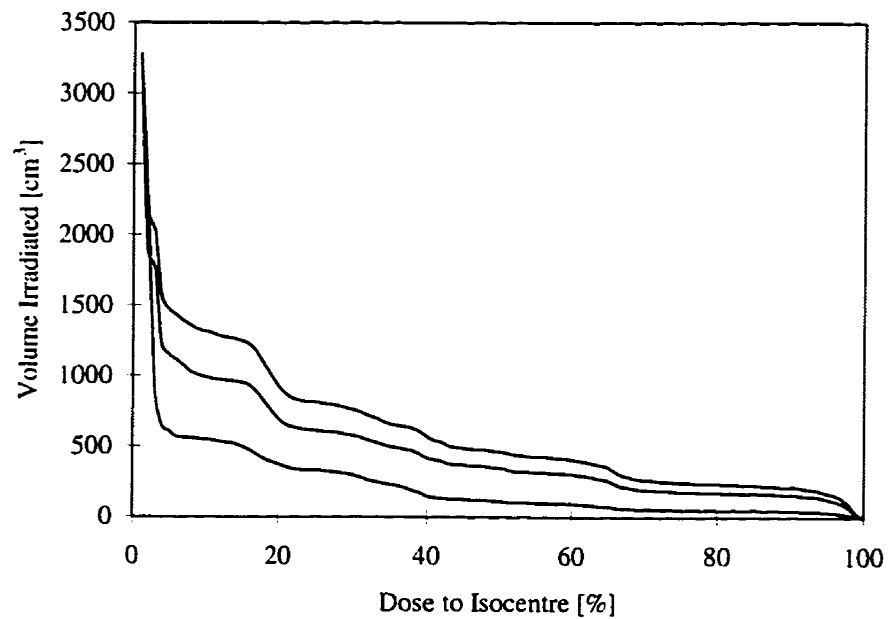
Figure 6.9: DVHs for Radius=2.0 cm. The PTV margins are 0 for the bottom, 1.0 cm in all directions for the middle, 1.0 cm laterally and 2.0 cm in the sup-inf for the highest lines.
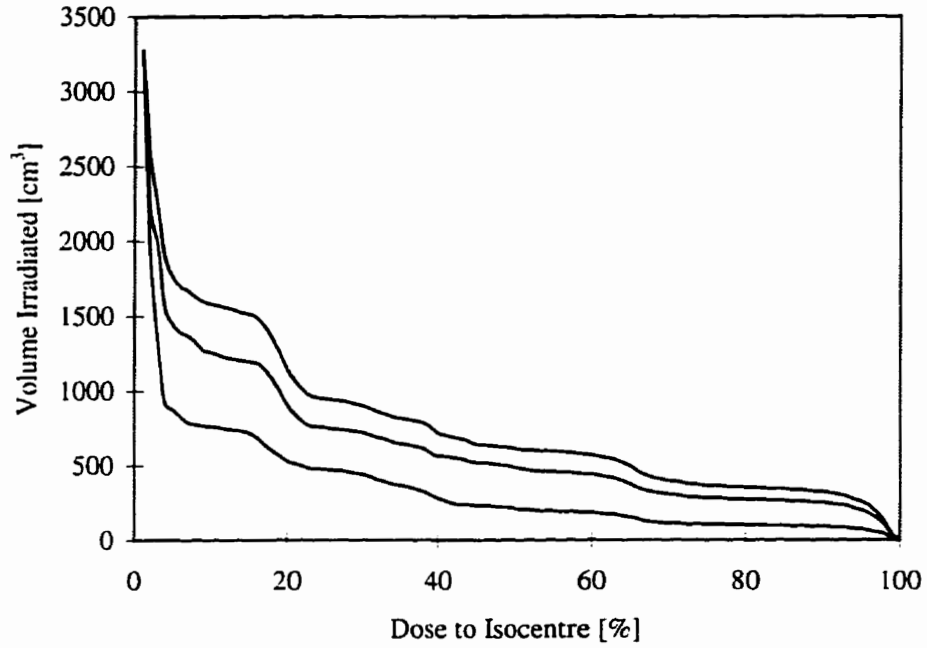
Figure 6.10: DVHs for Radius=2.5 cm. The PTV margins are 0 for the bottom, 1.0 cm in all directions for the middle, 1.0 cm laterally and 2.0 cm in the sup-inf for the highest lines.
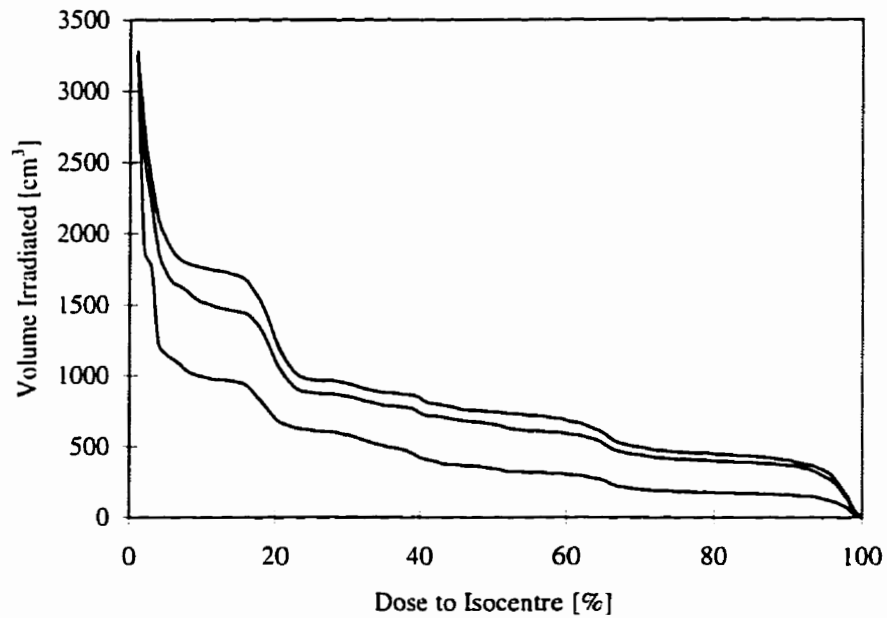
Figure 6.11: DVHs for Radius=3.0 cm. The PTV margins are 0 for the bottom, 1.0 cm in all directions for the middle, 1.0 cm laterally and 2.0 cm in the sup-inf for the highest lines.
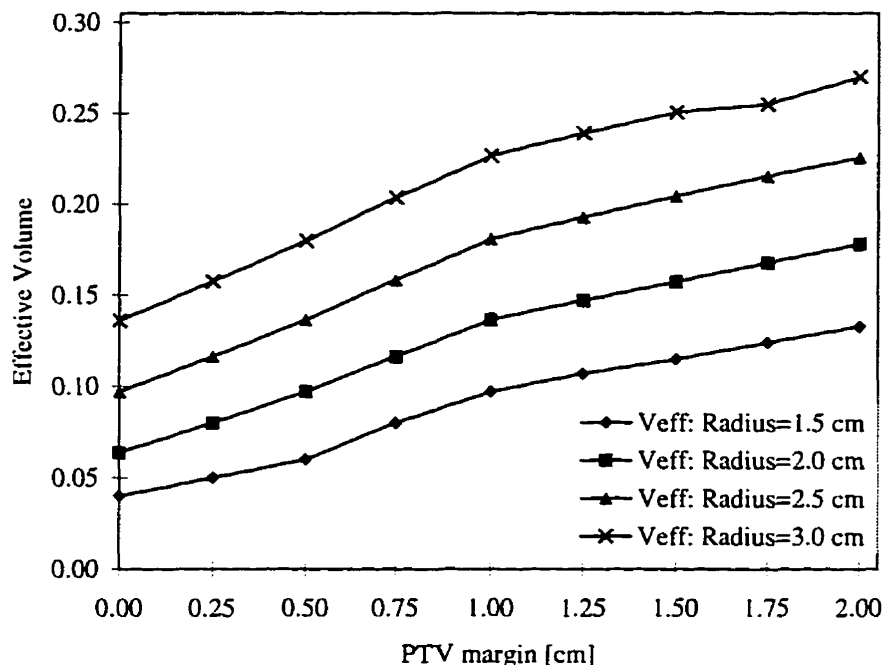
Figure 6.12: Effective volume computations.

Figure 6.12 illustrates that for this type of beam optimisation, the effective volume will increase proportionally with every PTV margin added to a clinical target volume. That is, for every 0.25 cm PTV margin used on a target with a radius of 1.5 cm to 3.0 cm, there will be an associated increase in the effective volume of approximately 0.015.

A three dimensional plot of lung tissue complication, effective volume, and dose on the z, y and x axes respectively, was generated to display the complication rates for various effective volumes and dose levels (See Figure 6.13). For reference, realistic prescription doses for NSCLC may be on the order of 60 Gy at the CCI. The regions of interest here are the lower effective volumes and the dose levels exceeding 50 Gy, along with their associated complication probabilities. Shown in Figure 6.14 are horizontal slices of the 3D plot for NTCP values of 5%, 10%, 30%, 50%, 90%, and 100% for reference. Also displayed on this graph are the effective volumes that the variable target radii straddle. The lighter lines indicate the effective volumes that are generated from no PTV margins where the darker lines indicate the largest PTV margins.

There are several things worth mentioning when inspecting this graph. First, assuming that the model is accurate, which has yet to be determined, there is potentially a greater risk from adding MTV respiratory margins for targets greater than 1.5 cm in radius. The Kutcher-Burman-Lyman model suggests that, when using our treatment planning optimization routine, targets smaller than 3.0 cm appear to have no associated complication probabilities, regardless of dose the target receives. This is due to the fact that the model predicts little changes in complications for effective volumes less than about 0.15. The model suggests that for a fixed

complication probability, there is a limit on the deliverable dose, as determined by the size of the PTV. The size of the PTV depends on the associated margins such as the MTV. According to this model, a change in the PTV by amounts equal to or less than 2.0 cm would reduce the risk of lung damage.
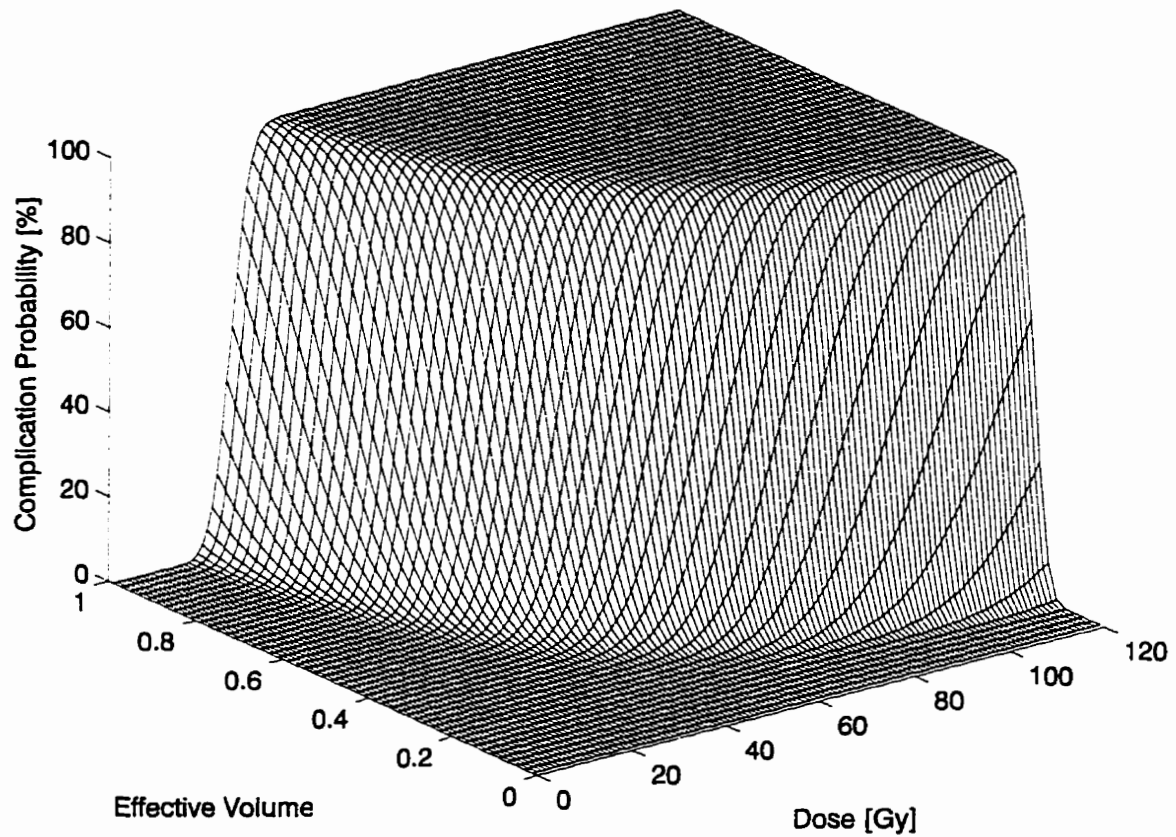
Figure 6.13: Three dimensional plot of complication for lung at various doses and effective volumes.
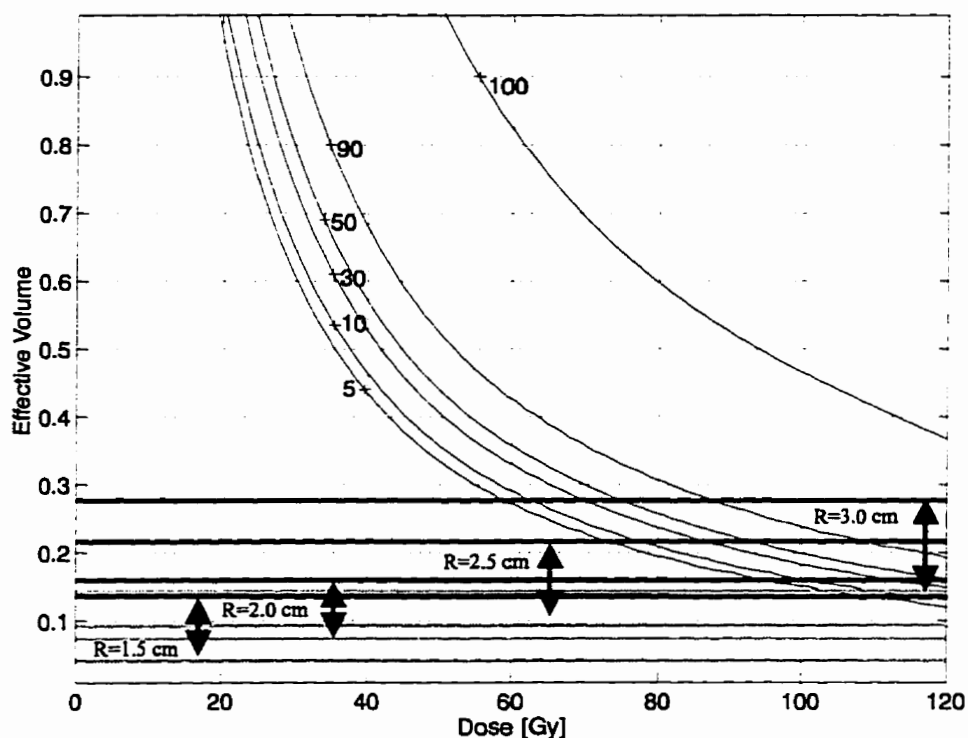
Figure 6.14: IsoNTCP curves for various effective volumes and doses. The lighter lines indicate effective volumes computed PTVs=0 cm where the darker lines indicate effective volumes computed for PTVs=2.0 cm.

If the margin allotted for respiration were reduced by 1.0 cm in the sup-inf direction, the treatment plans would consist of a 1.0 cm margin surrounding the PTV in all directions. The change in effective volumes from the 1.0 cm reduction of the sup-inf margins is constant for each target size. Although this margin seems small, being only 0.014, it is significant enough to produce different normal tissue complication probabilities within this model.

To compare with the RTOG 93-11 NSCLC protocol, Table 6.6 displays the percentage of lung volume greater than or equal to 20 Gy according to the various PTV margins for the various targets. The table illustrates that a 1.0 cm reduction in the sup-inf direction results in a significant change in the lung volume receiving equal to or greater than 20 Gy. Subsequently, such a reduction would result in the possibility of increasing dose from one dose level to a higher one. In particular, for either a 2.0, 2.5 or 3.0 cm target, if a prescription dose of 83.8 Gy were desired, a reduction of 1.0 cm would reduce the amount of lung tissue receiving greater than 20 Gy, which would be enough to allow for the potential of a higher dose of 90.3 Gy. A reduction of the PTV of margins allotted for respiration, in the case of the RTOG 93-11 protocol, would result in a higher tolerable dose limit.

	Radius=1.5 cm Sup-Inf Margin		Radius=2.0 cm Sup-Inf Margin		Radius=2.5 cm Sup-Inf Margin		Radius=3.0 cm Sup-Inf Margin	
Dose	1.0 cm	2.0 cm	1.0 cm	2.0 cm	1.0 cm	2.0 cm	1.0 cm	2.0 cm
70.9	14.0	19.6	18.3	24.2	22.6	28.4	26.6	29.4
77.4	14.5	20.3	18.7	25.0	23.1	29.0	26.9	29.6
83.8	14.8	20.9	19.2	25.3	23.5	29.7	27.6	30.8
90.3	15.2	21.2	19.6	25.8	24.2	30.8	28.9	32.3

Table 6.6: Percentage of lung volume receiving equal to or greater than 20 Gy for the various target radii and for various sup-inf PTV margins.

6.2.4 Discussion

This simulation attempted to examine whether there is a clinical advantage to minimizing the margins allotted for respiration in the MTV of lung cancer. When using the Kutcher-Burman-Lyman model for effective volume and normal tissue complication, there is a significant reduction in complication when minimizing margins allotted for respiration ($\pm$ 1.0 cm). The reduction of effective volume irradiated remained relatively constant for the four spherical tumours. This simulation suggests that dose escalation to the tumour may be possible if margins specifically allotted for respiratory motion were not included in the planning target volume.

The largest source of error in this simulation would stem from the Lyman model itself; it is uncertain whether this model is an accurate descriptor of complication rates for organs that have a large volume effect. An error map of the NTCP curves for the lung can be generated by performing an error analysis of Equations 3.2a-d and Equation 3.3.

The values of NTCP are highly sensitive to the curve fitting parameters n and m. Errors in these quantities have been derived by Burman et al. and are given as follows;

$$\delta n = \frac{1}{\ln(1/3)} \sqrt{\left(\frac{\delta TD_{50}(\frac{1}{3})}{TD_{50}(\frac{1}{3})}\right)^2 + \left(\frac{\delta TD_{50}(1)}{TD_{50}(1)}\right)^2} \text{, and}$$

$$\delta m = \frac{1}{1.647} \sqrt{\left(\frac{\delta TD_5(1)}{TD_5(1)}\right)^2 + \left(\frac{\delta TD_5(1)}{TD_5(1)}\right)^2 \cdot \left(\frac{\delta TD_{50}(1)}{TD_{50}(1)}\right)^2}.$$

The values of the error in TD_{50} and TD_5 are based on the differences between the calculated values within the model and that which was determined through the data of Emami et al. (1991). It may be true that the value of TD_{50} itself is in error; again, the model has yet to be verified. The model predicts $TD_{50}(1/3)$= 64 Gy, $TD_{50}(1)$= 25 Gy, and $TD_5(1)$= 17 Gy where Emami reports 65 Gy, 24.5 Gy, and 17.5 Gy, respectively. The errors in these values are very small, however, they have a significant impact on the computed NTCPs. The error in n becomes,

$$\delta n = \frac{1}{\ln(1/3)} \sqrt{\left(\frac{1}{65}\right)^2 + \left(\frac{0.5}{25}\right)^2} = \pm 0.02, \text{and}$$

$$\delta m = \frac{1}{1.647} \sqrt{\left(\frac{0.5}{17.5}\right)^2 + \left(\frac{0.5}{17.5}\right)^2 \cdot \left(\frac{0.5}{25}\right)^2} = \pm 0.02.$$

The upper and lower limits can be inserted into the NTCP calculation algorithm to produce a 3D surface similar to Figure 6.14 but with different values of n and m. Instead of showing the surface plots separately for each case, the absolute differences of NTCP values for the maximum and minimum n and m values were found and a contour plot of relative error in predicted probabilities is given in Figure 6.15. The horizontal solid lines in the contour plot indicate the effective volumes encountered in this simulation.
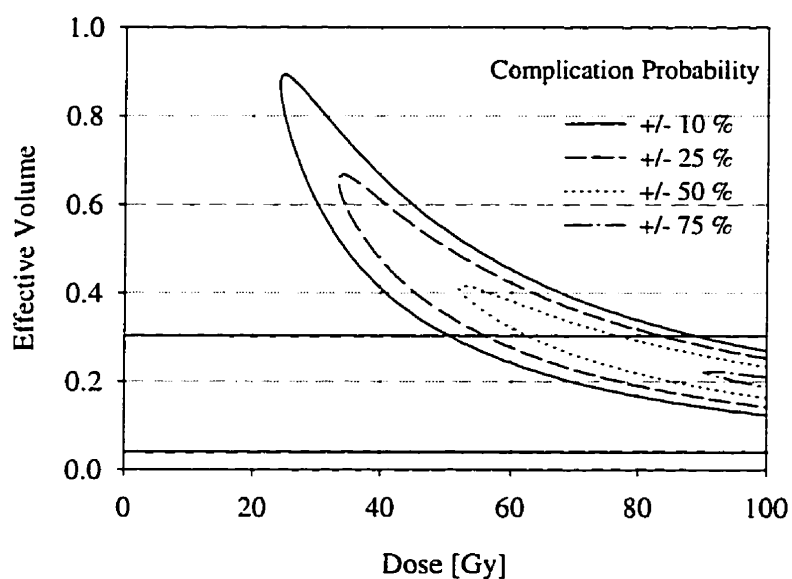
Figure 6.15: Errors in NTCP [+/-] for various effective volumes and doses. The horizontal solid lines indicate the ranges of effective volumes encountered in this simulation.

Figure 6.15, illustrates that the error is most significant for smaller effective volumes and high doses. Margins of error in complication rates can be expected to be ± 10-30%, depending on the prescription dose. These errors are large and may be greater because the values of TD_{50} and TD_5 are subject to further verification.

Despite the potential errors in complications, the *relative* placement of the complications is more important than the quantitative result itself. This in fact is the reason the dose escalation protocol is pursued; that is, for tissues with large volume effects, there potentially exist regions where overall dose response is more sensitive to the volume irradiated. By the same arguments put forth by the RTOG 93-11 protocol, a 1.0 cm reduction in dose would induce a change in effective volume equal to a significant change in tolerable prescription dose.

Other sources of error include the accuracy of the dose calculation and inhomogeneity correction algorithms. The errors in the calculation algorithm will effect the dose volume histograms and the subsequent effective volume computation. To estimate these errors, we start with

$$V_{eff} = \Delta V_i \left(\frac{D_i}{D_m} \right)^{1/n} .$$

Assuming that n, V and D are independent variables, the error in each of the bins may be given as,

$$\delta V_{eff} = V_{eff} \sqrt{ \left(\frac{\delta V_i}{V_i} \right)^2 + \left(\frac{\delta D_i}{n D_i} \right)^2 + \left(\frac{\delta n}{n^2} \right)^2 } \quad \text{(Equation 6.1)},$$

Note that no error in D_m is allotted, since all dose computations are done relative to some normalisation point. The normalisation point is arbitrary, therefore, it is excluded in the error propagation. δD_i approximates the error in the dose computation, δV approximates partial volume effects, and δn approximates errors in the lung volume dependence within the Lyman model.

Volume error for the CT data will depend on the pixel resolution and the size of the object of interest. The Helax algorithm computed the volume of the 1.5 cm radius sphere as 14 cm^3, which is less than 1% from the actual volume of $4/3\pi(1.5)^3$=14.1 cm^3. We previously stated that the error in dose is approximately 5% for the Helax algorithm. With n and δn equal to 0.18 and 0.02, the percent error in V_{eff} is less than 6%. Thus, each effective volume computation has an error of no greater than 6%. Clearly, the bulk of the error in V_{eff} stems from the accuracy of the dose calculation algorithm. This 6% error is not significant for effective volumes greater than 0.10, but may be of importance for effective volumes less than 0.10. However, for effective volumes equal to or less than 0.10, higher doses on the order of 100 Gy would appear to be tolerable. In such an instance, dose constraints would be minimal since so little of the healthy lung receives the prescription dose.

6.3 Accounting for Respiratory Motion

6.3.1 Diagnostic Imaging: Step and Shoot vs. Helical Scanning

As mentioned in Section 4.3.3, two things may be done to reduce the PTV margin allotted for respiratory motion. The first approach would be to treat the patient while asking the patient to hold their breath, and the other approach is to electronically gate the linac to the respiratory cycle. Before delivering radiation, care must be taken to ensure that the CT data set used in planning is an accurate description of the treatment configuration. Therefore, accounting for respiratory motion within the treatment plan will require a reexamination of the entire planning steps typically encountered for a lung cancer plan. As mentioned in Section 4.3.2.1, the step and shoot technique may take 5 seconds between each scan. In Section 6.1.3, respiratory periods were measured a 3.2s; thus, there may very well be motion artifacts in the image. Patients can hold their breath during the acquisition, but often this is not possible. Many patients are elderly and have respiratory problems: thus, one cannot expect to prolong the image acquisition period longer than several tens of seconds.

Because the densitometric features of the step and shoot CT scan are thought to better represent the treatment delivery conditions, it is believed that the dose computation using this CT data set will also become more accurate. If the same CT images are used for gated plans, this may have several consequences.

To investigate these consequences, a simulation of the potential motion artifacts of the step and shoot technique was conducted. From the data acquired from earlier experiments, it is reasonable to assume that a target within the lung may move at least 0 cm and at most ± 2.0 cm in the sup-inf direction. We neglect lateral displacements in this simulation. For a spherical target with an arbitrary radius, the image can be predicted as if it was obtained a using step and shoot CT data acquisition technique. We can model the motion of a target volume by assuming that it has temporal displacement pattern described by a sinusoid or a more realistic displacement pattern, such as the displacement pattern traced out in Section 6.1. The period of oscillation of the target can be set as 3.2 seconds, which was the average respiratory frequency of the patients observed in the earlier measurements.

```
% ctmove.m


clear all;          % Wipe out the memory buffer


% Enter in parameters of scan the
        Period=3.2;   % Period of Respiration [s]
        Disp=2;              % Total Displacement of Target [cm]
        Targetsize=3;% Radius of Target [cm]
        Stepsize=.5;  % CT Resolution [cm]
        Timeperscan=5;  % Time per scan [s]

    ...
```

Figure 6.16: Input parameters in the step and shoot CT image modeling.

Given the temporal displacement function, amplitude of oscillation, radius of target, scan time per slice, and slice interval, one can predict the shape of a moving object as seen on a CT image. The variables in the simulation are the target shape, respiratory period, distances between scans, and amplitude of oscillation. The time between the step and shoot scans is fixed at 5 seconds. Figure 6.16 displays a portion of a subroutine written in the Matlab environment that performs this simulation. The tabbed arguments are defined by the user and the target may be any arbitrary 2D function. The motion of a sphere was modeled here for illustration.
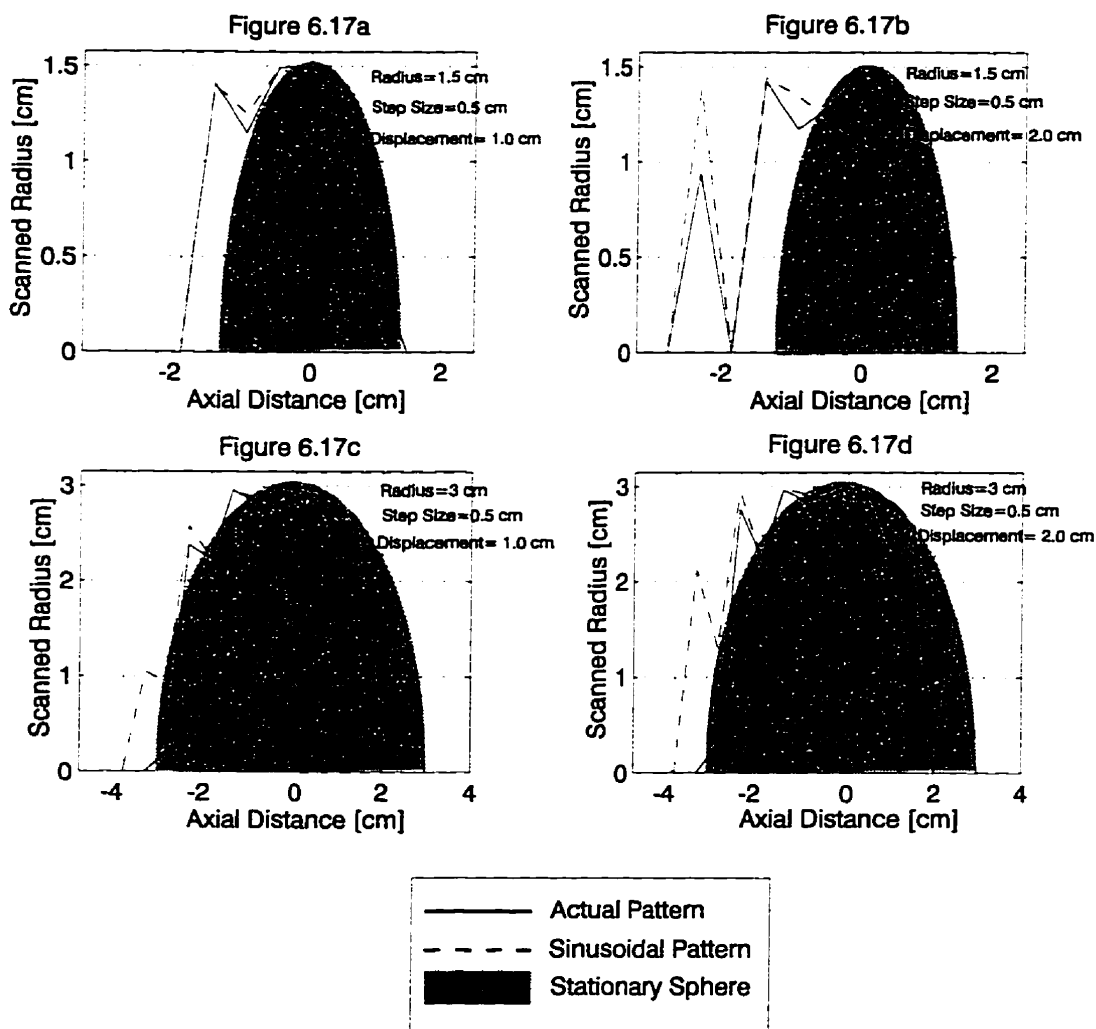
Figure 6.17a-d: Illustrations of potential artifacts for step and shoot imaging while free breathing. All scans assume 0.5 cm resolution and 5 seconds intervals between scans. The shaded region indicates the shape of the stationary target.

We assume that the target is isotropic, homogeneous, rigid and position of center of mass at the origin. For the sinusoidal variation, we assume that the object begins at the origin and displaces inferiorly with an amplitude equal to the specified value. For the realistic pattern, we assume that the target begins at the end-exhalation phase at the origin. The target then displaces its maximum amplitude in the negative direction. Thus, the negative z direction points inferiorly while the positive z direction points superiorly. The displacement mimics that of a target sitting on the diaphragm; pausing at end-exhalation, which is at the origin, and traversing its maximum displacement in the inferior direction.

Figures 6.17a-d illustrate the CT "images" for various target radii, displacements, and step sizes in patient's X-Y plane as observed for a step and shoot sequence with 5 s intervals. The figures illustrate that errors can occur when delineating the target volume if care is not taken to accurately chose step sizes for various target sizes. Higher resolutions may be necessary to define the target. However, under many conditions, a 0.25 cm resolution is not often done for diagnostic scans because of its increased time and integral dose to the patient. More likely, 0.5 cm or 1.0 cm slice intervals are used. Figure 6.17b illustrates the discontinuous appearance of the spherical target in the axial direction, at 0.5 cm resolution, for a 1.5 cm radius target displacing 2.0 cm from its central position. For larger targets, this is not so much a problem, however, for targets with radii less than 2.0 cm, proper imaging would require higher resolution or other techniques.

The figures once again illustrates the fact that the average position of the target is less than half the maximum distance observed for the target. Because the target spends more time about the origin, the artifacts are not as great. For larger targets (those with a radius greater than 3.0 cm) that displace less than 1.0 cm, one can expect this method of image acquisition to be fairly accurate when a slice resolution of 0.5 cm or less is used.

If gated radiotherapy is pursued, step and shoot acquisition while the patient is freely breathing may inaccurately assess the target volumes, unless the resolution is 0.5 cm or greater. A higher resolution of imaging will improve delineation at the expense of increased total acquisition time and increased integral dose to the patient. If gated radiotherapy is pursued, the scanning must be such that the CT image recreates the treatment configuration. It has already been mentioned that full thoracic diagnostic scans can be made through helical scanning while asking the patient to hold their breath. Helical CT images may be used for treatment planning provided that the patient holds their breath during treatment.

6.3.2 Gated Radiotherapy

A temporal analysis of videotaped fluoroscopic displacements of the diaphragm indicates that for targets situated on the diaphragm, a stable and reproducible target volume is achievable by gating the radiation beam at end-exhalation (see Figure 6.18). This observation of a relatively stable and reproducible position at end-exhalation is in agreement with the findings of Kubo et al. (1995) and Ohara et al. (1987) According to the temporal displacement data obtained, return positions at end exhalation may be in error by approximately 3 mm. If a tumour sitting on the diaphragm were moving 2.0 cm, sparing a 1.0 cm margin through gating the radiation at end exhalation would require 1/0.6, or 1.7 times longer than if the beams were on continuously for the treatment.

If gating, the duty factor, or beam-on time divided by total treatment time, will depend on the margin of PTV spared. Figure 6.19 shows beam-on times as a function of PTV margin irradiated, with the sup-inf PTV margin equal to 2.0 cm, for three different displacement functions: normal (as in Figure 6.18), square, and sinusoidal displacements. An inflection point is observed at about 1.0 cm regardless of the patient's respiratory frequency, or type or extent of motion. This implies that in the general case, treatment times become optimal when the spared PTV margin is equal to at least a centimetre. Under these circumstances, gating the beam would require a treatment time approximately 1.5 times longer than if the beam is on continuously.

Huang et al. (1996) report that a stable and reproducible target position may also be achieved while the patient holds his or her breath at inhale. This will also allows for a significant increase in the duty factor, and therefore lower treatment times.
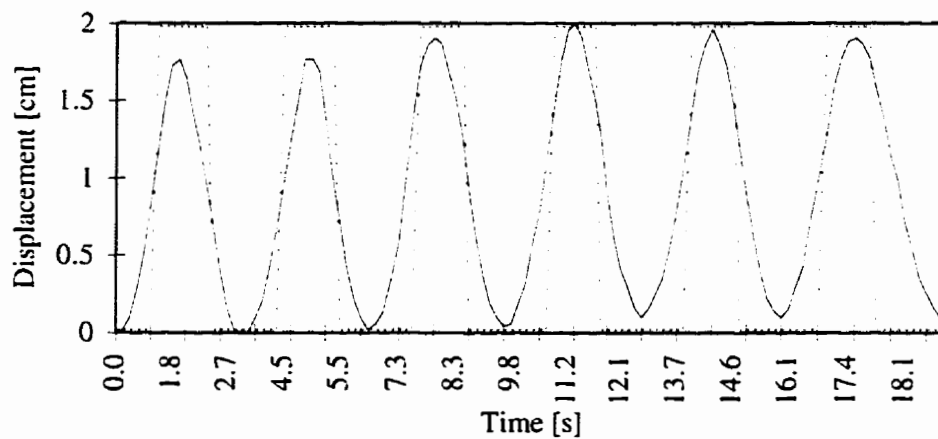
Figure 6.18: Actual displacement of target with respect to time. Shown in the dotted line is a square wave signal.
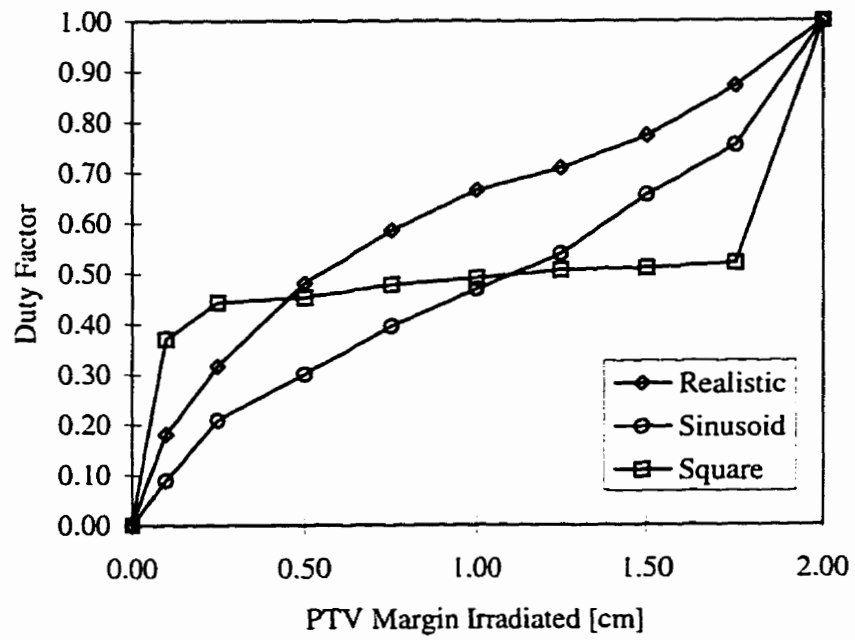
Figure 6.19: Duty factors for various PTVs for a target with radius of 3.0 cm, displacing 2.0 cm. The shape of the beam on-time curve is independent of the size of the target

7. Summary and Discussions

7.1 Summary

7.1.1 Inhomogeneity Compensation and Dose Optimisation

Considering the results from the two test phantoms used in Section 5.1, adequate inhomogeneity compensation is possible through scaling the water equivalent inhomogeneity by a thickness reduction ratio. This improved uniformity does not come without the increase in surface dose adjacent and upstream from the phantom and build up of dose beneath the inhomogeneity further downstream. When using the TRR method of internal inhomogeneity compensation, the material under-attenuates the beam; this results in slightly greater dose at the target site. Despite, this under-compensation, the method improves the homogeneity at the target depth significantly. For the phantoms used in these experiments, the maximum deviation from the target dose was +5%, with an average error of +2%. The improper value of trr is not only due to the inadequate accountance of charged particle equilibrium, it also stems from the improper assessment of scatter contributions of the inhomogeneous medium.

When modeled into the ATP dose calculation algorithm, the Batho algorithm predicts the dose effects for the compensators well within reasonable accuracy. There is good agreement between the measured data and the Batho algorithm despite the fact that it consistently underestimates the dose beneath the inhomogeneity. The average discrepancy between the Batho algorithm and measured data at the correction depth with the compensator in place is approximately 3%. The maximum error observed between the algorithm and measured data is 5%.

The iterative method to construct an optimised compensator, as explained in this thesis, is also a reasonable method to achieve field flatness for arbitrary internal and external contours. Since the construction is based on simulating the dose within the patient, the compensator shape will only be as accurate as the dose calculation algorithm itself. It has been shown that the iterative method consistently overcorrects the required material to achieve beam flatness when the Batho inhomogeneity algorithm is used to predict the dose. There may be negative consequences for this overcompensation. The overcompensation can be minimised by placing a larger error tolerance during the compensator construction, allowing the iterations to halt after one pass, or by scaling the thicknesses of material by a factor greater than unity. The average electron density along the central beam's axis would be suitable for the scaling parameter since that value would properly correct for primaries along the central axis; in effect being a reduction ratio.

Divergent solutions are observed when there is an overcorrection of underdosed portions of the beam or an undercorrection of overdosed portions of the beam. These "artifacts" are dependent on the compensator thickness to dose matrix resolution and alignment of the compensator geometry to the dose matrix. Slight shifts in compensator may greatly amplify the loss or build up of dose along the periphery of sharp geometric or density boundaries (including the penumbra). In order for avoid potential misalignment, the resolution of the compensator should be less than or equal to the dose resolution multiplied by the ratio of source-to-tray and source-to-compensation plane distances. This ensures that the compensator

is observed as a smooth function relative to the dose matrix. In addition, the compensator thickness should lay in-line with the calculated dose points.

In the multi-beam arrangement, it is possible to obtain a high and uniform dose to the target volume through the following method: selecting beam entry points and field sizes; compensating for both internal and external inhomogeneities; and then using Sherouse's gradient vector approach to determine beam weightings, and wedge and collimator angles. The dose distributions of the optimised plans show high uniformity as the 95% isodose line wraps the PTV reasonably well. The distributions generated through this approach display sharp dose gradients at the point of beam intersection and conform tightly to the beam intersection points. Simulations have shown that the average dose over the planning target volumes is approximately 98% of the target dose, displaying modest improvements for large field treatments (field sizes equal to or greater than 10 cm), and more profound improvements for smaller field treatments (field sizes less than 10 cm). Compensators that correct for internal and external inhomogeneities are chiefly responsible for these improved distributions. The simplicity of this technique renders itself for easy implementation in three dimensions conformal therapies and complicated beam arrangements.

There are minor perturbations in the dose profiles after the introduction of the wedges. This is due to the existence of internal density and contour variations. Because the beam intensity is modulated significantly to create the isodose effect, the modulation has consequences to most notably the primary photon dose contribution at the compensated plane. The internal structures will invoke higher primary and lower scatter dose contributions from those contributions generated in a uniform distribution.

A concern for employing this method is the higher than normal dose to up stream structures through the "horns" in the beams; however, these effects were not obvious in the two dimensional simulations performed in this thesis work. Errors in the simulations stem primarily from the accuracy calculation algorithm itself. Areas for potential improvement in this method are better compensator construction to minimise overdosing of structures upstream, more accurate inhomogeneity algorithms employed in the iterative procedure, and modeling the effects of wedges or, alternatively, compensating for an arbitrary plane within the patient.

7.1.2 Effects of Respiration in Lung Cancer Treatment

The intent of Chapter 6 was to investigate the effects of respiratory motion in various stages of radiotherapy. Measurements of the lung were videotaped for cancer patients undergoing routine fluoroscopy. The diaphragm contributed the largest displacement, while less significant is the lateral motion of the chest wall. The lung was observed to displace from 12 to 26 mm in the superior-inferior direction, and the chest wall has been observed to displace from 2 to 4 mm in the lateral direction. The largest displacement observed for either the left and right diaphragm was 48 millimetres. The largest displacement observed for the lateral displacements for either the left or right chest wall was 10 millimetres.

The degree of target motion was a function of tumour position within the lung, size of the tumour, and other individual case specific factors. Tumours situated close to functional diaphragms displayed greater ranges of motion than those tumours situated superior to the diaphragm. Tumours situated in the mediastinum area displayed smaller ranges of motion than

those tumours situated lateral to the mediastinum. Obviously, the closer the tumour was situated to a functional respiratory muscle, the more prone it was to displacement subject to that muscular contraction.

Larger tumours, possibly due to their inertia, moved less whereas smaller tumours showed larger displacements. The larger tumours most often lay in the mediastinal region, which was found to be less mobile. Tumour extensions were observed to "anchor" themselves to various portions of the lung and mediastinum. These extensions added complexity to the tumour dynamics.

In some instances, a few of the respiratory muscles were dysfunctional or completely collapsed. This required the functional respiratory muscles to compensate for the lack of pleural pressure necessary for inducing an adequate expansion of lung volume for oxygenation. Therefore, the patterns of respiratory displacements were unique for every patient observed. In some instances, functional portions of the diaphragm were observed to displace up to 48 mm. whereas nonfunctional portions of the diaphragm remained flaccid.

The average respiratory period was 3.2 seconds with the lowest and highest being 2.4 and 4.0 seconds, respectively. The time averaged position of the realistic pattern is 1.1 cm, which significantly less than the sinusoidally time averaged position. It is reasonable to assume that the time average position of a target undergoing respiratory motion is less than half the distance of the largest displacement. The shape of the temporal distribution will greatly affect the time averaged position of the target.

Errors in these measurements stem primarily from low patient data accrual; a greater number of patient data will improve the statistical accuracy of the measurements. Correlational studies of displacements for patients of different age, sex, cancer type, etc., may prove useful in obtaining general insight on target motion. Measurements of the displacements of the targets themselves for various cancer types will most certainly provide useful information as well. Although correlational studies may provide helpful information when assessing the margins of the PTV, it is essential to assess each patient individually so that an adequate determination of the PTV can be made. When using the beam's eye view approach to radiotherapy planning, as often done in 3D-CRT, it becomes important to account for respiratory displacements accurately.

There are dosimetric consequences for allotting the margins around the clinical target volume specifically accounting for superior-inferior respiratory displacements. The dosimetric consequences are apparent when examining the dose volume histograms of 3D lung plans with various superior-inferior field margins. For the aforementioned method of beam optimisation, the effective volume will increase proportionally with every PTV margin added to a clinical target volume. That is, for every 0.25 cm PTV margin used on a target with a radius of 1.5 cm to 3.0 cm, there will be an associated increase in the effective volume of approximately 0.015. Because the lung exhibits large volume effects, a 1.0 cm reduction in the field sizes in the superior-inferior direction is significant enough to alter values of effective volumes. For targets with radii less than or equal to 1.5 cm, lung tissue complications from allotting 2.0 cm margins in the superior-inferior direction and a 1.0 cm margin laterally appear to be insignificant when using the Kutcher-Burman-Lyman model of dose volume histogram reduction and normal tissue complication probability.

There is a potential risk from allotting MTV respiratory margins for targets greater than 1.5 cm in radius. The Kutcher-Burman-Lyman model suggests that, when using our treatment

planning optimisation routine, targets smaller than 3.0 cm appear to have no associated complication probabilities, regardless of dose the target receives. This is due to the fact that the model predicts little changes in complications for effective volumes less than about 0.15. The model suggests that for a fixed complication probability, there is a limit on the deliverable dose that is determined by the size of the PTV. The size of the PTV depends on the associated margins such as the MTV. Although the equivalent effecitive volume of this margin seems small, at 0.014, it is significant enough to produce different normal tissue complication probabilities.

A reduction of the PTV of margins allotted for respiration, in the case of the RTOG 93-11 protocol, would result in a higher tolerable dose limit. Dose escalation to the tumour may be possible if margins specifically allotted for respiratory motion were not included in the planning target volume.

The largest source of error in this simulation would stem from the Lyman model itself; it is uncertain whether this model is an accurate descriptor of complication rates for organs that have a large volume effect. The values of NTCP are highly sensitive to the curve fitting parameters n and m. Margins of error in complication rates can be expected to be ± 10-30%, depending on the prescription dose. These errors are large and may be greater because the values of TD_{50} and TD_5 are subject to further verification. Other sources of error include the accuracy of the dose calculation and inhomogeneity correction algorithms. The bulk of the error in V_{eff} stems from the accuracy of the dose calculation algorithm. This error, being on the order of 6%, is not significant for effective volumes greater than 0.10, but may be of importance for effective volumes less than 0.10. However, for effective volumes equal to or less than 0.10, higher doses on the order of 100 Gy would appear to be tolerable. In such an instance, dose constraints would be minimal since so little of the healthy lung receives the prescription dose.

If methods are devised that reduce the MTV alloted for respiration, care must be taken to ensure that the CT data set used in planning is an accurate description of the treatment configuration. Because the densitometric features of the step and shoot CT scan are thought to better represent the treatment delivery conditions, it is believed that the dose computation using this CT data set will also become more accurate. If these images are used for gated plans, there are potential negative consequences. Errors can occur when delineating the target volume if care is not taken to accurately chose step sizes for various target sizes. Higher resolutions may be necessary to define the target. However, under many conditions, lower resolutions are not often done for diagnostic scans because of its increased time and integral dose to the patient. Helical CT images may be used for treatment planning provided that the patient holds their breath during treatment.

A temporal analysis of videotaped fluoroscopic displacements of the diaphragm indicates that for targets situated by the diaphragm, a stable and reproducible target volume is achievable by gating the radiation beam at end-exhalation. This observation of a relatively stable and reproducible position at end-exhalation is in agreement with the findings of Kubo et al. (1995) and Ohara et al. (1987). According to the temporal displacement data obtained, return positions at end exhalation may be in error by approximately 3 millimetres. If a tumour sitting on the diaphragm were moving 2.0 centimetres, sparing a 1.0 centimetre margin through gating the radiation at end exhalation would require 1/0.6, or 1.7 times longer than if the beams were on continuously for the treatment. Treatment times become optimal when the spared PTV margin is equal to at least a centimetre.

7.2 Discussions

7.2.1 Inhomogeneity Compensation and Dose Optimisation

There are two major schools of thought regarding inhomogeneity corrections: they should not be performed and used while devising a patient plan until the algorithms can replicate the magnitude of errors in homogeneous dose calculation, which is typically on the order of 2%, and; some type of correction should be done, since the corrected value will better represent the true dose. There are both advantages and disadvantages for performing inhomogeneity calculations; it is not the intent of the writer to dwell on these but instead caution the reader that the concept of inhomogeneity compensation is therfore another potential point of contention. As the state exists today, there is a great need for inhomogeneity algorithms that can predict the dose to with both precision and accuracy. In addition, it is essential that these new algorithms can be implemented without a great cost of time and resources. Ahnesjö's collapsed cone approximation shows promise as being a very accurate inhomogeneity algorithm that may triumph this issue. One can expect that until a time exists where all institutions perform inhomogeneity corrections on a routine basis, the concept of inhomogeneity compensation may not become feasible. In addition, it is unlikely that surface correcting compensators would be used in a clinical setting, unless the patient has abnormally large surface contour variations. Compensating for internal inhomogeneities would certainly not be considered in the general clinical setting. Treatment factors, such as target motion, has yet to be investigated for this type of correction.

The construction of compensators themselves are in fact a time and resource consuming exercise, and some may argue that the cost is greater than the plans overall improvement. However, a considerable amount of research is being directed in very sophisticated inverse planning and beam modulation techniques for conformal therapies. Generally, these sophisticated dose optimisation algorithms that employ dynamic beam modulation require a great deal of computer time and resources. Some optimisation algorithms require a minimum of 6 beams to be used in the treatment plan, where each beam is modulated in some manner. Under these circumstances, a considerable amount of time and expertise would be required in developing, processing, and executing the vast amount of data required to deliver the plan. In brief, whether there is a cost-benefit advantage of using inverse planned algorithms or "forward" planned techniques for conformal therapies has yet to be investigated. With respect to lung cancer treatment, there are specific scenarios, such as treatment of the esophagus, where both contour correction and inhomogeneity compensation may be realised.

The fact that commercial systems, such as Helax TMS, may contain algorithms to automatically generate optimised compensators illustrates the fact that the radiotherapy "market" is concentrating more efforts into beam modulation.

7.2.2 Effects of Respiration in Lung Cancer Treatment

There have been preliminary reports in the literature of institutes employing some type of photon beam respiratory gating for lung cancer treatment. At the time of writing, there are approximately three institutes in North America who participate in some type of respiratory gated irradiation of lung cancers.

Kubo et. al (1996) and Ohara et al. (1987) have both demonstrated that it is technically possible to perform some type of electronic gating of the radiation beam to the respiratory

cycle. However, a major concern for many institutes is not reducing the margins alloted for respiration, but ensuring that the planning target volume is completely irradiated. From a clinical point of view, the clinicians primary concern would be ensuring that the target is uniformly irradiated; the additional PTV margin irradiated may be, in the opinion of many, a regretful but necessary margin of healthy tissue irradiated. This demonstrates the need for verification tools, such as on-line portal imaging, to ensure that the target is completely irradiated. Once clinicians and planners can be assured that the target position can be reproduced accurately, the concept of gating the radiation beam may become a feasible mode of treatment.

In addition to these concerns, questions regarding the dose-response characteristics of the lung need to be properly assessed. It was shown in Chapter 6 that the errors in the Kutcher-Burman-Lyman complication models can be extreme for smaller targets within the lung. Until the dose-response relationships of the lung are more accurately ascertained, convincing the academic community of the dosimetric advantages of respiratory PTV sparing may be difficult. In fact, there may not be a significant change in complications if Emami's tolerance data was under-estimated.

7.3 Future Considerations

7.3.1 Optimisation of Lung Cancer Treatment Through Beam Modulation

The aforementioned technique can be easily used for other purposes rather than for lung cancer treatment. In any instance where there are either internal and/or internal inhomogeneities, the method can be applied. In such instances, it may be beneficial to extend the algorithm to compensate to an arbitrary plane with respect to the isocentre. In complicated geometries, such as the head and neck, where oblique beams may be used, compensating for an arbitrary plane may be more beneficial. In the examples illustrated here, the isodoses were rotated with reasonable homogeneity after the wedges were introduced in the beam. For oblique beams, which are commonly used in head and neck treatments, the wedged and compensated distribution may not be flat due to the marked contour variations. It may be beneficial to determine the desired wedge angles apriori, and then correct for the inhomogeneity of the wedged isodose at the isocentric plane. This would be a natural extension of the existing algorithm and would not require much additional work.

To determine the best gantry angle, the tumour size can be approximated through a polygon, which can then be minimised into an arbitrary number of desired beams. Tumour volumes are normally specified by the clinician through discretising the PTV contour with small connecting lines. The main objective of the planner is to ensure that the contour along with its interior contents are adequately irradiated to within some specified level. If the planner constrains the beam to enter only within a certain values of gantry angles, points within the polygon can be approximated by a slightly larger polygon that fits around the PTV, while minimising the amount of additional healthy tissue irradiated. The approximated PTV can then be defined as beam edges and a computer can iterate through the allowed gantry angles. Furthermore, the planner can specify the number of beams allowable in the plan; the number of beams will thus become an important consideration when determining the approximated PTV contour. Once the optimal gantry angles are found and the planner approves the gantry

arrangement, then each beam can be compensated at isocentre and Sherouse's method can be applied. If a certain variable within the plan is undesireable, for instance a 60° wedge is undesired, the planner can change and fix the wedge angle and vary the remaining variables to reach the optimal solution. Such a technique could be done within or outside the planning system. An additional PC beside the planning system could contain the program and produce the outputs. This would allow for the planner to have complete control over the treatment planning system and its outputs to the verification system.

Another potential use of the gradient vector method is the strategic construction of non-uniform distributions. For instance, the clinician may determine that the distribution should not be uniform throughout the planning target volume, but instead consist of a varied distribution with ranges specified by the planner. The clinician can taylor the distribution to the relative percentage of clonogenic cells with the planning target volume. Uni-directional gradient distributions can easily be achieved through ensuring that the gradient vector is nonzero and points in the direction of the desired dose gradient. Furthermore, if divergent gradient distributions were desired, one could use several points lying on the isocentric plane to customise the dose distribution. An extension of the vector method as applied to several points, as opposed to just one point can be done to customise a dose distribution. In this manner, the possibility of "conformal avoidance" may easily be achieved, that is, instead of customising the dose to the planning target volume, one customises the distribution such that critical structures do not receive damaging doses [Mackie, 1995].

The focus of the radiotherapy is shifting from 3D conformal therapy to more global problems in treatment planning, such as inverse planning approaches, multi-beam modulation, and biological modelling. This shift is partially due to preliminary outcomes of the conformal therapy hypothesis, and also from advances in integrated softwares, hardwares and merged technologies.

One major question to be resolved is the extent of the cost-benefit for these various types of treatment implementations. For many institutes, it may not be realistic to spend the vast amount of resources required to implement complicated inverse planning methods that incorporate biological models; instead, inexpensive, yet sophisticated tools may be introduced into the existing technologies so as to deliver conformal treatments within the "forward planning" environment. For instance, it may be more economically viable for some institutes to implement beam modulation by way of physical compensators as opposed to dynamic beam modulation. Likewise, physical blocks can be manually constructed for beam shaping as opposed to multileaf collimation. There are, of course, advantages for automating procedures since they will most likely incur fewer long term costs. However, if there are components, or pieces of the puzzle, within the institute, one can deliver highly sophisticated treatments with minimal overhead costs.

As computers become more powerful and less expensive, Monte Carlo simulations for dose computations may soon become the standard method of dose calculation. Over the last five years, calculation times for 3D geometries have migrated from being on the order of days to hours of computation times. It is possible that within the next century, the 2% percent benchmark for inhomogeneity computations may be indeed be realised.

7.3.2 Accounting for Respiration in Cancer Treatment

Electronically gating the respiratory cycle to the linac may very well become a reality in the near future. Instead of using strain gauges to measure the diaphragmatic displacements, one could gate the radiation beam in a more feasible manner, such as monitoring the displacement of the diaphragm and chest wall through lasers. To begin, the CT data set may first be acquired under some known conditions such that the lung and tumour can be contiguously defined within the data set. The scan may be during any portion within the respiratory cycle, since the method will only turn the beam on whenever a certain patient geometry is recreated. Once the CT data is acquired, a plan can be devised and the dose can be computed. Before the simulation, digitally reconstructed radiographs can be generated, which are reconstructions of two dimensional planar views, for each of the beams in the treatment plan. Since the chest wall and abdomen are the two major objects that displace during the respiratory cycle, range sensitive devices, such as lasers, may be used to monitor the position of the chest wall and abdomen, which can then be correlated to the target position within the lung. These range finding sensors can then record the height of the diaphragm and chest wall for the positions where the fluoroscopic images match the digitally reconstructed images. Thus, the position of the target can then be uniquely defined for each patient, regardless of the location and size of the target, or other patient specific factors.

This displacement data can then be sent to the record and verify software of the treatment machine and identically positioned lasers can monitor the position of the chest wall and abdomen. In addition, such a verification tool may easily be used for other purposes, such as ensuring patient set up and orientation.. During the treatment, the laser can detect the appropriate height of both the abdomen and chest wall and turn the beam off when the simulated positions are recreated. Randomly sampled electronic portal images taken during the beam-on times may be used during the course of the treatments to ensure that the target was adequately irradiated. If the target were to stray from the target site, the linac could electronically switch the beam off. This would also allow for the patient to be active participant within the treatment itself; for instance, the patient could choose to recreate the treatment position or simply breath freely. The patient would have to visit the simulator only once during their course of treatment, unless there was a significant change in the patient body contour. Patients may experience weight loss during their course of radiation treatment; in such instances, another diagnostic simulation can be performed and the new positions of the chest wall and abdomen can be re-entered within the treatment management parameters.

This could become an economically feasible system for accounting for respiratory motion within a treatment plan. The range findering sensors can be permanently mounted within the simulator and treatment rooms, minimising set-up times and errors, while also being completely non-invasive to the patient. Furthermore, the devices may be used in tandem with other devices, such as an ECG monitor, for monitoring cardiac motion. If one were to do so, CT images that can contiguously define the heart would be necessary. During the time of writing, there have been reports in the literature of the possibility of obtaining contiguous CT images of the heart during breath hold [Nolan et al. 1997]. This would then allow for the possibility of accounting for both respiratory and cardiac displacements within the lung.

Bibliography

Agostoni, E; Mognoni, P; Torri, G; Saracino, F. "Relation between changes in rib cage circumference and lung volume" *Journal of Applied Physiology* 20:1179-1186 (1965)

Ahnesjö, A. "Collapsed cone convolution of radiant energy for photon dose calculation in heterogeneous media" *Med. Phys.* 16:577-592 (1989)

Ahnesjö, A; Saxner, M; Trepp A. "A pencil beam model for photon dose calculation" *Med. Phys.* 19:263-273 (1992)

Ahnesjö, A; Andreo, P. "Determination of effective bremsstrahlung spectra and electron contamination for photon dose calculations" *Phys. Med. Biol.* 34:1451-1464 (1989)

Alfidi, R.J; MacIntyre, W.J; Haaga, J.R. "The effects of Biological Motion on CT resolution" *American Journal of Roentgentology.* 127:11-15 (1976)

Ansbacher, W; Robinson, D.M; Scrimger, J.W; "Missing tissue compensators: Evaluation and optimization of a commercial system" *Med. Phys.* 19 ;1267-1272 (1992)

Armstrong JG; Burman C; Leibel S; Fontenla D; Kutcher G; Zelefsky M; Fuks, Z; "Three-dimensional conformal radiation therapy may improve the therapeutic ratio of high dose radiation therapy for lung cancer" *Int. J. Radiat. Oncol. Biol. Phys.* 26:685-9 (1993)

Attix. F.H. "Introduction to Radiological Physics and Radiation Dosimetry" New York, U.S.A. John Wiley & Sons (1986)

Austin-Seymour, M;Chen, G.T; Rosenman, J;Michalski, J; Lindsley. K; Goitein, M. "Tumor and target delineation: current research and future challenges" *Int. J. Radiat. Oncol. Biol. Phys.* 33:1041-52 (1995)

Austin-Seymor, M; Kalet, I; McDonald, J; Kromhout-Schiro, S; Jakcy, J; Hummel, S; Unger, J. "Three dimensional planning target volumes: a model and a software tool" *Int. J. Radiat. Oncol. Biol. Phys.* 33:1073-1080 (1995)

Bagne, F.R; Samsami, N; Hoke, S.W; Bronn, D.G; "A study of effective attenuation coefficient for calculating tissue compensator thickness" *Med. Phys* 17:117-121 (1990)

Balter, J.M; Ten Haken, R.K; Lawrence, T.S;Lam, K.L; Robertson, J.M. "Uncertainties in CT-based radiation therapy treatment planning associated with patient breathing" *Int. J. Radiat. Oncol. Biol. Phys.* 36:167-74 (1996)

Batho, H.F. *J. Can. Assoc. Radiol.* 1:15:79 (1964)

Battista, J.J; Rider, W.D; Van Dyk, J. "Computed tomography for radiotherapy planning" *Int. J. Radiat. Oncol. Biol. Phys.* 6:99-107 (1980)

Bortfeld, T; Bürkelbach, J; Boesecke, R; Schlegel, W. "Methods of image reconstruction from projections applied to conformation therapy" *Phys. Med. Biol.* 35:1423-1434 (1990)

Boyer, A.L. "Compensating filters for high energy x rays" *Med. Phys.* 9:429-433 (1982)

Boyer, A.L; Desorby, G.E; Wells, N.H. "Potential and limitations of invariant kernal conformal therapy" *Med. Phys* 18:703-712 (1991)

Boyer, A.L; Mok, E.C. "Calculation of photon dose distributions in an inhomogeneous medium using convolutions" *Med. Phys.* 13:503-509 (1986)

Bragg, D.G. "Current applications of imaging procedures in the patient with lung cancer. [Review]" *Int. J. Radiat. Oncol. Biol. Phys.* 21:847-851(1991)

Brahme, A. "Optimization of stationary and moving beam radiation therapy techniques" *Radiotherapy Onc.* 12:129-140 (1988)

Brock, W.A; Baker, F; Peters, L.J. "Radiosensitivity of human neck and squamous cell carcinomas in primary culture and its potential as a predictive assay of tumor radiocurability" *Int. J. Radiat. Oncol. Biol. Phys.* 56:751-760 (1989)

Burman, C; Kutcher, G.J; Emami, B; Goitein M. "Fitting of normal tissue tolerance data to an analytic function" *Int. J. Radiat. Oncol. Biol. Phys.* 21:123-135 (1991)

Campbell, E.J.M; Agostoni, E; Newsom-Davis, J; "The Respiratory Muscles: Mechanics and Neural Control" London U.K Lloyd-Luke (Medical Books) (1970)

Cassell, K.J; Hobday, P.A; Parker, R.P. "The implementation of a generalized Batho inhomogeneity correction for radiotherapy planning with direct use of CT numbers" *Phys. Med. Biol.* 26:825-833 (1981)

Chadwick, K.H; Leenhouts, C.J. "A molecular theory of cell survival" *Phys. Med. Biol.* 18:78 (1983)

Chu. T; Lee K; Dunscombe P. "A technique for the evaluation of a missing tissue compensator system" *Med. Phys.* 20:713-716 (1993)

Cox JD; BArbor-Derus S; Hartz AJ; Fischer M; Byhardt RW; Komaki R; Wilson JF; Greenberg, M. "Is adenocarcinoma/large cell carcioma the most radiocurable type of cancer of the lung?" *Int. J. Radiat. Oncol. Biol. Phys.* 12:1801-1805 1986

Cozzi, A.F; Cozzi, L; Garavaglia, G. "Wedge factors: dependence on depth and field size" *Radiotherapy & Oncology* 39: 31-4 (1996)

Cunningham, J.R; Wright, D.J; Webb, H.P; Rawlinson, J.A; Leung, P.M. "A semi-automatic cutter for compensating filters" *Int. J. Radiat. Oncol. Biol. Phys.* 1:355-60 (1976)

Cunningham,J.R. "Scatter-Air Ratios" *Phys. Med. Biol.* 17:42-51 (1972)

Daftari, I; Petti, P.L; Collier, J.M; Castro, J.R; Pitluck, S. "The effect of patient motion on dose uncertainty in charged particle irradiation for lesions encircling the brain stem or spinal cord" *Med. Phys.* 18:1105-1115 (1991)

Davies, S,C; Hill, A.L; Holmes, R.B; Halliwell, M; Jackson, P.C. "Ultrasound quantitation of respiratory organ motion in the upper abdomen" *Br. J Radiol.* 67:1096-1102 (1994)

Djordjevich, A; Bonham, D.J; Hussein, E.M; Andrew, J.W; Hale, M.E. "Optimal design of radiation compensators" *Med. Phys* 17: 397-404 (1990)

Derenne, J.P; Macklem, P.T; Roussos, C. "The respiratory muscles: mechanics, control, and pathophysiology" American Review of Respiratory Disease. 118(1):119-33 (1978)

Desobry, G.E; Wells, N.H; Boyer, A.L. "Rotation kernels for conformal therapy" *Med. Phys.* 18:481-487 (1991)

Drzymala, R.E; Mohan, R; Brewster, L; Chu, J; Goitein, M; Harms, W; Urie, M. "Dose Volume Histograms" *Int. J. Radiat. Oncol. Biol. Phys.* 21:71-78 (1991)

Dunscombe, P.B; Fox, K; Loose, S; Leszczynski, K. "The investigation and rectification of field placement errors in the delivery of complex head and neck fields" *Int. J. Radiat. Oncol. Biol. Phys.* 26:155-161 (1993)

Ekstrand, K.E; Barnes, W.H. "Pitfalls in the use of high energy X rays to treat tumors in the lung" *Int. J. Radiat. Oncol. Biol. Phys.* 18:249-252 (1990)

Ellis, F; Hall, E.J; Oliver, R. "A compensator for variations in tissue thickness for high energy beams" *Brit. J. Radiol.* 32:421-422 (1959).

Ellis, F; Lescrenier, C. "Combined compensator for contours and heterogeneity" *Radiology* 106:191-194 (1973)

Emami B; Lyman J; Brown A; Coia L; Goitien M; Muzenrider JE; Shank B;Solin LJ; Wesson M; Tolerance of normal tissue to therapeutic irradiation [Review] *Int. J. Radiat. Oncol. Biol. Phys.* 21(1) : 109-22 May 15 : 1991

Emami, B; Purdy, J.A; Manolis, J; Barest, G; Cheng, E; Coia, L; Doppke, K; Galvin, J; LoSasso, T; Matthews, J; et al. "Three-dimensional treatment planning for lung cancer" *Int. J. Radiat. Oncol. Biol. Phys.* 21:217-227 (1991)

Essers, M; Lanson, J.H. "The accuracy of CT-based inhomogeneity corrections and in vivo dosimetry for the treatment of lung cancer" *Radiotherapy & Oncology* 37:199-208 (1995)

Evans, R.D. "The Atomic Nucleus" McGraw-Hill, NewYork (1955)

Faddegon, B.A; Pfalzner, P. "Computer aided design and verification of megavoltage tissue compensators for oblique beams" *Med. Phys.* 15:757-762 (1988)

Feaster, G.R; Agarwal, S.K; Huddleston, A.L; Friesen, E.J; "A missing tissue compensator" *Int. J. Radiat. Oncol. Biol. Phys.* 5:277-280 (1979)

Ford RL; Nelson WR. The EGS Code System, Stanford Linear Accelerator Report 210 (Staanford CA: Stanford Linear Accelerator) 1978

Fung, Y.C. "Frontiers in biomechanics" Springer-Verlag, New York (1986)

Galvin, J.R; Gingrich, R.D; Hoffman, E; Kao, S.C; Stern, E.J; Stanford, W. "Ultrafast computed tomography of the chest. [Review]" *Radiologic Clinics of North America* 32:775-793 (1994)

Genereaux, G.P. "Computed tomography and the lung: review of anatomic and densitometric features with their clinical application. [Review]" *Journal of the Canadian Association of Radiologists* 36:88-102 (1985)

Goitein, M. "Calculation of the uncertainty in the dose delivered during radiotherapy" 5:608-612 (1985)

Goitein, M; Abrams, M; Rowell, D; Pollari, H; Wiles, J. "Multi-dimensional treatment planning: II. Beam's eye-view, back projection, and projection through CT sections" *Int. J. Radiat. Oncol. Biol. Phys.* 9:789-97 (1983)

Goitein, M. "Causes and consequences of inhomogeneous dose distributions in radiation therapy" *Int. J. Radiat. Oncol. Biol. Phys.* 12:701-704 (1986)

Gonzalez, R.C; Woods, R.E. "Digital image processing" Addison-Wesley, Don Mills Ontario (1993)

Graffman, S; Groth, T; Jung, B; Skollermo, G; Snell, J.E. "Cell kinetic approach to optimising dose distributions in radiation therapy" *Acta Radiologica* 14(1):54-62 (1975)

Graham, M.V; Matthews, J.W; Harms, W.B Sr; Emami, B; Glazer, H.S; Purdy, J.A; "Three-dimensional radiation treatment planning study for patients with carcinoma of the lung" *Int. J. Radiat. Oncol. Biol. Phys.* 29:1105-1117 (1994)

Gur, D; Drayer, B.P; Borovetz, H.S; Griffith, B.P. "Dynamic computed tomography of the lung: regional ventilation measurements" *J. Comp. Ass. Tomo.* 3:749-753 (1979)

Haruaz, G; Bronskill, M.J. "Comparision of the livers's respiratory motion in the supine and upright positions: Concise communitication" *J. Nucl. Med.* 20:733-735 (1979)

Hazuka, M.B; Turrisi, A.T. 3d; Lutz, S.T; Martel, M.K; Ten Haken, R.K; Strawderman, M; Borema, P.L; Lichter, A.S. "Results of high-dose thoracic irradiation incorporating beam's eye view display in non-small cell lung cancer: a retrospective multivariate analysis." *Int. J. Radiat. Oncol. Biol. Phys.* 27:273-84 (1993)

Hobday, P; Hodson, N.J; Husband, J; Parker, R.P; "Computed tomography applied to radiotherapy treatment planning: techniques and results" *Radiology* 133:477-482 (1979)

Holmes, T.W; Mackie, T.R; Reckwerdt, P. "An iterative filtered backprojection inverse treatment planning algorithm for tomotherapy" *Int. J. Radiat. Oncol. Biol. Phys.* 32:1215-1225(1995)

Huang DT; Tercilla O; Lutz S; Silverman L; Schmidt-Ullrich R. "A Patient Self-Gated Technique for Radiotherapy to Lung Cancers" *Proceedings of the 38th Annual ASTRO Meeting* p349 (1996)

International Commission on Radiation Units and Measurements "Determination of absorbed dose in a patient irradiated by beams of X or Gamma rays in radiotherapy procedures" ICRU Report 24 Washington D.C. U.S.A. (1976)

International Commission on Radiation Units and Measurements "Prescribing, Recording, and Reporting Photon Beam Therapy" ICRU Report 50 Washington DC (1993)

Jackson, A. "Wax retraction technique for compensators" *Br. J Radiol.* 43:859-867 (1970)

Jacobs I. Vanregemorter J. Scalliet P. "Influence of respiration on calculation and delivery of the prescribed dose in external radiotherapy" *Radiotherapy & Oncology* 39:123-128 (1996)

Janicki, J.S; Weber, K.T; Gochman, R.F; Shroff, S; Geheb, F.J. "Three-dimensional myocardial and ventricular shape: a surface representation" *American Journal of Physiology* 241:H1-11 (1981)

Johns, H.E; Bruce, W.R; Reid, W.B. "The independence of depth dose on focal skin distance" *Br. J Radiol.* 31:254 (1958)

Johns, H.E; Cunningham, J.R. "The Physics of Radiology" Charles C Thomas, Springfield U.S.A. (1983)

Jursinic, P.A; Podgorsak, M.B; Paliwal, B.R. "Implementation of a three-dimensional compensation system based on computed tomography generated surface contours and tissue inhomogeneities" *Med. Phys.* 21:357-365 (1994)

Källman, P; Lind, B.K; Brahme, A. "An algorithm for maximizing the probability of complication-free tumour control in radiation therapy" Phys. Med. & Biol. 37:871-90 (1992)

Källman, P; Lind, B; Eklof, A; Brahme, A. "Shaping of arbitrary dose distributions by dynamic multileaf collimation" *Phys. Med. & Biol.* 33:1291-300 (1988)

Kappas C; Rosenwald, J. "Quality Control of Inhomogeneity Correction Algorithms Used in Planning Systems" *Int. J. Radiat. Oncol. Biol. Phys.* 32:847-858 (1995)

Karzmark, C.J; "Advances in linear accelerator design for radiotherapy" *Med. Phys.* 11:105-128 (1984)

Khan, F.M. "The Physics of Radiation Therapy" Williams & Wilkins, Baltimore U.S.A. (1984)

Kijewski, P.K; Chin, L.M; Bjärngard, B.E. "Wedge-shaped dose distributions by computer-controlled collimator motion" *Med. Phys.* 5: 426-429 (1978)

Killoran, J.H; Kooy, H.M; Gladstone, D.J; Welte, F.J; Beard, C.J. "A numerical simulation of organ motion and daily setup uncertainties: implications for radiation therapy" *Int. J. Radiat. Oncol. Biol. Phys.* 37:213-321 (1997)

Knöös, T; Ahnesjö, A; Nilsson, P; Weber, L. "Limitations of a pencil beam approach to photon dose calculations in lung tissue" *Phys. Med. & Biol.* 40:1411-1420 (1995)

Kollar, J. "Evaluation and modification of a differential SAR dose calculation algorithm" M.Sc's Thesis, University of Alberta (1996)

Korin, H.W; Ehman, R.L; Riederer, S.J; Felmlee, J.P; Grimm, R.C; "Respiratory kinematics of the upper abdominal organs: a quantitative study" *Mag. Res. Med.* 23:172-178 (1992)

Kubo, H.D; Hill, B.C. "Respiration gated radiotherapy treatment: a technical study" *Phys. Med. & Biol.* 41:83-91 (1996)

Kutcher, G.J; Burman, C. "Calculation of Probability factors for non-uniform normal tissue irradiation: the effective volume method" *Int. J. Radiat. Oncol. Biol. Phys.* 16: 16: 1623-1630 (1989)

Kutcher, G.J; Burman ,C; Mohan, R. "Compensation in three-dimensional noncoplanar treatment planning" *Int. J. Radiat. Oncol. Biol. Phys.* 20:127-134 (1991)

Kutcher, G.J; Burman ,C; Brewster L,M; Goitein, M, Mohan, R. "Histogram reduction method for calculating complication probabilities for three-dimensional treatment planning evaluations" *Int. J. Radiat. Oncol. Biol. Phys.* 21:137-146 (1991)

Langer, M; Brown, R; Kijewsli, P; Ha, C. "The reliability of optimization under dose-volume limits" *Int. J. Radiat. Oncol. Biol. Phys.* 26:529-538 (1993)

Leibel, S.A; Ling, C.C; Kutcher, G.J; Mohan, R; Cordon-Cordo, C; Fuks, Z. "The biological basis for conformal three-dimensional radiation therapy" *Int. J. Radiat. Oncol. Biol. Phys* 21:805-811 (1991)

Ling, C.C; Burman, C; Chui, C.S; Jackson, A; Kutcher, G.J; Leibel, S; LoSasso, T; Mageras, G; Mohan, R; Yorke, E; et al. "Perspectives of mutidimesional conformal radiation treatment" *Radiotherapy & Oncology* 29:129-139 (1993)

Lyman JT; Wolbarst AB. "Optimization of radiation therapy, 3: A method of assessing complication probabilities from dose-volume histograms" *Int. J. Radiat. Oncol. Biol. Phys.* 13:103-109 (1987)

Mackie, T.R. "A Study of Charged Particles and Scattered Photons in Megavoltage X-ray Beams" PhD's Thesis, University of Alberta (1984)

Mackie, T.R; El-Khatib, E; Battista, J; Scrimger, J; Van Dyk, J; Cunningham, J.R."Lung dose corrections for 6- and 15-MV x-rays" *Med. Phys.* 12:327-332 (1985)

Mackie, T.R; Bielajew, A.F; Rogers, D.W.O; Battista, J.J. "Generation of photon energy deposition kernels using the EGS Monte Carlo code" *Phys. Med. Biol.* 33:1-20 (1988)

Mackie, T.R; Holmes, T.W; Reckwerdt, P. J; Yang, J. "Tomotherapy: Optimized planning and delivery of radiation therapy" *Int. J. Imag. Sys. Tech.* 43:43-55 (1995)

Mackie, T.R; Palta, J.R. (Editors) "Teletherapy: Present and Future" *AAPM Proceedings of the 1996 Summer School* (1996)

Mageras, G,S; Kutcher, G.J; Leibel, S.A; Zelefsky, M.J; Melian, E; Mohan, R; Fuks, Z. "A method of incorporating organ motion uncertainties into three-dimensional conformal treatment plans" *Int. J. Radiat. Oncol. Biol. Phys.* 35:333-342 (1996)

Mageras, G.S; Mohan, R; Burman, C; Barest, G.D; Kutcher, G.J. "Compensators for three-dimensional treatment planning" *Med. Phys.* 18:133-140 (1991)

Mageras, G.S; Podmaniczky, K.C; Mohan, R. "A model for computer-controlled delivery of 3-D conformal treatments" *Med. Phys.* 19:945-953 (1992)

Martel, M.K; Ten Haken, R.K; Hazuka, M.B; Kessler, M.K; Turrisi, A.T; "Analysis of tumor dose-volume histograms in relationships to local progression free survival for lung cancer patients" *Int. J. Radiat. Oncol. Biol. Phys.* 27(suppl 1):238 (1993)

Martonen, T.B; Yang, Y; Hwang, D; Fleming, J.S. "Computer simulations of human lung structures for medical applications" *Comp. in Biol. & Med.* 25:431-446 (1995)

Mayles, W.P.M; Yarnold, J.R; Webb, S. "Improved dose inhomogeneity in the breast using tissue compensators" *Radiotherapy and Oncology* 22:248-251 (1991)

McKenna, W.G; Yeakel, K; Klink, A; Fraass, B.A; van de Geijn, J; Glatstein, E; Lichter, A.S. "Is correcting for lung density in radiotherapy treatment planning necessary?" *Int. J. Radiat. Oncol. Biol. Phys.* 13:273-278 (1987)

Michalski, J.M; Wong, J.W; Gerber, R.L; Yan, D; Cheng, A; Graham, M.V; Renna, M.A; Sawyer, P.J; Perez, C.A. "The use of on-line image verification to estimate the variation in radiation therapy dose delivery" *Int. J. Radiat. Oncol. Biol. Phys.* 27:707-716 (1993)

Mohan, R; Chui, C; Lidofsky, L. "Energy and angular distributions of photons from medical linear acclerators" *Med. Phys.* 12:592-597 (1985)

Mohan, R; Chui, C.S. "Use of fast Fourier transforms in calculating dose distributions for irregularly shaped fields for three dimensional treatement planning" *Med. Phys.* 14:70-77 (1987)

Mohan, R; Mageras, G.S; Baldwin, B; Brewster, L.J; Kutcher, G.J; Leibel, S; Burman, C.M; Ling, C.C; Fuks, Z. "Clinically relevant optimization of 3-D conformal treatments" *Med. Phys.* 19:933-944 (1992)

Moreland, M.A; Bergh, A.C.M; Bhagwandien, R; Janssen, W.M; Bakker, C.J.G; Lagendijk, J.J.W; Battermann, J.J. "The influence of respiration induced motion of the kidneys on the accuracy of radiotherapy treatment planning, a magnetic resonance imaging study" *Radiotherapy & Oncology* 30:150-154 (1994)

Mori, M; Murata, K; Takahashi, M; Shimoyama, K; Ota, T; Morita, R; Sakamoto, T. "Accurate contiguous sections without breath-holding on chest ct : value of respiratory gating and ultrafast CT" *Amer. J. Roet.* 162:1057-1062 (1994)

Morrill, S.M; Lane, R.G; Rosen, I.I. "Constrained simulated annealing for optimized radiation therapy treatment planning" *Computer Methods and Programs in Biomedicine* 33:135-144 (1990)

Morrill, S.M; Langer, M.L; Lane, R.G; Rosen, I.I. "Tissue heterogeneity effects in treatment plan optimization" *Int. J. Radiat. Oncol. Biol. Phys.* 30:699-706 (1994)

Niemierko, A; Goitein, M. "Calculation of normal tissue complication probabiltiy and dose-volume histogram reduction schemes for tissues woth a critical elements architecture" *Radiotherapy & Oncology* 20:166-176 (1991)

Niemierko, A; Goitein, M. "Implementation of a model for estimating tumor control probability for an inhomogeneously irradiated tumor" *Radiotherapy & Oncology* 29:140-147 (1993)

Niemierko, A; Urie, M; Goitein, M.   "Optimization of 3D radiation therapy with both physical and biological end points and constraints" *Int. J. Radiat. Oncol. Biol. Phys.* 23:99-108 (1992)

Nillson, B; Brahme, A. "Contamination of high-energy photon beams by scattered photons" *Strahlentherapie* 157:181-186 (1981)

Nochomovitz, L; Neil S. "Noninvasive respiratory monitoring: Contemporary issues in pulmonary disease. v. 3" New York, U.S.A, Churchill Livingstone (1986)

Noel, A; Aletti, P; Bey, P; Malissard, L. "Detection of errors in individual patients in radiotherapy by systematic in vivo dosimetry" *Radiotherapy and Oncology* 34:144-151 (1995)

Nolan, J; Cunningham, I.A. "Temporal inconsistencies in ECG-gated cardiac CT" *COMP 97 Conference Proceedings* 111-113 (1997)

O'Conner, J.E. "The variation of scattered x-rays with density in an irradiated body" *Phys. Med. & Biol.* 1:352-369 (1957)

Ohara, K; Okumura, T; Akisada, M; Inada, T; Mori, T; Yokota, T; Calaguas, M.J.B. "Irradiation synchronized with respiration gate" *Int. J. Radiat. Oncol. Biol. Phys.* 17(4): 853-857 (1989)

Orton, C.G; Mondalek, P,M; Spicka, M.S; Herron, D.S; Andres, L.I. "Lung corrections in photon beam treatment planning : Are we ready?" *Int. J. Radiat. Oncol. Biol. Phys.* 10:2191-2199 (1984)

Park, H.C; Almond, P.R. "Tissue compensation and verification of dose uniformity" *Medical Dosimetry* 18:193-196 (1993)

Perez, C.A; Bauer, M; Edelstein, S; Gillespie, W.W; Birch, R.   "Impact of tumor control on survival in carcinoma of the lung treated with irradiation" *Int. J. Radiat. Oncol. Biol. Phys.* 12:539 (1986)

Perez, C.A; Purdy, J.A; Harms, W; Gerber, R; Graham, M.V; Matthews, J.W; Bosch, W; Drzymala, R; Emami, B; Fox, S; Klein, E; Lee, H.K; Michalski, J.M, Simpson, J.R "Three-dimensional treatment planning and conformal radiation therapy: preliminary evaluation" *Radiotherapy & Oncology* 36:32-43 (1995)

Pengelly, L.D. "Mechanical properties of the diaphragm and their application to a mathematical model" *American Review of Respiratory Disease* 119(2 Pt 2):33-36 (1979)

Phillips, M.H; Pedroni, E; Blattmann, H; Boehringer, T; Coray, A; Scheib, S. "Effects of respiratory motion on dose uniformity with a charged particle scanning method" *Phys. Med. & Biol.* 37: 223-234 (1992)

Pin-Hua, Huang. "Scattered photons produced by beam-modifying filters" *Med. Phys.* 13:57-63 (1986)

Primiano, F.P, Jr. "Theoretical analysis of chest wall mechanics" *J. Biomech.* 12:919-931 (1982)

Press, W.H; Teukolsky, S.A; Vetterling, W.T; Flannery, B.P. "Numerical Recipies in C" Second Edition New York, U.S.A. Cambridge University (1988)

Renner W.D; O'Connor, T.P; Bermudez ,N.M. "An algorithm for design of beam compensators" *Int. J. Radiat. Oncol. Biol. Phys.* 17:227-234 (1989)

Ritchie, C.J; Godwin, J.D; Crawford, C.R; Stanford, W; Anno, H; Kim, Y. "Minimum Scan speeds for suppression of motion artifacts in CT" *Radiology* 185:37-42 (1992)

Ritchie, C.J; Hsieh, J; Gard, M.F; Godwin, J.D; Kim, Y; Crawford, C.R. "Predictive respiratory gating: a new method of reduce motion artifacts on CT scans" *Radiology* 190:847-852 (1994)

Robinson, P.J; Kreel, L. "Pulmonary tissue attenuation with computed tomography: Comparision of inspiration and expiration scans" *J. of Comp. Tomo.* 3:740-748   (1979)

Robinson, D.M; Scrimger, J.W. "Modelling of asymmetric compensator geometries" *Med. Phys.* 18:759-762 (1991)

Robinson, D.M; Scrimger, J.W. "Optimized tissue compensators" *Med. Phys.* 17:391-396 (1990)

Rogers, D.W.O;Faddegon, B.A; Ding, G.X; Ma C.-M; Wei, J; Mackie T.R. "BEAM: A Monte Carlo code to simulate radiotherapy treatment units" *Med. Phys.* 22:503- 524 (1995)

Rogers D.W.O. *Nucl. Instrum. Meth. Phys. Res.* 199:531-548 (1982)

Ross, C.S; Hussey, D.H; Pennington, E.C; Stanford, W; Doornbos, J.F. "Analysis   of movement of intrathoracic neoplasms using ultrafast computerized tomography" *Int. J. Radiat. Oncol. Biol. Phys.* 18:671-677 (1990)

Raditation Therapy Oncology Group, RTOG 93-11 "A phase I/II dose escalation study using three dimensional conformal radiation therapy in patients with inoperable, non-small cell lung cancer" (1995)

Schwartz, L.H; Richaud, J; Buffat, L; Touboul, E; Schlienger, M. "Kidney mobility during respiration" *Radiotherpy & Oncology* 32:84-86 (1994)

Sherouse, G.W. "Coordinate transfromation as a primary representation of radiotherapy beam geometry" *Med. Phys.* 20:175-179 (1993)

Sherouse, G.W. "A mathematical basis for selection of wedge angle and orientation" *Med. Phys.* 20:1211-1218 (1993)

Shragge, P.C; Patterson, M.S. "Improved method for the design of tissue compensators" *Med. Phys.* 8:885-891 (1981)

Sonntag, A. "[A path to spatial irradiation planning. I. The problem of dose homogeneity within the area of crossing ray beams with different planes of incidence; basic examinations leading to an optimization procedure] [German]" *Strahlentherapie* 150:507-520 (1975)

Sonntag, A. "[A way to spatial irradiation planning. II. Vectorial demonstration of spatial dose distribution within a single-ray beam and 1st consequences for the practice] [German]" *Strahlentherapie* 150:569-578 (1975)

Sontag, M.R; Cunningham, J.R; "The equivalent tissue air ratio method for making absorbed dose calculations in a heterogeneous medium" *Radiology* 129:787-794 (1978)

Steel, G.G; Adams, G.E; Horwich, A. (Editors) "The biological basis of radiotherapy" Elsevier, New York U.S.A (1989)

Sundblom, L. "Individually designed filters in cobalt 60 teletherapy" *Acta Radiologica [Ther] (Stockh)* 2:189 (1964)

National Cancer Institute of Canada. "Probability of developing cancer by age and lifetime probability of   developing (1990–92) and dying (1993) from cancer" Statistics Canada, http://www.statcan.ca/english/Pgdb/People/Health/health25a.htm#map (1996)

Tai, R.C; Lee, G.C. "Isotropy and homogeneity of lung tissue deformation" *J. Biomechanics* 14:243 (1981)

Taylor, J.R. "An introduction to error analysis" University Science Books, Sausalito U.S.A. (1982)

Ten Haken, R.K; Martel, M.K; Kessler, M.L; Hazuka, M.B; Lawrence, T.S; Robertson, J.M; Turrisi, A.T; Lichter, A.S. "Use of Veff and iso-NTCP in the implementation of dose escalation protocols" Int. J. Radiat. Oncol. Biol. Phys. 27:689-95 (1993)

Thames, H.D; Scheltheiss, T.E; Hendry, J.H; Tucker, S.L; Dubray, B.M; Brock, W.A. "Can modest escalations of dose be detected as increased tumor control?" Int. J. Radiat. Oncol. Biol. Phys. 22:241-246 (1992)

Tortora, G.J. "Principles of Human Anatomy", HarperCollins, New York U.S.A. (1992)

Urie, M.M; Goitein, M; Doppke, K; Kutcher, J.G; LoSasso, T; Mohan, R; Munzenrider, J.E; Sontag, M; Wong, J.W. "The role of uncertainty analysis in treatment planning" Int. J. Radiat. Oncol. Biol. Phys. 21:91-107 (1991)

Van de Geijn, J. "The construction of individualised intensity modifying filters in cobalt 60 teletherapy" Br. J. Radiol. 38:865-870 (1965)

Van Dyk, J; Keane, T.J; Rider, W.D. "Lung density as measured by computerized tomography: implications for radiotherapy" Int. J. Radiat. Oncol. Biol. Phys. 8:1363-1372 (1982)

Van Dyk, J; Barnett, R.B; Cygler, J.E; Shragge, P.C. "Commissioning and quality assurance of treatment planning computers" Int. J. Radiat. Oncol. Biol. Phys. 26:261-73 (1993)

Vawter, D.L; Matthews, F.L; West, J.B. "Effect of shape and size of lung and chest wall on stresses in the lung" Journal of Applied Physiology 39:9-17 (1975)

Vogel, J; Muller, E, Merker, G. [Computer analysis of mechanics of breathing by semi on-line technique (author's translation)]. German, Zeitschrift fur Erkangkungen der Atmongsorgange 145:331-338 (1976)

Wade, O.L. "Movements fo the thoracic cage and diaphragm in respiration" Journal of Physiology 124:193-212 (1954)

Weeks, K.J; Sontag, M.R. "3-D Dose-volume compensation using nonlinear least square regression technique" Med. Phys. 18:474-480 (1991)

Willet, C.G; Linggood, R.M; Stracher, M.A; Goitein, M; Doppke, K; Kushner, D.C; Morris, T; Purdy, J; Carroll, R. "The effect of the respiratory cycle on mediastinal and lung dimensions in Hodgkin's Disease (Implications for Radiotherapy Gated to Respiration)" Cancer 60:1232-1237 (1987)

Wilson, T.A; Rehder, K; Krayer, S; Hoffman, E.A; Whitney, C.G; Rodarte, J.R. "Geometry and respiratory displacement of human ribs" Journal of Applied Physiology 62:1872-1877 (1987)

Wong, J.W; Henkelman, R.M; "A new approach to CT-pixel-based photon dose calculations in heterogeneous media" Med. Phys. 10:199-208 (1983)

Wong, J.W; Purdy, J.A. "On methods of inhomogeneity corrections for photon transport" Med. Phys. 17:807-815 (1990)

Woo, M.K; Cunningham, J.R; Jezioranski, J.J. "Extending the concept of primary and scatter eparation to the condition of electronic disequilibrium" Med. Phys. 17:588-595 (1990)

Yakiwczuk, L. "Analysis of the Equivalent Tissue Air Ratio Method of Photon Dose Computation" M.Sc's Thesis, University of Alberta (1987)

Yorke, E; Harisaidis, L; Wessels, B; Aghdam, H; Altemus, R. "Dosimetric considerations in radiation therapy of coin lesions of the lung" *Int. J. Radiat. Oncol. Biol. Phys.* 34:481-487 (1996)

Young, M.E; Kornelson, R.O. "Dose corrections for low-density tissue inhomogeneities and air channels for 10 MV X-rays" *Med. Phys.* 10:450-455 (1983)

Zagars G.K; Schultheiss, T.E; Peters L.J. "Inter-tumor heterogeneity and radiation dose-control curves" *Radiotherapy & Oncology* 8:353-362 (1987)

Zwicker, R.D; Shahabi, S; Wu, A; Sternick, E.S. "Effective wedge angles for 6 MV wedges" *Med. Phys.* 12:347-349 (1985)